eXPRESS Polymer Letters Vol.4, No.6 (2010) 328
Available online at www.expresspolymlett.com
DOI: 10.3144/expresspolymlett.2010.41

Editorial corner – a personal view
Polymer-based functionally graded materials (FGMs): potential and challenges

*P. Krawczak**

Department of Polymers and Composites Technology & Mechanical Engineering, Ecole des Mines de Douai, 941 rue Charles Bourseul, BP 10838, 59508 Douai, France

Functionally Graded Materials (FGMs) are a class of engineered materials characterized by a spatial variation of composition and microstructure aiming at controlling corresponding functional (i.e. mechanical, thermal, electrical, etc.) properties. The tailored gradual variation of microstructural features may be obtained through non-uniform distributions of the reinforcement phase(s) with different properties, sizes and shapes, as well as by interchanging the role of reinforcement and matrix materials in a continuous manner. Various approaches are used to fabricate FGMs: bulk (particulate), preform, layer and melt processing techniques as well as ink-jet printing of different monomers followed by UV curing. These materials can be designed for specific functions and applications with a broad range of outlets in transportation, (bio)mechanical, civil or nuclear engineering, as well as sensor technology, tribology, optics, electronics or magnetics.

FGMs originally found widespread applications as metal-ceramic composites, in which there is a gradual microstructural transition from a ceramic rich to a metal rich region. Then, interest has emerged in the field of polymer-based FGMs, in particular for graded fibre composites, cellular structures (foams) or interpenetrating polymer networks.

Actually, organic structural composites and plastic foams present an interesting potential to design FGMs. On one hand, polymer composites are theoretically ideal materials that would permit to tailor reinforcement as a function of the applied stress field. By distributing a fixed amount of fibres having a well-mastered orientation according to fraction of load to carry, the graded composite may provide better performance. On the other hand, cellular plastics often naturally have a gradient of microstructure through the part cross-section, due to the processing technologies used (e.g. injection, extrusion or rotational moulding). The challenge is however to be able to vary gradually and continuously the material properties not only through the thickness but also along the part length or width (i.e. in 3D). The textile technology may contribute to address these issues successfully in the case of structural composites. In the case of cellular polymers, the processing technology control remains a key issue, which requires further intensive research efforts at a laboratory scale. The final challenge would be to develop manufacturing techniques to produce such functionally graded polymeric parts under industrially viable conditions (scale-up, mass production, repeatability, reliability, cost-effectiveness).

Prof. Dr. Patricia Krawczak
Member of International Advisory Board

*Corresponding author, e-mail: patricia.krawczak@mines-douai.fr

eXPRESS Polymer Letters Vol.4, No.6 (2010) 329–338
Available online at www.expresspolymlett.com
DOI: 10.3144/expresspolymlett.2010.42

Synthesis and characterization of PVP-functionalized superparamagnetic Fe_3O_4 nanoparticles as an MRI contrast agent

N. Arsalani[1*], *H. Fattahi*[1], *M. Nazarpoor*[2]

[1]Polymer Research Laboratory, Department of Organic and Biochemistry, Faculty of Chemistry, University of Tabriz, Tabriz, Iran
[2]Department of Radiology, Faculty of Paramedical, Tabriz University of Medical Sciences, Tabriz, Iran

Received 21 January 2010; accepted in revised form 19 March 2010

Abstract. The magnetite (Fe_3O_4) nanoparticles (MNPs) coated with poly(N-vinyl pyrrolidone) (PVP) via covalent bonds were prepared as T_2 contrast agent for magnetic resonance imaging (MRI). The surface of MNPs was first coated with 3-(trimethoxysilyl) propyl methacrylate (silan A) by a silanization reaction to introduce reactive vinyl groups onto the surface, then poly(N-vinyl pyrrolidone) was grafted onto the surface of modified-MNPs via surface-initiated radical polymerization. The obtained nanoparticles were characterized by FT-IR (Fourier transform infrared spectroscopy), XRD (X-ray diffraction), TEM (transmission electron microscopy), VSM (vibrating sample magnetometer), and TGA (thermogravimetric analysis). The MNPs had an average size of 14 nm and exhibited superparamagnetism and high saturation magnetization at room temperature. T_2-weighted MRI images of PVP-grafted MNPs showed that the magnetic resonance signal is enhanced significantly with increasing nanoparticle concentration in water. The r_1 and r_2 values per millimole Fe, and r_2/r_1 value of the PVP-grafted MNPs were calculated to be 2.6 , 72.1, and 28.1$(mmol/l)^{-1}\cdot s^{-1}$, respectively. These results indicate that the PVP-grafted MNPs have great potential for application in MRI as a T_2 contrast agent.

Keywords: *nanomaterials, superparamagnetism, iron oxide nanoparticles, MRI contrast agent*

1. Introduction

In recent years, superparamagnetic iron oxide nanoparticles have shown great potential applications in many biological fields, including targeted-drug delivery [1, 2], bioseparation [3], tissue repair [4], cancer treatment through hyperthermia [5, 6], and magnetic resonance imaging (MRI) contrast enhancement [7–9].

MRI is an appealing noninvasive approach for early cancer diagnostics and therapeutics [10]. However, in clinical diagnosis, it is often the case that the diseased and healthy tissues are similar in composition and MRI technology alone will not always differentiate the two. A contrast agent is necessary to distinguish the normal and diseased tissue. The conventional, gadolinium compounds [11] have been used as T_1 contrast agents that cause positive contrast enhancement and provide a bright state in the image where the compounds are accumulated [12]. However, with the increasing use of paramagnetic gadolinium chelates for MRI, shortcomings of gadolinium chelates have been found, such as fast elimination in tissue; non-specific distribution in vivo and limited effect in improving MR imaging.

Since superparamagnetic Fe_3O_4 nanoparticles can enhance the alterations of proton relaxation in the tissue microenvironment, these are suitable as T_2 contrast agent in MRI [13, 14]. These T_2 contrast agents cause to decrease the signal intensity in the

*Corresponding author, e-mail: arsalani@tabrizu.ac.ir

region that they are accumulated, and hence cause negative contrast and provide a dark state in the image where the compounds are accumulated [15]. However, the direct use of magnetic nanoparticles as in vivo MRI contrast agent results in biofouling of the particles in blood plasma and formation of aggregates that are quickly sequestered by cells of the reticular endothelial system (RES) such as macrophages [16, 17]. Furthermore, aggregated nanoparticles change their superparamagnetic response [7]. Therefore, in order to minimize biofouling and aggregation of particles and escape from the RES for longer circulation times, the nanoparticles are usually coated with a layer of hydrophilic and biocompatible polymer such as dextran [18], dendrimers [19], poly(ethylene glycol) (PEG) [20], and poly(vinyl pyrrolidone) (PVP) [21–23]. Of synthetic polymers, PVP is water-soluble, non-charged, non-toxic, and is used in various medical applications [24]. While there is a potential concern about covalent interaction between hydrophilic polymers and magnetic nanoparticles in order to increase their stability in physiological medium [25–29], PVP coating on Fe_3O_4 nanoparticles in all previous works has been achieved through noncovalent interaction.

Now, polymers grafting of magnetic nanoparticles is one of the most attractive methods of surface modification [30, 31]. In the present study, we carried out chemical synthesis and characterization of PVP-functionalized magnetite (Fe_3O_4) nanoparticles. Since the PVP was bonded to the surface of magnetite nanoparticles through covalent bonds, the prepared magnetic fluid (ferrofluid) was very stable for a long period of time. To this aim, first magnetite nanoparticles were synthesized by the chemical co-precipitation of Fe^{3+} and Fe^{2+} ions with NH_4OH. Then, the nanoparticles were modified directly by 3-(trimethoxysilyl) propyl methacrylate (silan A) to introduce reactive vinyl groups on the particles surface, and poly(N-vinyl pyrrolidone) was grafted onto modified nanoparticles by surface-initiated radical polymerization. The structure, particle size, and composition of PVP-functionalized magnetite nanoparticles were examined by FT-IR (Fourier transform infrared spectroscopy), XRD (X-ray diffraction), TEM (transmission electron microscopy), VSM (vibrating sample magnetometer), and TGA (thermogravimetric analysis). Furthermore, the PVP-functionalized MNPs were dispersed in water to form stable magnetic fluids. T_2-weighted MRI images of PVP-grafted magnetic nanoparticles were obtained and the results indicated that they have great potential for application in MRI as T_2 contrast agent.

2. Experimental

2.1. Materials

Ferric chloride haxahydrate ($FeCl_3 \cdot 6H_2O$, >99%), ferrous chloride tetrahydrate ($FeCl_2 \cdot 4H_2O$, >99%) and ammonium hydroxide (25 wt%) were obtained from Fluka (Switzerland). 3-(trimethoxysilyl) propyl methacrylate (silan A), dichloromethane and Azobisisobutyronitrile (AIBN) were purchased from Merck (Schuchardt, Germany). All the materials mentioned above were used without further purification. N-vinyl pyrrolidone was obtained from Merck (Schuchardt, Germany) and was distilled under reduced pressure prior to use. Ethanol (96%) was provided by Simin Tak (Qazvin, Iran). Distilled water was used throughout the work.

2.2. Synthesis of Fe_3O_4 nanoparticles

The preparation of Fe_3O_4 nanoparticles was followed by a chemical co-precipitation of Fe^{2+} and Fe^{3+} ions described previously [32]. Briefly, fifty milliliters of 1.0 mol/l Fe^{2+} and 2.0 mol/l Fe^{3+} solutions were prepared with deionized water in two beakers, and then transferred to a 250 ml three-necked flask together. When the solution was heated to 80°C, NH_4OH (25 wt%) was added dropwise under argon protection and vigorous mechanical stirring until pH = 10–11. As the base was added, the solution immediately turned black indicating the formation of iron oxide in the system. The solution was heated at 80°C for 1 h, and then the precipitated powders were collected by magnetic separation. The obtained magnetic nanoparticles were washed immediately with deionized water for five times and then with dichloromethane for three times. The final product was dried into powder at 40°C under vacuum.

2.3. Preparation of silan A-modified Fe_3O_4 nanoparticles

In order to introduce vinyl group onto the magnetic nanoparticles, we used 3-(trimethoxysilyl) propyl

methacrylate (silan A) as a coupling agent. Silan A-modified magnetic nanoparticles were achieved by the silanization reaction between Silan A and the hydroxyl groups on the surface of magnetite. Namely, 3.7 g of Fe_3O_4 nanoparticles were dispersed in 40 ml toluene by sonication for about 1 h, and then 19.5 mmol (4.66 ml) of Silan A was added under argon atmosphere using a syringe. The reaction mixture was kept at room temperature for 5 h with vigorous mechanical stirring. Afterwards, the Silan A-immobilized Fe_3O_4 nanoparticles were obtained by magnetic separation and washed with ethanol (2×30 ml) and dichloromethane (2×30 ml) in turn. They were then dried in a vacuum oven at 40°C overnight.

2.4. Synthesis of PVP-grafted Fe_3O_4 nanoparticles

The graft polymerization was performed using surface-initiated radical polymerization, according to a modified procedure [31]. In a typical protocol, 0.5 g of silan A-modified Fe_3O_4 nanoparticles, 0.069 g of AIBN, 44 ml of ethanol and 10 ml of deionized water were put in a flask and vibrated with ultrasonic for 30 min under argon to be dispersed uniformly. Then the flask was heated at 70°C, mechanically stirred at 400 rpm under argon, and a mixture of N-vinyl pyrrolidone (6.4 ml, 0.06 mol), ethanol (7 ml), and deionized water (7 ml) was added dropwise into the flask within 1 h. The graft polymerization was performed at 70°C for 6 h. Then the resultant product was collected by magnetic separation, washed with ethanol for several times, and finally dried at 40°C in a vacuum oven.

2.5. Characterization techniques

Nano-Fe_3O_4, nano-Fe_3O_4 modified with silan A and also PVP-grafted Fe_3O_4 nanoparticles were tested by Fourier transform infrared (FT-IR) spectroscopy. The measurements were performed on a TENSOR 27 spectrometer (Bruker, Germany) with a solid potassium bromide method, with 2 cm^{-1} resolution and 10 scanning times.

The nanoparticles were observed with transmission electron microscope (TEM) (Jeol TEM-2100, Japan) operated at 200 kV. Investigating TEM, the nanoparticles were deposited on a copper-grid-supported perforated transparent carbon coil. The crystal structure of prepared nanoparticles was studied by an X-ray diffractometer (Siemens D5000, Germany) using CuK_α radiation (λ = 1.5418 Å). Particle size distribution was determined by particle size analyzer (Photal ELS Z, Otsuka Electronics, Japan).

Thermogravimetric analysis (TGA) experiments were performed by TGA 951 (DuPont, USA). Dried samples (1–5 mg) were placed in the TGA furnace and the measurements were carried out under nitrogen with a heating rate of 15°C/min from 30 to 650°C. The magnetic properties of Fe_3O_4 nanoparticles were measured at room temperature with vibrating sample magnetometer (VSM) (LakeShore 7307, USA).

MRI experiments were performed at 25°C in a clinical magnetic resonance (MR) scanner (GE Signa EXCITE 1.5T, USA). To demonstrate the T_1 and T_2 effects in an aqueous solution, PVP-grafted magnetic nanoparticles were suspended in tubes of water (10 ml) with iron concentration at 0, 0.025, 0.050, 0.075, 0.100, 0.200, 0.400, and 0.600 mmol/l Fe, respectively. The tubes were placed into the MR scanner and a number of spin-echo sequences were run for determining both T_2 and T_1 relaxation times. The IDL software (version 5.5) was used for data acquisition. To estimate the T_2 relaxation time for each sample, coronal images (TH = 10 mm) were acquired at various echo times (TE) from 10 to 140 ms with a repetition time (TR) of 1600 ms. Similarly, the T_1 relaxation time for each sample was measured by varying TR between 100 and 6400 ms while keeping TE constant at 18 ms. After acquiring the images, the magnitudes of image intensities were measured within manually-drawn regions of interest (ROIs) for each sample. Relaxation rates R_1 ($1/T_1$) and R_2 ($1/T_2$) were calculated by mono-exponential curve fitting of the signal intensity vs. time (TE or TR). The Equations (1) and (2) were used for curve fitting of relaxation rate R_1 and R_2, respectively [33]:

For relaxation rate R_1:

$$I = A \cdot [1 - \exp(-R_1 \cdot TR)] \tag{1}$$

For relaxation rate R_2:

$$I = A + C \cdot [\exp(-R_2 \cdot TE)] \tag{2}$$

where I is the signal intensity. Plotting R_1 (or R_2) vs. iron concentration gives T_1 relaxivity (r_1) or T_2 relaxivity (r_2) as the slope, respectively.

3. Results and discussion

3.1. Preparation of PVP-grafted Fe_3O_4 nanoparticles

The process for synthesis of PVP-grafted Fe_3O_4 nanoparticles is shown in Figure 1. The Fe_3O_4 nanoparticles were synthesized by a chemical co-precipitation of Fe^{2+} and Fe^{3+} ions under alkaline condition. The concentration ratio of Fe^{2+}/Fe^{3+} was 1:2, and the experiment was carried out under argon gas to prevent Fe^{2+} oxidation to Fe^{3+}. The Fe_3O_4 nanoparticles prepared by the co-precipitation method have a number of hydroxyl groups on the surface. Silan A-modified MNPs were achieved by the silanization reaction between silan A and the hydroxyl groups on the surface of magnetite (Figure 1).

Surface-grafted polymerization of N-vinyl pyrrolidone involves two reactions, which take place simultaneously. On the surface of silan A-modified Fe_3O_4 nanoparticles, the graft polymerization occurs, while the random polymerization takes place in the solution. In order to decrease the random polymerization, the following strategies were adopted. On the one hand, AIBN was dissolved in the modified nanoparticles suspended solution and the solution was placed overnight to let nanoparticles absorb AIBN on the surface the most. On the other side, the monomer was added dropwise in the reaction mixture. Following the application of the procedure explained, as the mixture is heated the vinyl groups on the surface of nanoparticles are activated by initiator and when the monomer is added slowly to the mixture, surface-initiated radical polymerization occurs. The ungrafted oligomers would be separated by magnetic decantation after reaction.

3.2. FT-IR analysis

To evaluate the graft polymerization, the homopolymers and unreacted monomers were extracted from final product within ethanol to be separated from the grafted nanoparticles. Figure 2 shows the FT-IR spectra of pure Fe_3O_4, silan A-treated Fe_3O_4 and PVP-grafted Fe_3O_4 nanoparticles, respectively. From the IR spectra presented in this figure, the absorption peak at 580 cm^{-1} belongs to the stretching vibration mode of Fe–O bonds in Fe_3O_4. Comparing with the IR spectrum of pure Fe_3O_4 (Figure 2a), the IR spectrum of Silan A-modified Fe_3O_4 (Figure 2b) has absorption peaks presented at 1700 and 1648 cm^{-1} being relevant to the stretching vibration of conjugated esteric C=O and stretching vibration of C=C bonds, respectively. Absorption bonds of stretching vibrations of esteric C–O bond are appeared at 1172 and 1017 cm^{-1}. Absorbent peaks at 2926 and 1460 cm^{-1} belong to asymmetric stretching vibration and scissoring bending vibration of CH_2 group, respectively. All these peaks revealed the existence of silan A and indicated that the reactive groups had been introduced onto the surface of magnetite. In Figure 2c, the absorbent peak at 1660 cm^{-1} belongs to C=O group of N-vinyl pyrrolidone. Asymmetric stretching and scissoring bending vibrations of CH_2 group of N-vinyl pyrrolidone are appeared at 1957 and 1465 cm^{-1}, respectively. The absorbent peak centered at 1289 cm^{-1} is due to C–N stretching vibration of N-vinyl pyrrolidone. Also the peak at 2957 cm^{-1} is

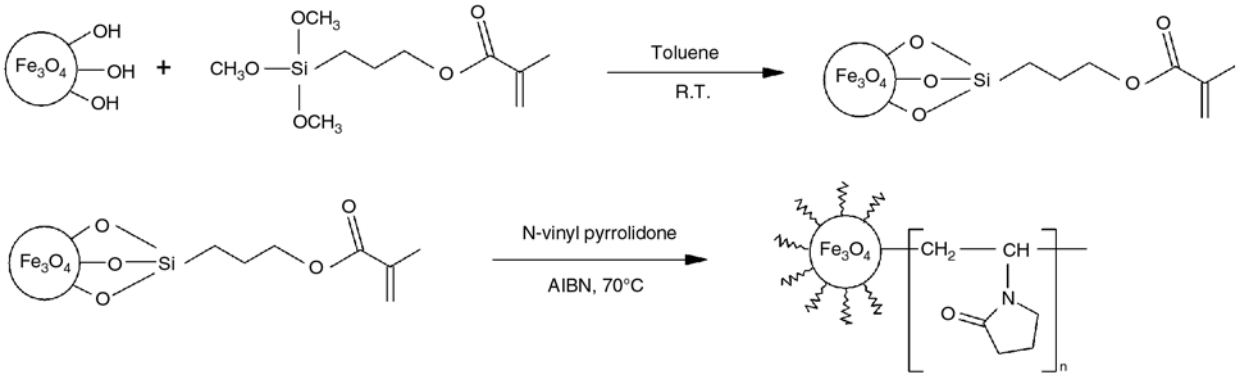

Figure 1. Surface modification and graft polymerization of magnetic nanoparticles

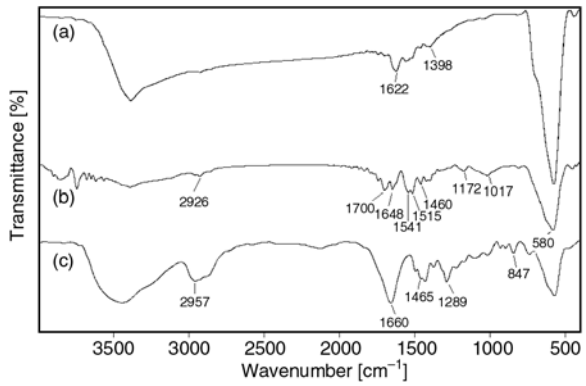

Figure 2. FT-IR spectra of (a) pure Fe_3O_4 nanoparticles; (b) Fe_3O_4 nanoparticles modified with Silan A; (c) PVP-grafted Fe_3O_4 nanoparticles

due to the asymmetric stretching vibration of CH_3 group of azobisisobutyronitrile (AIBN) that is used as initiator. Overall, these FT-IR spectra indicated that N-vinyl pyrrolidone polymer chains were successfully grafted onto the Fe_3O_4 nanoparticles surface.

3.3. X-ray diffraction (XRD)

The XRD diffraction patterns of pure magnetite, silan A treated magnetite and PVP-grafted magnetite nanoparticles are shown in Figure 3a–3c, respectively. It is apparent that the diffraction pattern of our Fe_3O_4 nanoparticles is close to the standard pattern of crystalline magnetite (Figure 3a). The characteristic diffraction peaks marked, respectively, by their indices (220), (311), (400), (422), and (511) could be well indexed to the inverse cubic spinel structure of Fe_3O_4. The average crystallite size D was calculated using the Debye-Scherrer formula $D = K\lambda/\beta\cos\theta$, where K is

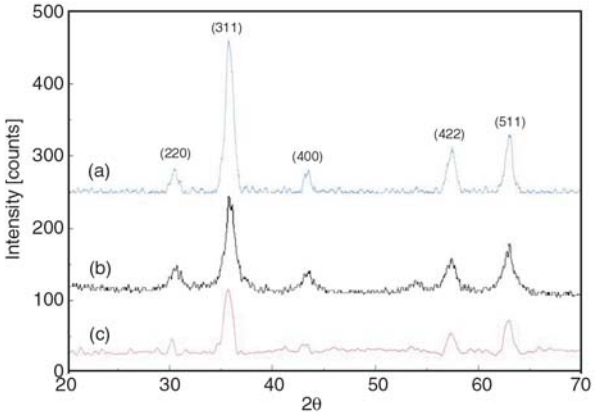

Figure 3. XRD patterns of (a) pure Fe_3O_4 nanoparticles; (b) silan A-modified Fe_3O_4 nanoparticles; (c) PVP-grafted Fe_3O_4 nanoparticles

Table 1. The intensity of magnetite diffraction peaks before and after coating

Difraction peak	Intensity (counts)		
	Fe_3O_4	Silan A-modified Fe_3O_4	PVP-grafted Fe_3O_4
220	33.32	28.32	25.18
311	212.43	131.39	87.73
400	31.47	26.75	11.02
422	63.73	46.42	26.35
511	81.04	68.06	44.45

Scherrer constant, λ is the X-ray wavelength, β is the peak width of half-maximum, and θ is the Bragg diffraction angle. The crystallite size obtained from this equation was found to be about 19 nm, which is basically in accordance with the transmission electron microscopy. These characteristic peaks can also be found in Figure 3b and 3c, which illustrated that the characteristic peaks did not change but only the peak intensity and width after coated with silan A and PVP, showing that the crystalline structure of the modified nanoparticles was not varied. The intensity of peaks for each sample is given in Table 1.

3.4. Transmission electron microscopy (TEM)

The TEM micrographs of pure Fe_3O_4 nanoparticles (Figure 4a) and Fe_3O_4 nanoparticles grafted by poly(N-vinyl pyrrolidone) (Figure 4b) are shown. Particles with an average diameter of 14 nm were observed. This result is in good accordance with the estimation from X-ray diffraction results. The electron diffraction pattern (Figure 4c) consisting of rings indicates the good crystal structure of the nanoparticles. It can be seen that the particles have a strong tendency to aggregate as a result of the interaction of the polymer grafted on the nanoparticles. This is a further confirmation of the encapsulation of Fe_3O_4 magnetic core polymerized with PVP.

The surface-grafted magnetic nanoparticles could be easily dispersed in water to form a uniform suspension and be stably preserved for several months, suggesting that the tendency for the aggregation of particles is considerably weakened, whereas the suspension made from the bare magnetic nanoparticles is completely precipitated from the solvent in only a few minutes without stirring. Figure 5 shows the size distribution plot for PVP-grafted nanoparticles, as it can be seen the size of nanoparticles has

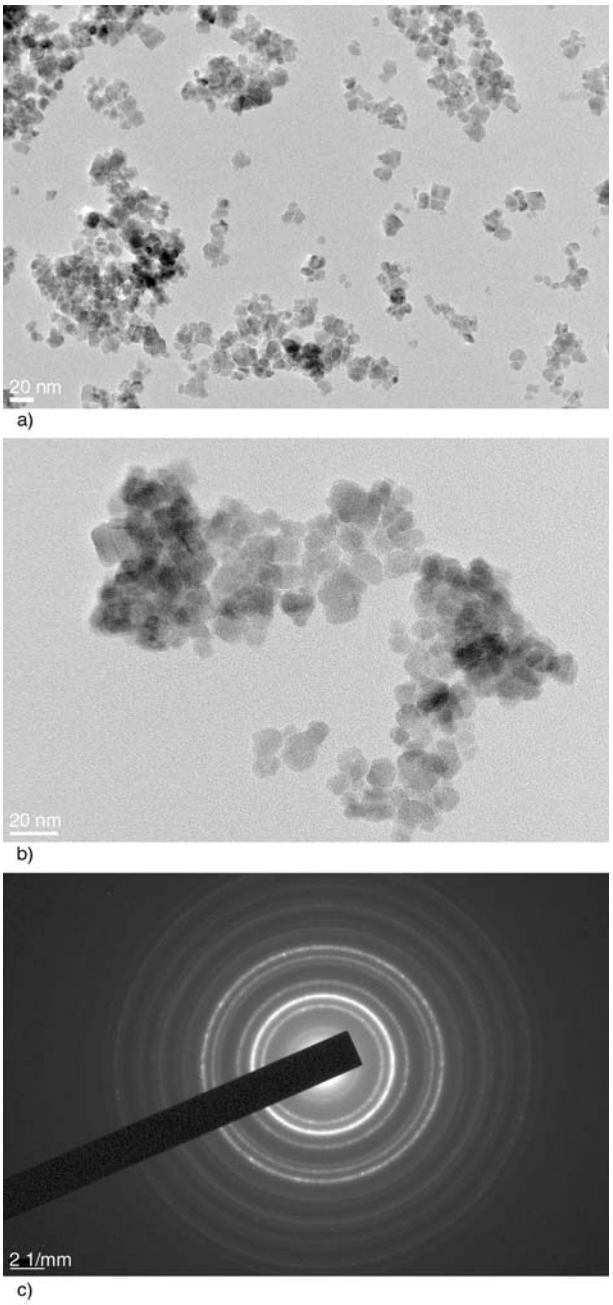

Figure 4. TEM images of (a) pure Fe_3O_4 nanoparticles; (b) PVP-grafted Fe_3O_4 nanoparticles; (c) Electron diffraction pattern of pure Fe_3O_4 nanoparticles

increased because of organic coating and also their aggregation, this is in good agreement with TEM image.

3.5. Thermogravimetric analysis

The magnetite contents of Silan A treated magnetite and PVP-grafted magnetite were measured through the TGA under nitrogen atmosphere condition at the heating rate of 15°C/min. Figure 6 illustrates the TGA curves, depicting the variations of residual masses of the samples with temperature. The organic materials and magnetite of the samples were completely burned to generate gas products and converted into Fe_2O_3 at elevated temperatures, respectively. The magnetite amounts of samples can be estimated from the residual mass percentages. The absolute weight loss of the uncoated Fe_3O_4 is 3.2% (Figure 6a) for the whole temperature range because of the removal of adsorbed physical and chemical water. Figure 6b shows that the weight loss increased above 200°C, attributed to the loss of silan A layer coated on the MNPs. It is estimated that the weight loss of silan A coated on the Fe_3O_4 nanoparticles is about 3.8%. As shown in Figure 6c, for PVP-grafted MNPs the first weight loss stage (below 140°C) can be ascribed to the evaporation of water molecules in the polymer matrix, while the other stage beginning at about 200°C was due to the decomposition of PVP. Thermogravimetric chart of PVP-grafted Fe_3O_4 nanopar-

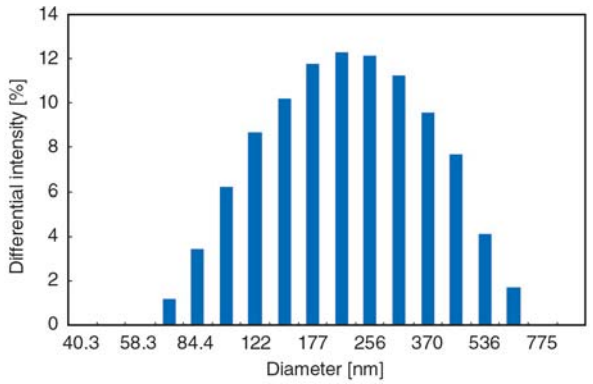

Figure 5. Size distribution plot of PVP-grafted Fe_3O_4 nanoparticles

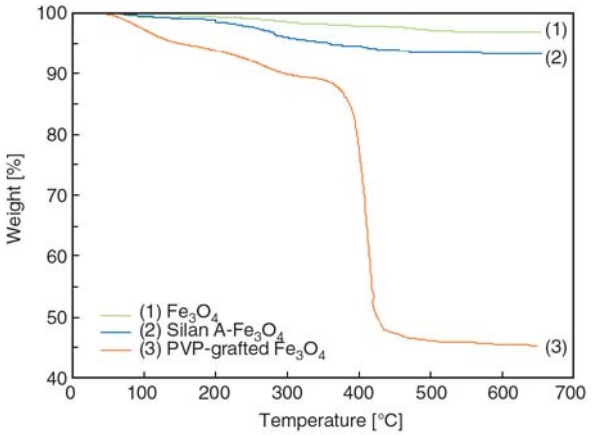

Figure 6. TGA curves of (a) pure Fe_3O_4 nanoparticles; (b) silan A-treated Fe_3O_4 nanoparticles; (c) PVP-grafted Fe_3O_4 nanoparticles

ticles pointed that magnetite content is about 45.3%.

3.6. Analysis of magnetic properties

Figure 7 shows the magnetization curves of pure, silan A-modified, and PVP-grafted Fe_3O_4 nanoparticles respectively, determined by VSM at room temperature. The saturation magnetization (M_s) is found to be 51.6 and 33.5 emu/g for silan A-modified Fe_3O_4 and PVP-grafted Fe_3O_4, respectively, less than the pure Fe_3O_4 nanoparticles (62.1 emu/g). This difference suggests that Silan A and PVP are grafted on the surface of Fe_3O_4 nanoparticles. As M_s of 7–22 emu/g is reported adoptable for bioapplications [34, 35], the level of M_s achieved for PVP-grafted Fe_3O_4 nanoparticles (33.5 emu/g) is deemed sufficient for such applications. In addition, there is no hysterisis in the magnetization curve with both remanence and coercivity being zero, indicating that these magnetic nanoparticles are superparamagnetic.

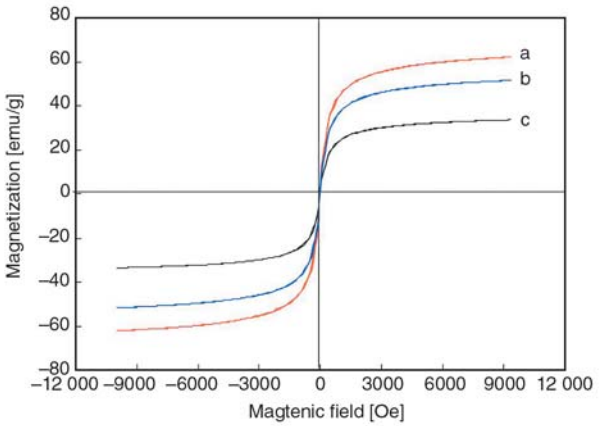

Figure 7. Magnetization curves of (a) pure Fe_3O_4 nanoparticles; (b) Fe_3O_4 nanoparticles treated by Silan A; (c) PVP-grafted Fe_3O_4 nanoparticles

3.7. MRI and relaxivities

Since superparamagnetic Fe_3O_4 nanoparticles are good T_2-type (negative) contrast agents in MRI, and PVP is a biocompatible macromolecule, the effect of PVP-grafted MNPs was investigated in terms of MR signal-enhancing property. To investigate such a property a phantom test was carried out. Figure 8 shows T_2-weighted MR images of various concentrations of PVP-grafted Fe_3O_4 nanoparticles in water (spin-echo technique with TR = 1600 and TE = 140 ms). It can be seen that the MR signal

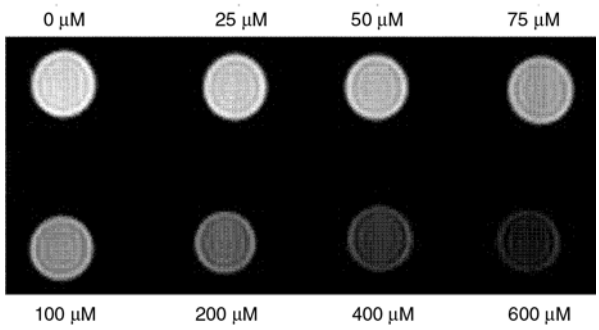

Figure 8. T_2-weighted MRI images (1.5T, spin-echo sequence: repitition time TR = 1600 ms, echo time TE = 140 ms) of the PVP-grafted Fe_3O_4 nanoparticles at various iron concentration at 25°C

intensity (related to the T_2 relaxation time in T_2-weighted images) for the samples of different concentrations is not identical. With increasing nanoparticles concentration in water, the MR signal is enhanced significantly (negative in brightness in T_2-weighted image). The T_2 relaxation process occurs because of the exchange of energy between protons in water molecules. In the presence of an externally applied magnetic field, superparamagnetic iron oxide nanoparticles create inhomogeneity in the magnetic field affecting the microenvironment that results in dephasing of the magnetic moments of protons and hence T_2 shortening. The results indicate that the nanoparticles can generate high magnetic field gradients near the surface of the PVP-grafted Fe_3O_4 nanoparticles.

Figure 9a and 9b show the relaxation rates R_1 ($R_1 = 1/T_1$) and R_2 ($R_2 = 1/T_2$) as a function of the iron molar concentration, [Fe], for the PVP-grafted MNPs. In Figure 9a and 9b, the relaxation rates R_1 and R_2 were found to vary linearly with the iron concentration, according to the Equations (3) and (4), respectively [36]:

$$\frac{1}{T_1} = \frac{1}{T_1([\mathrm{Fe}]=0)} + r_1[\mathrm{Fe}] \tag{3}$$

$$\frac{1}{T_2} = \frac{1}{T_2([\mathrm{Fe}]=0)} + r_2[\mathrm{Fe}] \tag{4}$$

where r_1 and r_2 are the longitudinal and transversal relaxivities, respectively. The intercepts $1/T_1$ ([Fe] = 0) and $1/T_2$ ([Fe] = 0) are the proton inverse relaxation times in pure water. The r_1 value per millimole Fe of the PVP-grafted MNPs is 2.6 $(\mathrm{mmol/l})^{-1}\cdot\mathrm{s}^{-1}$, while the r_2 value is 72.1 $(\mathrm{mmol/l})^{-1}\cdot\mathrm{s}^{-1}$. It is well known that the relax-

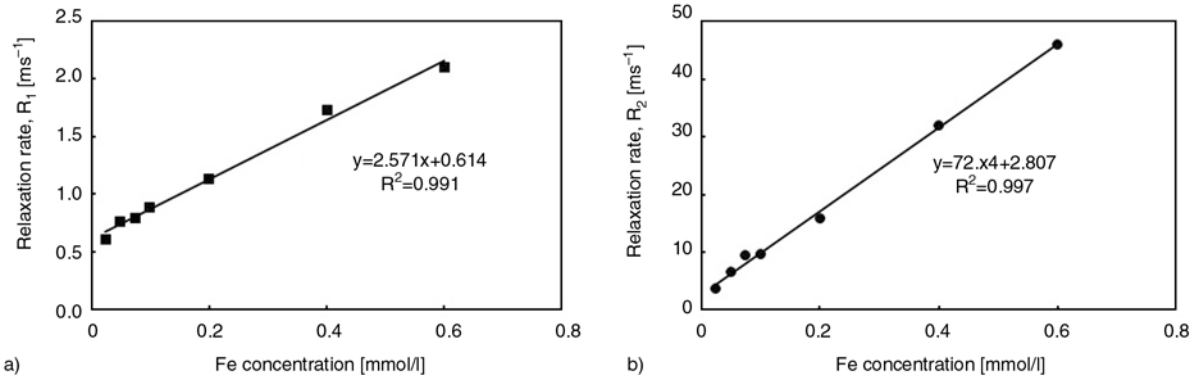

Figure 9. (a) T_1 and (b) T_2 relaxation rates ($1/T_1$ and $1/T_2$ [s^{-1}]) as a function of iron concentration [mmol/l] of PVP-grafted Fe_3O_4 nanoparticles in aqueous solution (1.5*T*, 25°C)

ivity ratio, r_2/r_1, is usually an important parameter to estimate the efficiency of T_2-contrast agents. In our work, the r_2/r_1 is calculated to be 28.1, which is much larger than that of dextran-coated MNPs [37], demonstrating the PVP-grafted MNPs should perform well as T_2-contrast agents in magnetic resonance imaging.

4. Conclusions

In summery, the present work reports on the preparation of superparamagnetic Fe_3O_4 nanoparticles through co-precipitation method followed by surface modification with poly(N-vinyl pyrrolidone) in two steps. First, magnetite nanoparticles were modified by 3-(trimethoxysilyl) propyl methacrylate (silan A) to introduce reactive groups onto the nanoparticles surface. Second, N-vinyl pyrrolidone was grafted onto the surface of modified-Fe_3O_4 nanoparticles by surface-initiated radical polymerization. The results indicate that the polymer chains had been effectively grafted onto the surface of Fe_3O_4 nanoparticles. The functionalized nanoparticles are superparamagnetic with M_s of 33.5 emu/g and possess good dispersibility and stability in water for a long period of time. MRI of the nanoparticles in water confirmed its contrast enhancement effect in T_2-weighted sequences. Calculated r_1 and r_2 relaxivites, and also r_2/r_1 ratio indicate that the PVP-grafted nanoparticles may be a good candidate as T_2 contrast agent.

Acknowledgements

The cooperation of Hafez medical imaging center of Tabriz (Dr. Zynat Mayabi, and Mr. Ali Kolahduz) in acquiring the MRI images is acknowledged. Also, authors gratefully acknowledge the assistance of Mr. Saso Gyergyek and Mr. Slavko Kralj, Joseph Stephan Institute of Slovenia, in the recoding of TEM images and VSM measurements.

References

[1] Son S. J., Reichel J., He B., Schuchman M., Lee S. B.: Magnetic nanotubes for magnetic-field-assisted bioseparation, biointeraction, and drug delivery. Journal of American Chemical Society, **127**, 7316–7317 (2005).
DOI: 10.1021/ja0517365

[2] Tietze R., Jurgons R., Lyer S., Schreiber E., Wiekhorst F., Eberbeck D., Richter H., Steinhoff U., Trahms L., Alexiou C.: Quantification of drug-loaded magnetic nanoparticles in rabbit liver and tumor after *in vivo* administration. Journal of Magnetism and Magnetic Materials, **321**, 1465–1468 (2009).
DOI: 10.1016/j.jmmm.2009.02.068

[3] Liu K. J. W., Zhang Y., Chen D., Yang T., Chen Z. P., Pan S. Y., Gu N.: Facile synthesis of high-magnetization γ-Fe_2O_3/alginate/silica microspheres for isolation of plasma DNA. Colloids and Surface A: Physicochemical and Engineering Aspects, **341**, 33–39 (2009).
DOI: 10.1016/j.colsurfa.2009.03.033

[4] Gupta A. K., Gupta M.: Synthesis and surface engineering of iron oxide nanoparticles for biomedical applications. Biomaterials, **26**, 3995–4021 (2005).
DOI: 10.1016/j.biomaterials.2004.10.012

[5] Zhang L-Y., Gu H-C., Wang X-M.: Magnetite ferrofluid with high specific absorption rate for application in hyperthermia. Journal of Magnetism and Magnetic Materials, **311**, 228–233 (2007).
DOI: 10.1016/j.jmmm.2006.11.179

[6] Allard E., Passirani C., Benoit J. P.: Convection-enhanced delivery of nanocarriers for the treatment of brain tumors. Biomaterials, **30**, 2302–2318 (2009).
DOI: 10.1016/j.biomaterials.2009.01.003

[7] Mody V. V., Nounou M. I., Bikram M.: Novel nanomedicine-based MRI contrast agents for gynecological malignancies. Advanced Drug Delivery Reviews, **61**, 795–807 (2009).
DOI: 10.1016/j.addr.2009.04.020

[8] Liu H., Li J.: Preparation and characterization of poly(PEGMA) modified superparamagnetic nanogels used as potential MRI contrast agents. Iranian Polymer Journal, **17**, 721–727 (2008).

[9] Corti M., Lascialfari A., Micotti E., Castellano A., Donativi M., Quarta A., Cozzoli P. D., Manna L., Pellegrino T., Sangregorio C.: Magnetic properties of novel superparamagnetic MRI contrast agents based on colloidal nanocrystals. Journal of Magnetism and Magnetic Materials, **320**, 320–323 (2008).
DOI: 10.1016/j.jmmm.2008.02.064

[10] Bulte J. W., Hoekstra Y., Kamman R. L., Magin R. L., Webb A. G., Briggs R. W., Go K. G., Hulstaert C. E., Miltenyi S.: Specific MR imaging of human lymphocytes by monoclonal antibody-guided dextran-magnetite particles. Magnetic Resonance in Medicine, **25**, 148–157 (1992).
DOI: 10.1002/mrm.1910250115

[11] Feng J., Sun G., Pei F., Liu M.: Comparison between GdDTPA and two gadolinium polyoxometalates as potential MRI contrast agents. Journal of Inorganic Biochemistry, **92**, 193–199 (2002).
DOI: 10.1016/S0162-0134(02)00557-3

[12] Semelka R. C., Helmberger T. K. G.: Contrast agents for MR imaging of the liver. Radiology, **218**, 27–38 (2001).

[13] Bean C. P., Livingston J. D.: Superparamagnetism. Journal of Applied Physics, **30**, 120–129 (1959).
DOI: 10.1063/1.2185850

[14] Koenig S. H., Brown R. D.: Relaxometry of magnetic resonance imaging contrast agents. Magnetic Resonance Annual, **5**, 263–286 (1987).

[15] Senéterre E., Taourel P., Bouvier Y., Pradel J., Van Beers B., Daures J. P., Pringot J., Mathieu D., Bruel J. M.: Detection of hepatic metastases: Ferumoxides-enhanced MR imaging versus unenhanced MR imaging and CT during arterial portography. Radiology, **200**, 785–792 (1996).

[16] Kaim A. H., Wischer T., O'Reilly T., Jundt G., Fröhlich J., Schulthess G. K., Allegrini P. R.: MR imaging with ultrasmall superparamagnetic iron oxide particles in experimental soft-tissue infections in rats. Radiology, **225**, 808–814 (2002).
DOI: 10.1148/radiol.2253011485

[17] Jung C. W., Jacobs P.: Physical and chemical properties of superparamagnetic iron oxide MR contrast agents: Ferumoxides, ferumoxtran, ferumoxsil. Magnetic Resonance Imaging, **13**, 661–674 (1995).
DOI: 10.1016/0730-725X(95)00024-B

[18] Lacava L. M., Lacava Z. G., Da Silva M. F., Silva O., Chaves S. B., Azevedo R. B., Pelegrini F., Gansau C., Buske N., Sabolovic D., Morais P. C.: Magnetic resonance of a dextran-coated magnetic fluid intravenously administered in mice. Biophysical Journal, **80**, 2483–2486 (2001).
DOI: 10.1016/S0006-3495(01)76217-0

[19] Strable E., Bulte J. M., Moskowitz B., Vivekanandan K., Allen M., Douglas T.: Synthesis and characterization of soluble iron oxide-dendrimer composites. Chemistry of Materials, **13**, 2201–2209 (2001).
DOI: 10.1021/cm010125i

[20] Kohler N., Sun C., Fichtenholtz A., Gunn J., Fang C., Zhang M. Q.: Methotrexate-immobilized poly(ethylene glycol) magnetic nanoparticles for MR imaging and drug delivery. Small, **2**, 785–792 (2006).
DOI: 10.1002/smll.200600009

[21] Lee H-Y., Lee S-H., Xu C., Xie J., Lee J-H., Wu B., Koh A. L., Wang X., Sinclair R., Wang S. X., Nishimura D. G., Biswal S., Sun S., Cho S. H., Chen X.: Synthesis and characterization of PVP-coated large core iron oxide nanoparticles as an MRI contrast agent. Nanotechnology, **19**, 165101/1–165101/6 (2008).
DOI: 10.1088/0957-4484/19/16/165101

[22] Liu H-L., Ko S. P., Wu J-H., Jung M-H., Min J. H., Lee J. H., An B. H., Kim Y. K.: One-pot polyol synthesis of monosize PVP-coated sub-5 nm Fe_3O_4 nanoparticles for biomedical applications. Journal of Magnetism and Magnetic Materials, **310**, 815–817 (2007).
DOI: 10.1016/j.jmmm.2006.10.776

[23] Lee H. Y., Lim N. H., Seo J. A., Yuk S. H., Kwak B. K., Khang G., Lee H. B., Cho S. H.: Preparation and magnetic resonance imaging effect of polyvinylpyrrolidone-coated iron oxide nanoparticles. Journal of Biomedical Materials Research B: Applied Biomaterials, **79**, 142–150 (2006).
DOI: 10.1002/jbm.b.30524

[24] Garrec D. L., Gori S., Luo L., Lessard D., Smith D. C., Yessine M. A., Ranger M., Leroux J. C.: Poly(*N*-vinylpyrrolidone)-block-poly(D,L-lactide) as a new polymeric solubilizer for hydrophobic anticancer drugs: *In vitro* and in vivo evaluation. Journal of Controlled Release, **99**, 83–101 (2004).
DOI: 10.1016/j.jconrel.2004.06.018

[25] Lee H., Lee E., Kim D. K., Jang N. K., Jeong Y. Y., Jon S.: Antibiofouling polymer-coated superparamagnetic iron oxide nanoparticles as potential magnetic resonance contrast agents for in vivo cancer imaging. Journal of American Chemical Society, **128**, 7383–7389 (2006).
DOI: 10.1021/ja061529k

[26] Kohler N., Fryxell G. E., Zhang M.: A bifunctional poly(ethylene glycol) silane immobilized on metallic oxide-based nanoparticles for conjugation with cell targeting agents. Journal of American Chemical Society, **126**, 7206–7211 (2004).
DOI: 10.1021/ja049195r

[27] Feng B., Hong R. Y., Wang L. S., Guo L., Li H. Z., Ding J., Zheng Y., Wei D. G.: Synthesis of Fe_3O_4/APTES/PEG diacid functionalized magnetic nanoparticles for MR imaging. Colloids and Surfaces A: Physicochemical and Engineering Aspects, **328**, 52–59 (2008).
DOI: 10.1016/j.colsurfa.2008.06.024

[28] Barrera C., Herrera A. P., Rinaldi C.: Colloidal dispersions of monodisperse magnetite nanoparticles modified with poly(ethylene glycol). Journal of Colloid and Interface Science, **329**, 107–113 (2009).
DOI: 10.1016/j.jcis.2008.09.071

[29] Cao H., He J., Deng L., Gao X.: Fabrication of cyclodextrin-functionalized superparamagnetic Fe_3O_4/amino-silane core-shell nanoparticles via layer-by-layer method. Applied Surface Science, **225**, 7974–7980 (2009).
DOI: 10.1016/j.apsusc.2009.04.199

[30] Fan Q-L., Neoh K-G., Kang E-T., Shuter B., Wang S-C.: Solvent-free atom transfer radical polymerization for the preparation of poly(poly(ethyleneglycol) monomethacrylate)-grafted Fe_3O_4 nanoparticles: Synthesis, characterization and cellular uptake. Biomaterials, **28**, 5426–5436 (2007).
DOI: 10.1016/j.biomaterials.2007.08.039

[31] Yong Y., Bai Y., Li Y., Lin L., Cui Y., Xia C.: Preparation and application of polymer-grafted magnetic nanoparticles for lipase immobilization. Journal of Magnetism and Magnetic Materials, **320**, 2350–2355 (2008).
DOI: 10.1016/j.jmmm.2008.04.158

[32] Massart R., Cabuil V.: Effect of some parameters on the formation of colloidal magnetite in alkaline medium: Yield and particle size control. Journal of Chemical Physics, **84**, 967–973 (1987).

[33] Jain T. K., Richey J., Strand M., Leslie-Plecky D. L., Flask C. A., Labhasetwar V.: Magnetic nanoparticles with dual functional properties: Drug delivery and magnetic resonance imaging. Biomaterials, **29**, 4012–4021 (2008).
DOI: 10.1016/j.biomaterials.2008.07.004

[34] Brusentsov N. A., Gogosov V. V., Brusentsova T. N., Sergeev A. V., Jurchenko N. Y., Kuznetsov A. A., Kuznetsov O. A., Shumakov L. I.: Evaluation of ferromagnetic fluids and suspensions for the site-specific radiofrequency-induced hyperthermia of MX11 sarcoma cells in vitro. Journal of Magnetism and Magnetic Materials, **225**, 113–117 (2001).
DOI: 10.1016/S0304-8853(00)01238-5

[35] Xu C. J., Xu K. M., Gu H. W., Zhong X. F., Guo Z. H., Zheng R., Zhang X., Xu B.: Nitrilotriacetic acid-modified magnetic nanoparticles as a general agent to bind histidine-tagged proteins. Journal of American Chemical Society, **126**, 3392–3393 (2004).
DOI: 10.1021/ja031776d

[36] Gillis P., Koenig S. H.: Transverse relaxation of solvent protons induced by magnetized spheres: Application to ferritin, erythrocytes, and magnetite. Magnetic Resonance in Medicine, **5**, 323–345 (1987).
DOI: 10.1002/mrm.1910050404

[37] Wang Y-X. J., Hussain S. M., Krestin G. P.: Superparamagnetic iron oxide contrast agents: Physicochemical characteristics and applications in MR imaging. European Radiology, **11**, 2319–2331 (2001).
DOI: 10.1007/s003300100908

eXPRESS Polymer Letters Vol.4, No.6 (2010) 339–345
Available online at www.expresspolymlett.com
DOI: 10.3144/expresspolymlett.2010.43

Influence of multi-walled carbon nanotubes on the β form crystallization of syndiotactic polystyrene at low temperature

A. Sorrentino[*], *L. Vertuccio, V. Vittoria*

Chemical and Food Engineering Department – University of Salerno, via Ponte Don Melillo – 84084 Fisciano (SA), Italy

Received 28 December 2009; accepted in revised form 23 March 2010

Abstract. Syndiotactic polystyrene (sPS) samples were quenched at low temperature (0°C) in the presence of Multi-Walled Carbon Nanotubes (MWCNT) at different concentrations. The influence of carbon nanotubes on the structure and physical properties of sPS composites was investigated by SEM, X-ray diffractograms, DSC (Differential Scanning Calorimetry), and Dynamic Mechanical Analysis (DMA). A good dispersion of the carbon nanotubes in the sPS matrix was found, at least for the low MWCNT concentration, whereas opposite effects were noticed on T_g and elastic modulus, depending on concentration. The pristine sPS sample was almost amorphous at 0°C, whereas in the filled samples the crystallinity increased on increasing the MWCNT concentration, indicating a strong nucleation effect of the nanotubes. Interestingly, in spite of the low temperature, the β crystallinity was induced and this crystalline form increases on increasing the carbon nanotube concentration, being dominant (68% of the total crystallinity) already at 3 wt% of MWCNT concentration.

Keywords: *nanocomposites, polymer crystallization, multi-wall carbon nanotubes, syndiotactic polystyrene, morphology*

1. Introduction

In semicrystalline polymer materials, the degree of crystallinity, the orientation, the polymorphism and the thermodynamic state of the amorphous phase are important factors in controlling the physical properties. Many efforts have been devoted in the past to settle a correlation picture between these parameters and the processing conditions [1]. This is particularly relevant for syndiotactic polystyrene (sPS) that presents a complex polymorphic pattern, depending on several factors, further complicated by the presence of structural disorder [2–5]. In particular, when crystallized from the molten state, sPS solidifies into two different crystal forms, termed α and β. They can appear pure or mixed in different proportions, depending on the experimental conditions [1, 6, 7].

Controlling of processing conditions to obtain a pure α or β form is of particular interest especially in consideration of their different physical properties [2, 6]. For example, sPS samples in the crystalline α form, as well as amorphous samples, when exposed to suitable solvents transform into clathrate forms, characterized by chains in helical conformation. This transition never occurs in samples that present crystalline β form [2]. For this reason, the sPS β form could represent a polymeric material of industrial interest due to its high melting temperature, fast crystallization rate, good chemical and thermal resistance [2, 5]. However, in spite of its thermodynamic higher stability with respect to the α form, it can be obtained only at very low under-cooling (high crystallization temperature), whereas at crystallization temperatures

[*]Corresponding author, e-mail: asorrentino@unisa.it

lower than 230°C the α form is always obtained [8].

Many attempts to obtain the β form at lower temperatures failed so far. Polymorphic state has been only altered in the presence of miscible polymers, such as poly(2,6-dimethyl-p-phenylene oxide) [9] or atactic polystyrene, which reduced in sPS blends the α form crystallinity, increasing the β form [10, 11].

Recent experimental investigations are demonstrating the potential of carbon nanotubes as small-volume fraction reinforcements in polymer matrix systems [12–17].

Carbon nanotubes are also known to impart profound changes to the crystallization behavior of semicrystalline polymers. They can affect the crystalline morphology [18] and modify the kinetics of the crystallization process as a result of their nucleating action [19–20]. Furthermore, carbon nanotubes may induce polymorphism in certain systems and promoting crystallization into specific crystal forms [21, 22].

In this paper we show the enhanced crystallization of sPS in the β form, in the presence of multi-walled carbon nanotubes (MWCNT), even at very low crystallization temperatures. The possibility of inducing the β form crystallization at low temperatures (close to the common processing conditions) is very important because in this way several polymer properties were improved, such as mechanical and thermal properties.

2. Experimental

2.1. Materials

Syndiotactic polystyrene (*Questra QA101*) was supplied by the *Dow Chemical Co* (USA). The molecular weight characteristics were: M_w = 320 000 g/mol and M_w/M_n = 3.9, whereas a concentration of syndiotactic triads was greater than 98% [6].

The carbon nanotubes were obtained from *Nanocyl S. A.* (Belgium) synthesized by catalytic carbon vapor deposition (ccvd) process. They are multi-walled carbon nanotubes characterized by an average diameter of about 10 nm and the length ranging from 0.1 to 10 μm. The nanotubes were purified to produce a carbon purity >95% and a metal oxide impurity <5% as it results by thermogravimetric analysis (TGA). The specific surface area determined with the BET method is around 250–300 m_2/g [17].

Neat sPS sample and the composite materials containing different concentration of multi-walled carbon nanotubes (1, 3, 6 and 9 wt%) were prepared using a laboratory-scale conical twin-screw extruder '*Micro-Coumpounder*' by *ThermoHaake* (Germany). Polymers and carbon nanotubes were premixed manually and then loaded into the compounder. All batches, weighing 6 g each, were processed at 295°C with a screw speed of 100 rpm for 15 min. The samples were then extruded and cooled down to room temperature. The extruded samples were moulded in a hot press by *Carver Inc.* (USA) at 310°C, forming 100 μm thick films, which were rapidly quenched in a bath with water at 0°C.

2.2. Methods

Differential Scanning Calorimetry (DSC) analysis was carried out on films samples with a mass ranging between 5 and 7 mg. The tests were carried out by means of a *DSC 822* by *Mettler Toledo* (Germany) under nitrogen atmosphere. The samples were heated from 25 to 300°C at 10°C/min and kept at 300°C for 5 min to eliminate the previous thermal history. After that, non isothermal melt-crystallization study was carried out by cooling the samples to 30°C at a rate of 10°C/min.

X-ray diffraction (XRD) measurements were performed on the sample films by means of a *D8 Advance by Bruker* (USA) X-ray diffractometer with Ni-filtered CuK_α radiation (λ = 1.5405 Å). Data were collected from 2 to 40° in 2θ in steps of 0.03°at a time /step of 0.02 sec.

Scanning electron microscopy (SEM) was conducted using a *JSM-5900LV* by *JEOL* (USA) scanning electron microscope. The films were etched before of the observation. The etching reagent was prepared by stirring 1.0 g potassium permanganate in a solution mixture of 95 ml sulphuric acid (95–97%) and 48 ml orthophosphoric acid (85%). The samples were immersed into the fresh etching reagent at room temperature and held under agitation for 48 hours. Subsequent washings were done using a cold mixture of 2 parts by volume of concentrated sulfuric acid and 7 parts of water. Furthermore the samples were washed successively with 30% aqueous hydrogen peroxide to remove

any manganese dioxide. The samples were washed with distilled water and kept under vacuum for 2 days.

Thermo-mechanical properties of the different blends were determined with a dynamic thermo-mechanical analyzer, *DMA 2980* by *TA instrument* (USA). Quenched film samples with dimensions 5×10×0.1 mm were tested by applying a variable tensile deformation. The displacement amplitude was set to 1%, whereas the measurements were performed at the frequency of 1 Hz. The range of temperature was from 0 to 150°C at a scanning rate of 3°C/min.

3. Results and discussion

3.1. Samples morphology

In Figure 1 the morphology of pristine sPS and the sample containing 1 wt% of MWCNT are compared. In the pristine sample the etching procedure erased the surface sheet, putting in evidence an almost structure-less morphology, typical of an amorphous sample.

The filled sample appears very similar, and no recognizable morphology is seen in the polymeric matrix; at variance a very homogeneous network of carbon nanotubes is clearly visible. They are nicely dispersed and do not show any bundle aggregate, going separately out of the polymeric matrix. This means that at the concentration of 1 wt% it is possible to disperse well the carbon nanotubes into the syndiotactic polystyrene matrix, producing a homogeneous sample. Further and deeper analyses, such as TEM, are needed to verify if the good dispersion is a general feature of the sPS-CNT composites, even for high concentrations.

3.2. Differential Scanning Calorimetry (DSC)

The DSC scans of sPS and sPS-MWCNT films quenched at 0°C are shown in Figure 2, during the first heating (Figure 2a) at 10°C/min and successive cooling (Figure 2b) always at 10°C/min. In the heating of the neat sPS sample it is clearly observed a deflection from the baseline in the range 80–100°C, due to the amorphous glass transition, an

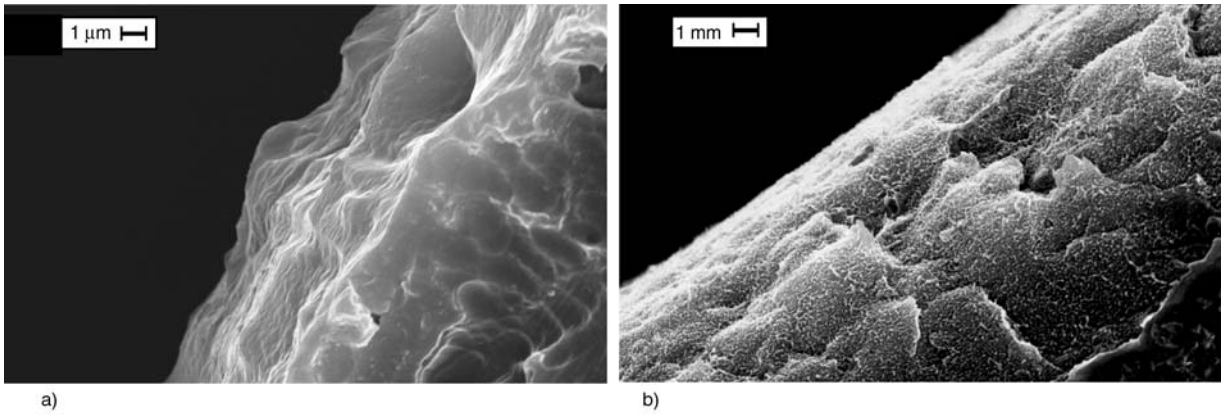

Figure 1. Scanning electron microscopy of selected samples. a) neat sPS; b) sPS containing 1 wt% of MWCNT

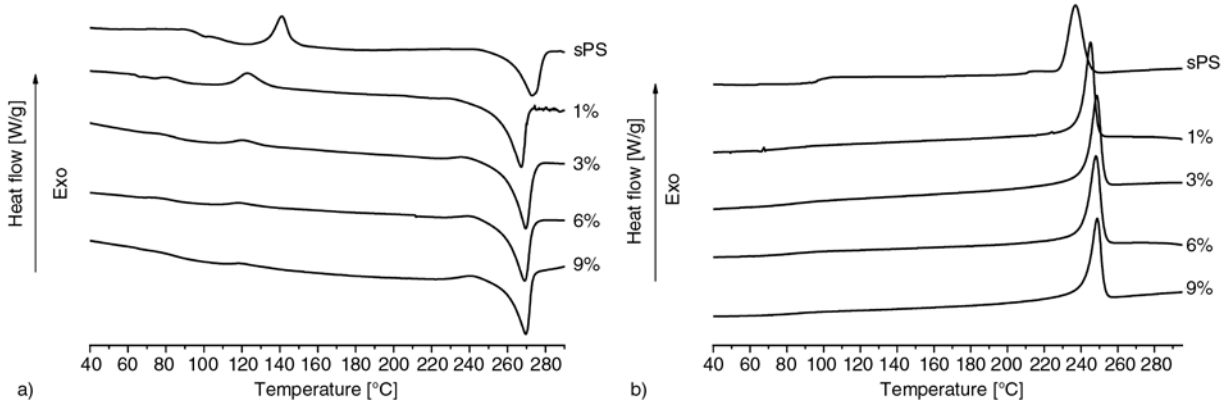

Figure 2. DSC curves of the reported samples: a) heating scan at 10°C/min of the quenched samples; b) cooling scan at 10°C/min of the same samples after the annealing step at 300°C

exothermic peak due to the cold crystallization and the melting peak. The jump at the glass transition temperature (T_g) is quite evident in the pristine sPS sample, whereas it appears at lower temperatures and is less evident in the composites. The subsequent exothermic peak due to the cold crystallization indicates that the pure sPS films quenched at 0°C is prevalently amorphous and crystallizes during the heating scan. At variance this peak is reduced in the sample containing MWCNT up to fully disappear in the samples with 6 and 9 wt% of MWCNT.

It is interesting to note that the cold crystallization temperature ($T_{c(heating)}$) (the temperature of the exothermic peak) decreases by almost 20°C going from the pure to the composite samples, indicating a nucleation effect due to the carbon nanotubes [19, 20].

This effect is also detectable during the cooling scan from the melt state, in which the crystallization temperature ($T_{c(cooling)}$) of the composite samples is always higher than that of the neat sPS.

The melting temperatures (T_m) are slightly lower in the composite samples. This is due to the fact that the crystals formed during the DSC heating scan have a melting temperature higher than that formed during the rapid quenching at 0°C.

All the thermal parameters are reported in Table 1, in which also the crystallinity (X_c), evaluated using the following Equation (1) is reported:

$$X_c = \frac{\Delta H_m - \Delta H_c}{\Delta H_\infty} \cdot 100 \quad (1)$$

where ΔH_c and ΔH_m are the enthalpy of cold crystallization and fusion recorded by DSC, and ΔH_∞ is the heat of fusion for 100% crystalline sPS (taken to be 53.2 J/g [23]).

The enthalpies, and consequently the crystallization degree, reported in Table 1, are normalized to the polymer mass.

It is important to note that this method tends to overestimate the value of crystallinity in presence of mesophase and/or melting – re-crystallization processes during the heating scan at temperatures close to the melting point. In particular, the formations of an instable mesophase during the crystallization of sPS at lower temperature, was clearly observed in the literature [2, 8]. Even if the conformational order of the chain sequences is not sufficient to give rise to discrete X-ray reflections, the presence of mesomorphic phase can be characterized by infrared spectroscopy as well as permeability tests [8].

It is also evident that increasing the MWCNT concentration the crystallinity increases, being almost double with respect to the pure sPS for the samples with 3, 6 and 9 wt% nanotubes. The shift of the glass transition temperature at lower temperatures is also worth noting in all the composite samples. Probably, as observed in other polymer nanocomposites systems, the presence of CNT in the matrix induces an increase of free volume, and consequently an increase in the molecular mobility at lower temperature [24, 25].

3.3. X-ray analysis

In Figure 3 the X-ray diffractograms of the pure sPS and all the sPS-MWCNT composites are shown. The pure sPS sample is almost completely

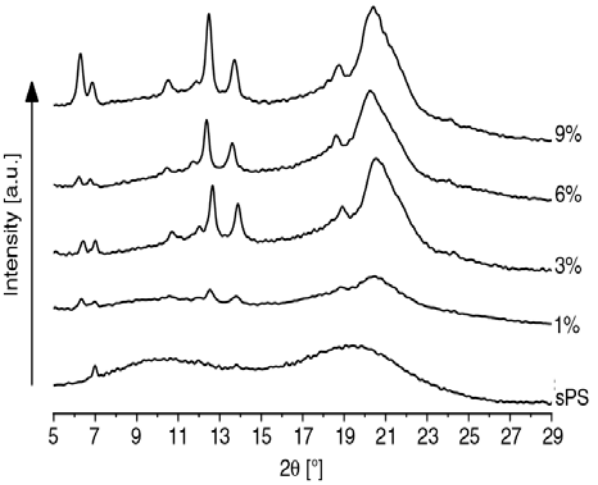

Figure 3. X-ray powder spectra of the reported samples

Table 1. DSC results for the reported samples

%MWCNT	T_g [°C]	$T_{c(heating)}$ [°C]	$\Delta H_{c(heating)}$ [J/g]	T_m [°C]	ΔH_m [J/g]	X_c [%]	$T_{c(cooling)}$ [°C]	$\Delta H_{c(cooling)}$ [J/g]
sPS	97.5	141	11.26	273	24.29	24	237	24.30
1	81.0	123	7.42	267	28.91	40	245	26.78
3	84.0	120	2.51	270	30.46	52	248	29.44
6	85.0	119	1.44	269	29.04	52	248	28.52
9	83.0	120	1.29	269	30.89	56	249	27.32

amorphous: indeed only a small peak at 6.8° of 2θ, characteristic of the α form [2, 3] is apparent in the diffractogram. This is an expected result, always found for quenching at low temperatures.

At variance, all the composites appear crystalline, with this parameter increasing on increasing the carbon nanotube concentration, confirming the DSC results. Moreover the crystalline diffractograms surprisingly show the presence of peaks characteristic of the β form, never observed at crystallization temperature as low as 0°C. Indeed the peaks at 6.2 and 12.3° of 2θ typical of the β form [2, 3] are evident in the sample containing 1 wt% of MWCNT, and their intensity increases on increasing the nanotube concentration. Also the peaks characteristic of the α form are present in the diffractograms, in particular the peaks at 6.8 and 11.8° of 2θ [2, 3]. However, at variance with the β form peaks, the α form peaks decrease on increasing the nanotube concentration, indicating that the nanotubes strongly favor the β crystallization. The total crystallinity was derived from the diffractograms by comparing the crystalline peak area with the total area of the diffractograms. The obtained values are reported in Table 2. The X-ray analysis, which represents the crystallinity of the quenched samples (not invalidated by further crystallization as in DSC), shows a dramatic increase of crystallinity from the pure sPS sample (3%) and the sample with 3 wt% of MWCNT (36%), confirming the qualitative behavior deduced in the DSC analysis.

To investigate the variation of the β form crystallinity on increasing the nanotube concentration, the formula of Guerra *et al.* [8] was used for calculating the β fraction.

It consists of determining the areas (I) of the two peaks located at 2θ = 11.6° (α form) and 2θ = 12.2 (β form), and deriving the percentage of β form by the Equation (2) where 1.8 is ratio between the intensities of peaks at 11.6 and 12.2° of 2θ, for sample of equal thickness and crystallinity in the pure α and β form, respectively:

$$P_\beta = \left[1 - \frac{\frac{1.8 \cdot I_{(11.6°)}}{I_{(12.2°)}}}{1 + \frac{1.8 \cdot I_{(11.6°)}}{I_{(12.2°)}}} \right] \cdot 100 \quad (2)$$

In Table 2 the also the relative P_β crystallinity are reported. A strong increase of both the total and the β crystallinity is clearly observed on increasing the carbon nanotube concentration, with the β form being dominant (68% of the total crystallinity) already at 3 wt% of MWCNT concentration.

Table 2. XRD results for the reported samples

$\%_{MWCNT}$	X_c [%]	P_β [%]
sPS	3	0
1	18	33
3	36	68
6	34	77
9	39	83

3.4. Dynamic mechanical properties

Figure 4 shows the tensile storage modulus (E') and the glass transition temperature (T_g), resulting from the DMA characterization of the samples.

MWCNT addition increases the storage modulus of the composites for all the concentrations. The glass transition temperature (identified as the temperature where the tanδ presents a peak) after a sudden decrease, increases on increasing the MWCNT concentration. Even if this trend was confirmed by the experimental results found in the DSC analysis (Figure 2a), it is difficult to explain. It probably corresponds to an overlapping of different effects related to the free volume, the crystallinity of sPS matrix, the relaxation of the rigid amorphous phase immobilized by carbon nanotubes and inter-phase interactions [26]. At low CNT concentration the increase of free volume, determining an increase of chain mobility prevails, determining a decrease of the T_g, whereas at high CNT concentration the

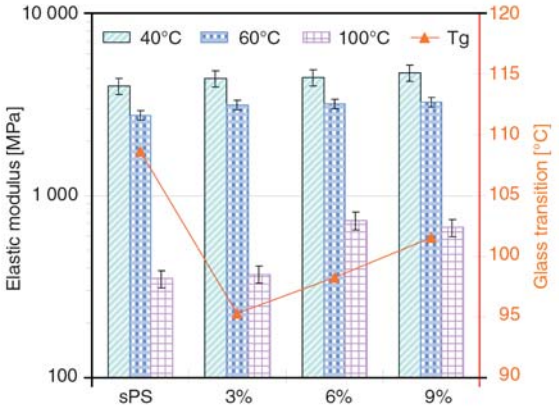

Figure 4. Storage modulus at 40, 60 and 100°C and glass transition temperature as a function of nanotubes concentration as calculated by the DMA tensile tests

increasing amount of filler increases the restrictions imposed to the motion of the polymer chains, which can explain the increase after the initial drop. The decrease in the chain mobility and principally the consistent increase of crystallinity can explain also the enhancement in the elastic modulus. A similar behaviour was described in [27] for another semicrystalline polymer-nanocomposite system (PA6-MWCNT composites).

4. Conclusions

The influence of carbon nanotubes on the structure and physical properties of sPS composites has been investigated by different methods, giving the following results:

- The chosen processing conditions allows, at least for low concentrations, a good dispersion of the carbon nanotubes in the sPS matrix.
- As evidenced by DMA and DSC analysis, the glass transition decreases in the filled samples, indicating that the effect of carbon nanotubes on the amorphous phase of sPS produce different and opposing effects.
- The pristine sPS sample is almost amorphous at 0°C, whereas in the filled samples the crystallinity increases on increasing the MWCNT concentration, indicating a strong nucleation effect of the nanotubes.
- The β crystallinity increases on increasing the carbon nanotube concentration, being dominant (68% of the total crystallinity) already at 3 wt% of MWCNT concentration.
- MWCNT addition increases the storage modulus of the composites for all the concentrations.

References

[1] Sorrentino A., De Santis F., Titomanlio G.: Polymer crystallization under high cooling rate and pressure: A step towards polymer processing conditions. in 'Lecture notes in physics: Progress in understanding of polymer crystallization' (eds.: Reiter G., Strobl G.) Springer, Berlin, Vol 714, 329–344 (2007).

[2] Sorrentino A., Vittoria V.: Structure, morphology, and crystallization behavior of syndiotactic polystyrene. in 'Syndiotactic polystyrene: Synthesis, characterization, processing, and applications' (ed.: Schellenberg J.) Wiley, Chichester, 157–194 (2009).

[3] De Rosa C., de Ballesteros O. R., Di Gennaro, M., Auriemma, F.: Crystallization from the melt of α and β forms of syndiotactic polystyrene. Polymer, **44**, 1861–1870 (2003).
DOI: 10.1016/S0032-3861(02)00885-6

[4] De Rosa C.: Crystal structure of the trigonal modification (α form) of syndiotactic polystyrene. Macromolecules, **29**, 8460–8465 (1996).
DOI: 10.1021/ma960905q

[5] Greis O., Asano T., Xu Y., Petermann J.: Morphology and structure of syndiotactic polystyrene. Polymer, **30**, 590–594 (1989).
DOI: 10.1016/0032-3861(89)90140-7

[6] Sorrentino A., Pantani R., Titomanlio G.: Kinetics of melting and characterization of the thermodynamic and kinetic properties of syndiotactic polystyrene. Journal of Polymer Science Part B: Polymer Physics, **45**, 196–207 (2007).
DOI: 10.1002/polb.21039

[7] Sorrentino A., Pantani R., Titomanlio G.: Melting and zero growth rate temperatures of syndiotactic polystryrene. Colloid and Polymer Science, **286**, 983–991 (2008).
DOI: 10.1007/s00396-008-1858-2

[8] Guerra G., Vitagliano V., De Rosa C., Petraccone V., Corradini P.: Polymorphism in melt crystallized syndiotactic polystyrene samples. Macromolecules, **23**, 1539–1544 (1990).
DOI: 10.1021/ma00207a050

[9] Dikshit A. K., Kaito A.: Effects of the oriented mesophase on the cold crystallization of syndiotactic polystyrene and its blend with poly(2,6-dimethyl-1,4-phenylene oxide). Journal of Polymer Science Part B: Polymer Physics, **41**, 1665–1675 (2003).
DOI: 10.1002/polb.10520

[10] Woo E. M., Sun Y. S., Yang C-P.: Polymorphism, thermal behavior, and crystal stability in syndiotactic polystyrene vs. its miscible blends. Progress in Polymer Science, **26**, 945–983 (2001).
DOI: 10.1016/S0079-6700(01)00010-7

[11] Guerra G., De Rosa C., Vitagliano V. M., Petraccone V., Corradini P.: Effects of blending on the polymorphic behavior of melt-crystallized syndiotactic polystyrene. Journal of Polymer Science Part B: Polymer Physics, **29**, 265–271 (1991).
DOI: 10.1002/polb.1991.090290301

[12] Shaffer M. S. P., Windle A. H.: Fabrication and characterization of carbon nanotube/poly(vinyl alcohol) composites. Advanced Material, **11**, 937–941 (1999).
DOI: 10.1002/(SICI)1521-4095(199908)11:11<937::AID-ADMA937>3.0.CO;2-9

[13] Quian D., Dickey E. C., Andrews R., Rantell T.: Load transfer and deformation mechanisms in carbon nanotube-polystyrene composites. Applied Physic Letters, **76**, 2868–2870 (2000).
DOI: 10.1063/1.126500

[14] Kashiwagi T., Grulke E., Hilding J., Harris R., Awad W., Douglas J.: Thermal degradation and flammability properties of poly(propylene)/carbon nanotube composites. Macromolecular Rapid Communication, **23**, 761–765 (2002).
DOI: 10.1002/1521-3927(20020901)23:13<761::AID-MARC761>3.0.CO;2-K

[15] Andrews R., Weisenberger M. C.: Carbon nanotube polymer composites. Current Opinion in Solid State and Materials Science, **8**, 31–37 (2004).
DOI: 10.1016/j.cossms.2003.10.006

[16] Ajayan P. M., Zhou O. Z.: Applications of carbon nanotubes. in 'Carbon nanotubes: Synthesis, structure, properties, and applications' (eds.: Dresselhaus M. S., Dresselhaus G., Avouris P.) Springer, Berlin, 386–421 (2000).

[17] Guadagno L., Vertuccio L., Sorrentino A., Raimondo M., Naddeo C., Vittoria V., Iannuzzo G., Calvi E., Russo S.: Mechanical and barrier properties of epoxy resin filled with multi-walled carbon nanotubes. Carbon, **47**, 2419–2430 (2009).
DOI: 10.1016/j.carbon.2009.04.035

[18] Jeon K., Lumata L., Tokumoto T., Steven E., Brooks J., Alamo R. G.: Low electrical conductivity threshold and crystalline morphology of single-walled carbon nanotubes – High density polyethylene nanocomposites characterized by SEM, Raman spectroscopy and AFM. Polymer, **48**, 4751–4764 (2007).
DOI: 10.1016/j.polymer.2007.05.078

[19] Sandler J. K. W., Pegel S., Cadek M., Gojny F. H., van Es M., Lohmar J., Blau W. J., Schulte K., Windle A. H., Shaffer M. S. P.: A comparative study of melt spun polyamide-12 fibres reinforced with carbon nanotubes and nanofibres. Polymer, **45**, 2001–2015 (2004).
DOI: 10.1016/j.polymer.2004.01.023

[20] Probst O., Moore E. M., Resasco D. E., Grady B. P.: Nucleation of polyvinyl alcohol crystallization by single-walled carbon nanotubes. Polymer, **45**, 4437–4443 (2004).
DOI: 10.1016/j.polymer.2004.04.031

[21] Sarno M., Gorrasi G., Sannino D., Sorrentino A., Ciambelli P., Vittoria V.: Polymorphism and thermal behaviour of syndiotactic poly(propylene)/carbon nanotube composites. Macromolecular Rapid Communications, **25**, 1963–1967 (2004).
DOI: 10.1002/marc.200400344

[22] Li J. A., Fang Z. P., Tong L. F., Gu A. J., Liu F.: Polymorphism of nylon-6 in multiwalled carbon nanotubes/nylon-6 composites. Journal of Polymer Science Part B: Polymer Physics, **44**, 1499–1512 (2006).
DOI: 10.1002/polb.20808

[23] Pasztor A. J., Landes B. G., Karjala P. J.: Thermal properties of syndiotactic polystyrene. Thermochimica Acta, **177**, 187–195 (1991).
DOI: 10.1016/0040-6031(91)80095-Z

[24] Drozdov A. D., Christiansen J. C., Gupta R. K., Shah A. P.: Model for anomalous moisture diffusion through a polymer-clay nanocomposite. Journal of Polymer Science Part B: Polymer Physics, **41**, 476–492 (2003).
DOI: 10.1002/polb.10393

[25] Sorrentino A., Gorrasi G., Tortora M., Vittoria V.: Barrier properties of polymer/clay nanocomposites. in 'Polymer nanocomposites' (eds.: Mai Y-W., Yu Z-Z.) Woodhead, Cambridge (273–292) (2006).

[26] Pantani R., Sorrentino A.: Pressure effect on viscosity for atactic and syndiotactic polystyrene. Polymer Bulletin, **54**, 365–376 (2005).
DOI: 10.1007/s00289-005-0397-y

[27] Logakis E., Pandis C., Peoglos V., Pissis P., Stergiou C., Pionteck J., Pötschke P., Micušík M., Omastová M.: Structure-property relationships in polyamide 6/multi-walled carbon nanotubes nanocomposites. Journal of Polymer Science Part B: Polymer Physics, **47**, 764–774 (2009).
DOI: 10.1002/polb.21681

eXPRESS Polymer Letters Vol.4, No.6 (2010) 346–354
Available online at www.expresspolymlett.com
DOI: 10.3144/expresspolymlett.2010.44

Synthesis, characterization and thermal decomposition of poly(decamethylene 2,6-naphthalamide)

S. H. Yang[1], P. Fu[1], M. Y. Liu[1], Y. D. Wang[1], Z. P. Li[2], Q. X. Zhao[1]*

[1]School of Materials Science and Engineering, Zhengzhou University, 75 Daxue Road, Zhengzhou 450052, People's Republic of China
[2]Radiation Processing Center, Henan Academy of Sciences, 7 Songshan Road, Zhengzhou 450015, People's Republic of China

Received 8 February 2010; accepted in revised form 29 March 2010

Abstract. A novel engineering plastic, poly(decamethylene 2,6-naphthalamide) (PA10N) was prepared via a reaction of 2,6-naphthalene dicarboxylic acid and 1,10-decanediamine. The structure of synthesized PA10N was characterized by elemental analysis, Fourier transform infrared (FT-IR) spectroscopy and proton nuclear magnetic resonance (^{1}H-NMR). The thermal behavior was determined by differential scanning calorimetry (DSC), thermo-gravimetric analysis (TGA) and dynamic mechanical analysis (DMA). Melting temperature (T_m), glass transition temperature (T_g) and decomposition temperature (T_d) of PA10N are 320, 144 and 495°C, respectively. The solubility, water-absorbing capacity, and mechanical properties of PA10N have also been investigated. Pyrolysis products and thermal decomposition mechanism of PA10N were analyzed by flash pyrolysis-gas chromatography/mass spectrometry (Py-GC/MS). The results show that the heat resistance and mechanical properties of PA10N are near to those of poly(nonamethylene terephthalamide) (PA9T), and PA10N is a promising heat-resistant and processable engineering plastic.

Keywords: *mechanical properties, thermal properties, polyamides, synthesis, decomposition*

1. Introduction

Aromatic polyamides and semiaromatic polyamides have been widely used in many industrial and commercial applications, especially in surface-mount technology (SMT) and automobile industries, by virtue of their excellent characteristics such as good thermal stability, chemical resistance, low creep and high modulus [1–3]. The commonly mentioned aromatic and semiaromatic polyamides can not be processed by melting method due to their high melting temperature and relatively lower decomposition temperatures [4–6]. Therefore, several approaches have been made through synthetic modification by the incorporation of flexible linkages [7, 8], bulky pendant groups [9] and noncoplanar biphenylene moieties [10] into the polymer backbones. Poly(nonamethylene terephthalamide) (PA9T) inherits the merits of the heat resistance of aromatic polyamides and the processing ability of aliphatic polyamides [11]. However, the high cost of PA9T limited its applications.

In order to increase the processing ability and decrease the cost of semiaromatic polyamides, long flexible aliphatic chains are usually introduced into their backbones [12–14]. It has been reported that diacids with long molecular chains can be prepared from petroleum fermentation process using light wax as raw material [15], and the long chain diamines can be prepared from the corresponding long chain diacids by cyanation and amination process [16]. The cost of obtained long chain diacids and diamines was reduced accordingly. It

*Corresponding author, e-mail: zhaoqingxiang1@126.com

was noticeable that naphthalene-ring can be also introduced into the molecular main chain of semiaromatic polyamides and high thermal stability was retained expectably. However, the semiaromatic polyamides containing naphthalene-ring were presented relatively low molecular weight and unsatisfactory performance which would not meet the requirements for commercialization [17, 18]. Therefore, it is of great significance to synthesize novel, low-cost, high-performance and processability semiaromatic polyamides containing naphthalene-ring.

Semiaromatic polyamides are widely used in many demanding applications where the properties of thermal stability and flame resistant are priorities [19]. Taking into account this high practical interest, it is important to study the thermal decomposition behavior of semiaromatic polyamides [20, 21]. Pyrolysis-gas chromatography/mass spectrometry (Py-GC/MS) is well established as a method for the analysis of the thermal decomposition of polymers [22–24]. The investigation of Py-GC/MS can provide unique information on the primary processes of the thermal decomposition of polymers and also important structural information, such as structural identification of homopolymers, differentiation of isomeric structures, copolymer composition, etc.

In this work, the PA10N was successfully synthesized by the polycondensation reaction of 2,6-naphthalene dicarboxylic acid and 1,10-decanediamine in water. PA10N was investigated by Fourier transform infrared (FT-IR) spectroscopy, proton nuclear magnetic resonance (^{1}H-NMR) and elemental analysis. The thermal property was studied by differential scanning calorimetry (DSC), thermogravimetric analysis (TGA) and dynamic mechanical analysis (DMA). The thermal decomposition process was analyzed by Py-GC/MS. The solubility, intrinsic viscosity, inherent viscosity, water-absorbing capacity and mechanical properties of PA10N were also studied.

2. Materials and methods

2.1. Materials

2,6-naphthalene diacrboxylic acid was purchased from Mitsubishi Gas Chemical Company, Inc (MGC, Japan). 1,10-decanediamine was provided commercially by Zibo Guangtong Chemical Co. Ltd (China), and purified by vacuum distillation prior to use.

2.2. Synthesis of PA10N

PA10N was prepared from the reaction of 2,6-naphthalene dicarboxylic acid and 1,10-decanediamine through a three-step procedure: salt formation, prepolymerization and solid-state polymerization (Figure 1).

1,10-decanediamine (258 g, 1.5 mol) was dissolved in distilled water (1000 ml) at 80°C. Then the solution was added slowly into 500 ml of distilled water mixture of 2,6-naphthalene diacrboxylic acid (324 g, 1.5 mol) with vigorous stirring and then stirred for 2 h at 80°C. Finally a slight excess of 1,10-decanediamine (2 g, 0.01 mol) was added into the solution with continuous stirring for 1 h at 80°C. The pH value of the solution was adjusted to 7.2. The white 1,10-decanediamine-2,6-naphthalene diacrboxylic acid salt (PA10N salt) precipitated from the solution.

After filtering over a Buchner funnel and drying in a vacuum desiccator for 12 h, the white salt of PA10N (553 g) and distilled water (500 ml) were added into an autoclave. The autoclave was filled with carbon dioxide and then heated to 240°C while increasing the pressure to 2.6 MPa. After 2 h, the pressure of the autoclave was gradually decreased to normal pressure in 2 h by deflating and the reaction temperature of the autoclave was increased to 255°C. After reaction for another 1.5 h, the ivory-white prepolymer of PA10N was obtained (503 g).

The prepolymer of PA10N was ground into particles with diameter of 0.1~2 mm and dried at 90°C in a vacuum oven for 4 h. Then the prepolymer of PA10N was added into a solid-state polymerization kettle, the reaction was carried out at 250°C for 15 h with a vacuum of 10 Pa. Finally, the kettle was cooled to room temperature and straw yellow polymer of PA10N was obtained (478 g).

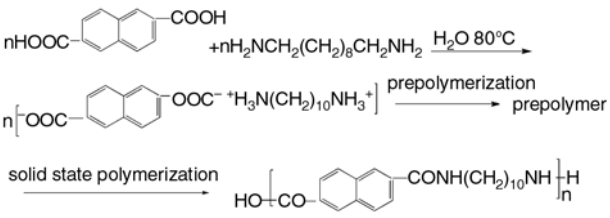

Figure 1. The synthetic route of PA10N

2.3. Characterization of PA10N

FT-IR, ^{1}H-NMR and elemental analysis were used to confirm the structure of PA10N. The thermal behavior was determined by DSC, TGA and DMA. Thermal decomposition mechanisms of PA10N were analyzed by Py-GC/MS. The solubility, intrinsic viscosity, inherent viscosity, water-absorbing capacity and mechanical property of PA10N were also studied.

The intrinsic viscosity and inherent viscosity of PA10N dissolved in concentrated sulfuric acid was determined in an Ubbelohde viscometer at 25±0.1°C. The water-absorbing of PA10N was measured according to GB/T 1034 (Chinese standard).

The FT-IR measurement was carried out on a NICOLET 460 spectrometer. ^{1}H-NMR spectra was recorded with a Bruker DPX-400 (400 MHz), using deuterated trifluoroacetic acid as solvents and tetramethylsilane (TMS) as an internal reference. Elemental analysis was performed on a Perkin-Elmer 2400 CHNS/O elemental analyzer at 975°C under nitrogen.

Thermal analysis (DSC and TGA) was recorded on a NETSCH 204 calorimeter with a heating rate of 10°C·min^{-1} in a nitrogen stream. DMA was carried out on a NETZSCH DMA-242 apparatus operating in the bending mode at 1 Hz and a heating rate 3°C·min^{-1} from –170 to 170°C.

All samples for mechanical tests were prepared by injection molding. The Izod impact strength was measured according to GB/T 1843 (Chinese standard). Tensile strength and elongation at break were measured according to GB/T 1040 (Chinese standard). Bending strength was measured according to GB/T 9341 (Chinese standard). All tests were carried out at room temperature (23°C). The resulting value of each sample was the average of five parallel experiments.

The samples of PA10N were pyrolyzed with a set-point of 700°C per 5 s using a Chemical Data Systems Pyroprobe 2000. Pyrolyses were carried out in helium using a coil probe. The sample weights used ranged from 0.1 to 1 mg, and no changes in pyrolysis product distribution were observed. Analysis was performed using an Agilent GC/MS(6890A/5973) system with a DB-FFAP (nitroterephthalic acid modified polyethylene glycol) capillary columns from J&W Company (60 m×250 μm×0.25 μm). The oven temperature program was as follows: 40°C, initial time 5 min, heating rate 3°C·min^{-1}, then temperature 200°C holding 10 min, final temperature 230°C for 20 min. Helium was used as the carrier gas. Mass spectra was acquired by a Nist98 Mass Spectra Library data system operating under HP Chemistry Station G1034. The mass spectrometer was scanned repetitively from *m*/*z* 500 to *m*/*z* 20 at a scan rate of 0.7 s/decade; the ionizing conditions were 70 eV.

3. Results and discussion

3.1. Synthesis of PA10N

PA10N was prepared from the reaction of 2,6-naphthalene dicarboxylic acid and 1,10-decanediamine through a three-step procedure: salt formation, prepolymerization and solid-state polymerization. In order to assure an accurate equivalent ratio of 1,10-decanediamine to 2,6-naphthalene dicarboxylic acid, PA10N salt was prepared firstly. Then an slight excess 1,10-decanediamine was added into the salt solution to compensate reaction system for the loss during the prepolymerization reaction. It is noticeable that the solvent for the salt formation reaction is water, which is cheaper and environmental friendly compared with ethanol, usually used in preparing other common polyamides [25]. In order to obtain high vapor pressure, the distilled water was added to reduce volatilization of diamine during the prepolymerization. The prepolymer was ground into small particles, which are convenient for removing water. In order to avoid side reaction and to improve the molecular weight of the polyamide, the high vacuum was maintained during the solid-state polymerization reaction. The molecular weight of the PA10N was characterized by intrinsic viscosity and inherent viscosity. The intrinsic viscosity and inherent viscosity of PA10N are 1.85 dl·g^{-1} and about 1.78 dl·g^{-1}, respectively.

FT-IR spectrum of the PA10N is shown in Figure 2. All the characteristic peaks of amide groups and methylene segments of polyamide are listed as follows: 1632 cm^{-1} (amide I, C=O stretching vibration), 1534 cm^{-1} (amide II, C–N stretching and CO–N–H bending vibration), 2922 cm^{-1} (N–H in-plane bending vibration and CH_2 vibration), 3296 cm^{-1} (hydrogen-bonded and N–H stretching vibration), 3076 cm^{-1} (N–H in-plane bending),

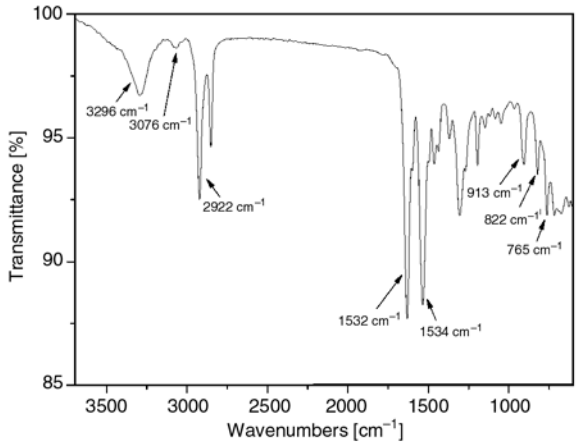

Figure 2. FT-IR spectra of PA10N

912 cm^{-1} (amide IV, C–CO stretching vibration), 822 cm^{-1} (CH_2 wagging), 765 cm^{-1} (C–H of naphthalene ring vibration).

Figure 3 presents the ^{1}H-NMR spectrum of PA10N in deuterated trifluoroacetic acid. The chemical shifts at 8.50 ppm (2H), 7.96 ppm (2H) and 8.19 ppm (2H) are attributed to the naphthalene ring protons (*a*, *b* and *c*). The chemical shift at 3.83 ppm (4H) originates from the protons at the position *d* while that at 1.93 ppm (4H) comes from the protons at the position *e*. The peak at 1.49 ppm (12H) belongs to the other protons of the aliphatic chains (*f*). The peak at 11.6 ppm was assigned to trifluoroacetic acid.

The elemental analysis data of PA10N are listed in Table 1. The calculated components are presented for comparison. The resulting value of elemental analysis was the average of five parallel experiments. The hydrogen content of PA10N is higher than the theoretical value owing to the absorption of water. The other measurement results are in agreement with the theoretical values.

The water-absorbing of PA10N was measured according to GB/T 1034 (Chinese standard), and the result is 0.14. The low water absorption, close to PA9T (0.17) [26], is conducive to maintain dimensional and mechanical stability of products.

The solubilities (sample 100 mg, solvent 10 ml) of PA10N were tested in different organic solvents. PA10N can easily dissolve in acidic solvents such as concentrated sulfuric acid and trifluoroacetic acid (TFA) at room temperature, while it is insoluble in dimethylsulphoxide (DMSO), N,N′-dimethylformamide (DMF), 1-methyl-2-pyrrolidenone (NMP), dimethylacetamide (DMAc), *m*-cresol, tetrahydrofuran (THF), pyridine, tetrachloroethane, chlorobenzene, methanol, toluene, chloroform, phenol and formic acid. The results show that PA10N exhibits good chemical solvent resistance.

3.2. Thermal properties of PA10N

Figure 4 depicts the DSC curves of PA10N. Curve A is the second heating DSC curve, while B is a cooling DSC curve. The heating rate is 10°C·min^{-1}, and the test temperature is 50 to 330°C. PA10N exhibits double-melting endotherms, which is a common phenomenon observed in semicrystalline polymers [27–29]. The melting temperature (T_m) of PA10N is 320°C based on curve A, and the crystallization

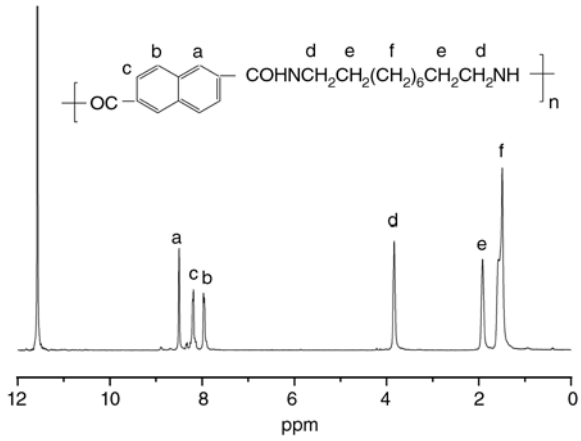

Figure 3. ^{1}H-NMR spectra of PA10N

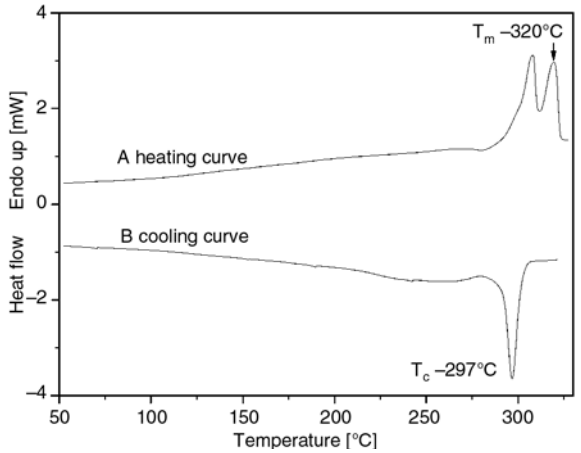

Figure 4. DSC curves of PA10N

Table 1. Elemental analysis data of PA10N

Sample	Carbon [%]		Hydrogen [%]		Nitrogen [%]		Oxygen [%]	
	calculated	measured	calculated	measured	calculated	measured	calculated	measured
PA10N	75.0	74.9	7.95	8.01	7.95	7.91	9.10	9.18

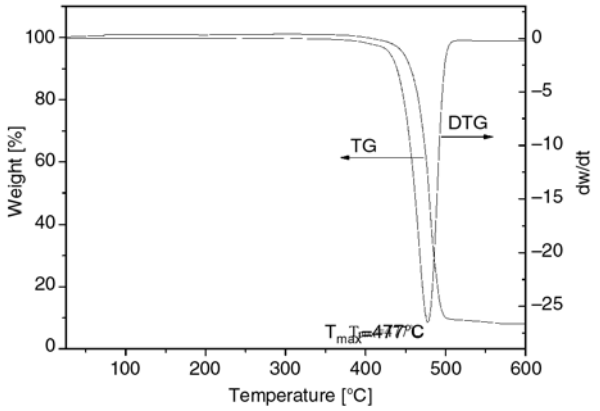

Figure 5. TGA curves of PA10N

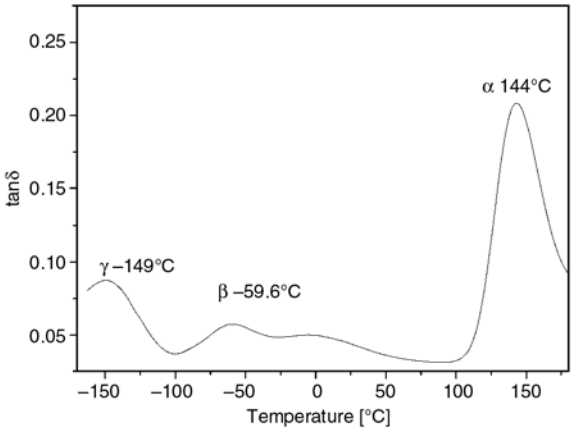

Figure 6. DMA curve versus temperature of PA10N (1 Hz)

temperature (T_c) of PA10N is 297°C based on curve B.

TGA curves of PA10N are shown in Figure 5. The curve A of PA10N shows a one-stage weight loss process in nitrogen. The decomposition temperature (T_d) of PA10N is approximately 495°C, and the termination temperature of thermal degradation is about 500°C. The maximum degradation temperature (T_{max}) of PA11N is 477°C.

The T_m of PA10N is far below T_d of PA10N. Therefore, the melt processing ability of PA10N is excellent. In addition, the T_d of PA10N is higher than that of aliphatic polyamides [30, 31]. The results show that the thermal stability of PA10N has been improved by inserting naphthalene linkage into the polymeric backbone.

DMA was also used to characterize the thermal property of PA10N (Figure 6). Three obvious transition peaks can be observed, and are defined as α, β and γ relaxation, respectively. The glass transition temperature (T_g) of the PA10N is 144°C according to α relaxation. T_g of aliphatic polyamides such as poly(ε-caprolactam) (nylon6) (T_g = 60°C) and poly(hexamethylene adipamide) (nylon66) (T_g = 50°C) are all below 90°C. The results show that T_g of PA10N is higher than those of aliphatic polyamides. As expected, the heat-resistance of PA10N was improved by the introduction of naphthalene-ring. The β relaxation reflects the mobility of carbonyl group of amorphous region, and the γ relaxation reflects the co-movement of amido and methane groups. The thermal data of PA10N in this work are listed in Table 2.

3.3. Mechanical properties of PA10N

All dry and standard samples of PA10N for mechanical tests were prepared by injection molding in an injection-molding machine. Based on Table 3, it can be observed that the tensile strength of PA10N is almost as same as that of PA9T at room temperature [32].

3.4. Flash Py-GC/MS analysis

A typical pyrogram of PA10N (total ion chromatogram of the pyrolysates) obtained by flash pyrolysis at 700°C is shown in Figure 7. The pyrolysates were identified by mass spectra and confirmed by comparing their retention times [33–37]. The results of identification, the molecular weight and relative intensity of pyrolysis products

Table 2. The intrinsic viscosity, thermal data and water-absorbing capacity of PA10N

Sample	η [dl·g^{-1}]	T_m [°C]	T_c [°C]	T_d [°C]	T_g [°C]	Water-absorbing capacity [%]
PA10N	1.85	320	297	495	144	0.14

Table 3. The mechanical property of PA10N compared with PA9T

Samples	Tensile strength [MPa]	Tensile modulus [GPa]	Breaking elongation [%]	Bending strength [MPa]	Bending modulus [GPa]	Izod impact strength [kJ·m^{-2}]
PA10N	94	1.7	40	92	1.9	5.2
PA9T	92	–	20	120	2.6	4.9

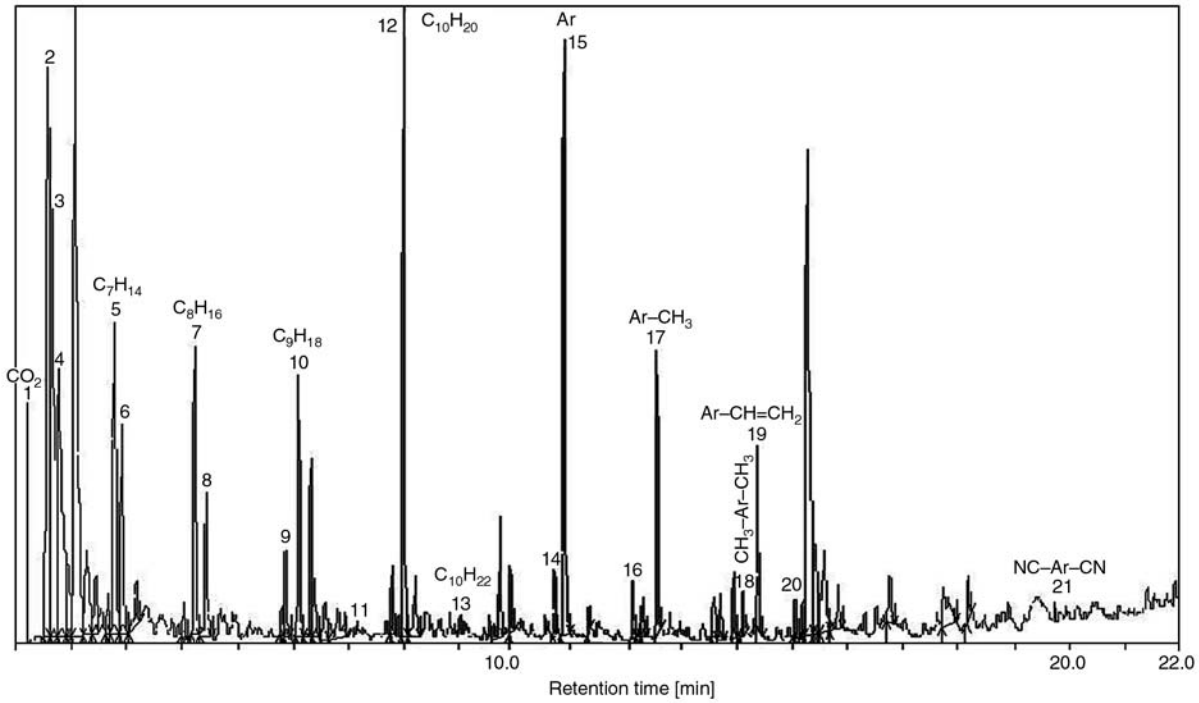

Figure 7. Py-GC/MS chromatogram of PA10N at 700°C

Table 4. Analysis results of PA10N by Py-GC/MS

No.	Tentative compounds	Molecular weight	Retention time [min]	Formula	Relative intensity [%]
1	Carbon dioxide	44	1.57	CO_2	16.39
2	Pentanenitrile	83	1.65	C_5H_9N	3.47
3	1-Pentene	70	1.77	C_5H_{10}	2.95
4	1-Hexene	84	2.06	C_6H_{12}	6.27
5	1-Heptene	98	2.77	C_7H_{14}	2.66
6	Heptane	100	2.89	C_7H_{16}	2.81
7	1-Octene	112	4.21	C_8H_{16}	2.15
8	Octane	114	4.42	C_8H_{18}	2.14
9	1,8-Nonadiene	124	5.86	C_9H_{16}	2.57
10	1-Nonene	126	6.09	C_9H_{18}	3.07
11	Nonane	128	7.42	C_9H_{20}	3.29
12	1-Decene	140	7.98	$C_{10}H_{20}$	2.20
13	Decane	142	9.29	$C_{10}H_{22}$	2.75
14	Octanenitrile	125	10.71	$C_8H_{15}N$	2.49
15	Naphthalene	128	10.88	$C_{10}H_8$	19.62
16	Decanenitrile	153	12.26	$C_{10}H_{19}N$	2.56
17	1-Methylnaphthalene	142	12.57	$C_{11}H_{10}$	4.57
18	2,6-Dimethylnaphthalene	156	14.10	$C_{12}H_{12}$	2.92
19	2-Vinylnaphthalene	154	14.38	$C_{12}H_{10}$	2.57
20	1-Naphthalenecarbonitrile	153	15.28	$C_{11}H_7N$	9.57
21	2,6-Naphthalene dicarbonitrile	178	19.77	$C_{12}H_6N_2$	2.11

are reported in Table 4. The relative intensity is a ratio of integral shadow area among them. The weight of each sample used in the analysis is 0.1, 0.2, 0.5 and 1 mg. Four parallel experiments were carried out for each sample with different sample weight, and no changes in relative intensity of pyrolysis product were observed. The resulting value was the average of four parallel experiments.

3.5. The inferred thermal decomposition processes

The bond strength of C–N is 305 kJ·mol^{-1}, which is less than the value of 346 kJ·mol^{-1} for a C–C bond [38], so many evidences suggested that the primary polyamide chain scission occurs either at the peptide C–N or at adjacent bonds [39]. Homolytic scission, hydrolysis, intramolecular C–H transfer and

cis-elimination (a particular case of C–H transfer) are all suggested as possible primary chains-scission mechanisms [39]. Naphthalene rings are stabilized in the process of pyrolysis of PA10N, the cleavage of the C–N amide bond and the homolytic scission of $C_{naphthalene}$–C_{amido} bond were the primary pyrolysis pathways. According to the pyrolysis products, the possible pyrolysis pathways are illustrated in Figure 8–11 (Marked as route A, B, C and D respectively). The four possible routes happen randomly at the same time.

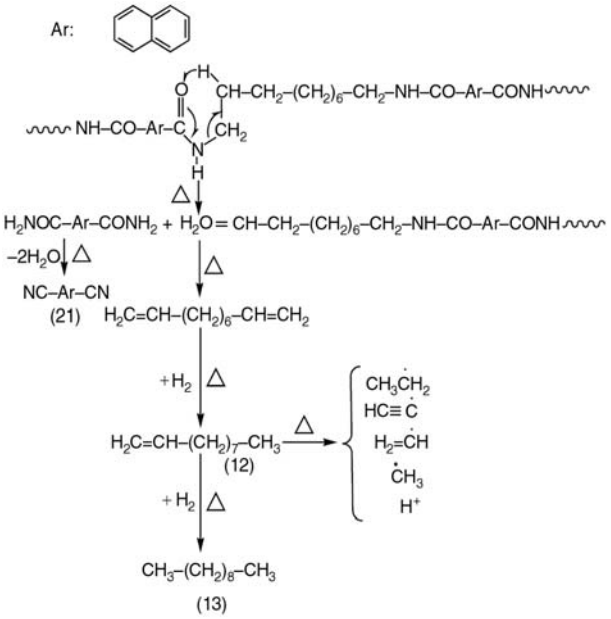

Figure 8. Thermal decomposition mechanism A of PA10N

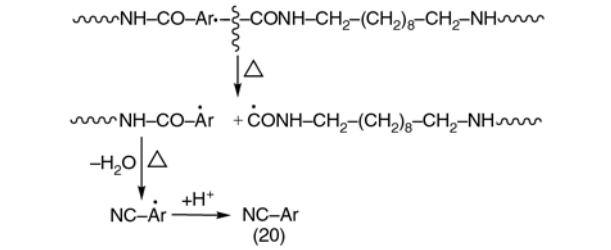

Figure 9. Thermal decomposition mechanism B of PA10N

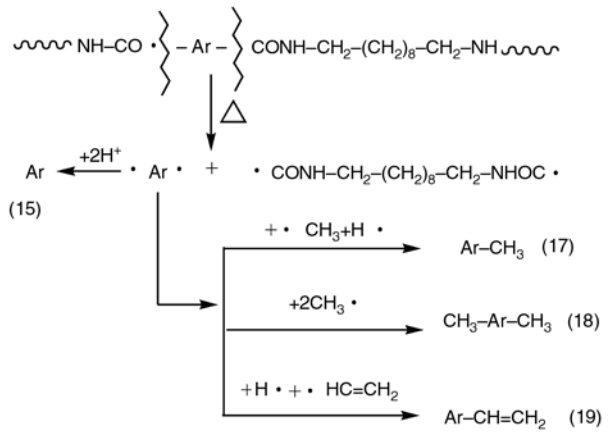

Figure 10. Thermal decomposition mechanism C of PA10N

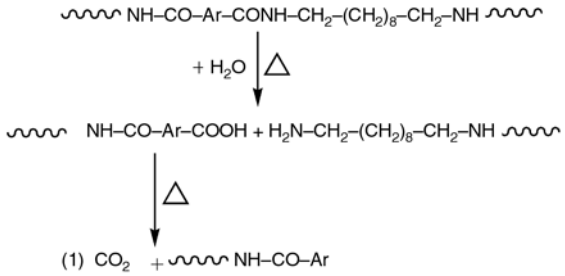

Figure 11. Thermal decomposition mechanism D of PA10N

Route A indicated that PA10N was decomposed via a β-CH hydrogen transfer process with formation of amide and olefin end-groups [40]. The products containing amide end-groups could further undergo thermal decompositions and produce the compounds with nitrile end-group, such as 2,6-naphthalene dicarbonitrile.

Route B showed homolytic cleavage occurred at one side of the $C_{naphthalene}$–C_{amido} bonds which form naphthalene amide and alkylamide radicals. Then, naphthalene amide radical reacted with hydrogen radical, alkyl radical and eliminating water. Finally, 1-naphthalenecarbonitrile was obtained.

Route C presented the bonds cleavage occurred at the two sides of $C_{naphthalene}$–C_{amido} bonds forming the compounds containing naphthalene and alkylamide radicals. Naphthalene radical reacted with hydrogen radical, alkyl radical, and ethene radical, and then formatted naphthalene compounds.

Route D presented the amide bond leaded to hydrolysis in the presence of water which formed the $–NH_2$ and –COOH end-groups [41], –COOH end-groups were further degraded to form CO_2.

Alkenes and diolefines are easy to take part in homolytic radical scission of the C–C bonds at high temperature to form smaller fragments. These fragments might react with benzene and benzonitrile free radical, so the alkenes and diolefines were not detected in the pyrolysis products.

4. Conclusions

PA10N was prepared from the reaction of 2,6-naphthalene dicarboxylic acid and 1,10-decanediamine. The characterization of FT-IR, ^{1}H-NMR

spectroscopy and elemental analysis confirmed that the obtained product has the expected chemical structure and composition. T_m, T_g and T_d of PA10N are 320, 144 and 495°C, respectively. The intrinsic viscosity and inherent viscosity of PA10N are 1.85 dl·g^{-1} and about 1.78 dl·g^{-1}, respectively. The results show that PA10N has better thermal stability than aliphatic polyamides. Py-GC/MS was used to study the pyrolysis products and thermal decomposition mechanisms of PA10N. The pyrolysis products of PA10N were mainly composed of twenty-one kinds of compounds, and the major pyrolysis process included β-CH hydrogen transfer process, main chain random scission and hydrolytic decomposition. Compared with PA9T, the low cost and good performance of PA10N demonstrate it could be a promising, heat-resisting and well processable engineering plastic and it can be a candidate nylon for the industrial production.

References

[1] Cassidy P. E.: Thermally stable polymers. Marcel Dekker, New York (1980).

[2] Persyn O., Miri V., Lefebvre J-M., Ferreiro V., Brink T., Stroeks A.: Mechanical behavior of films of miscible polyamide 6/polyamide 6I-6T blends. Journal of Polymer Science Part B: Polymer Physics, **44**, 1690–1701 (2006).
DOI: 10.1002/polb.20825

[3] Endo M., Morishima Y., Yano S., Tadano K., Murata Y., Tsunashima K.: Miscibility in binary blends of aromatic and alicyclic polyamides. Journal of Applied Polymer Science, **101**, 3971–3978 (2006).
DOI: 10.1002/app.22912

[4] Ferreiro J. J., de la Campa J. G., Lozano A. E., de Abajo J.: Polyisophthalamides with heteroaromatic pendent rings: Synthesis, physical properties, and water uptake. Journal of Polymer Science Part A: Polymer Chemistry, **43**, 5300–5311 (2005).
DOI: 10.1002/pola.21000

[5] Yang H. H.: Aromatic high-strength fibers. Wiley, New York (1989).

[6] Rao Y., Waddon A. J., Farris R. J.: Structure-property relation in poly(*p*-phenylene terephthalamide) (PPTA) fibers. Polymer, **42**, 5937–5946 (2001).
DOI: 10.1016/S0032-3861(00)00905-8

[7] Spiliopoulos I. K., Mikroyannidis J. A., Tsivgoulis G. M.: Rigid-rod polyamides and polyimides derived from 4,3″-diamino-2′,6′-diphenyl- or di(4-biphenylyl)-p-terphenyl and 4-amino-4″-carboxy-2′,6′-diphenyl-*p*-terphenyl. Macromolecules, **31**, 522–529 (1998).
DOI: 10.1021/ma9709664

[8] Liaw D-J., Liaw B-Y., Tseng J-M.: Synthesis and characterization of novel poly(amide-imide)s containing hexafluoroisopropylidene linkage. Journal of Polymer Science Part A: Polymer Chemistry, **37**, 2629–2635 (1999).
DOI: 10.1002/(SICI)1099-0518(19990715)37:14<2629::AID-POLA37>3.0.CO;2-3

[9] Liaw D-J., Hsu P-N., Chen W-H., Lin S-L.: High glass transitions of new polyamides, polyimides, and poly(amide-imide)s containing a triphenylamine group: Synthesis and characterization. Macromolecules, **35**, 4669–4676 (2002).
DOI: 10.1021/ma001523u

[10] Liaw D-J., Chang F-C., Leung M-K., Chou M-Y., Muellen K.: High thermal stability and rigid rod of novel organosoluble polyimides and polyamides based on bulky and noncoplanar naphthalene-biphenyldiamine. Macromolecules, **38**, 4024–4029 (2005).
DOI: 10.1021/ma048559x

[11] Uddin A. J., Ohkoshi Y., Gotoh Y., Nagura M., Endo R., Hara T.: Melt spinning and laser-heated drawing of a new semiaromatic polyamide, PA9-T fiber. Journal of Polymer Science Part B: Polymer Physics, **42**, 433–444 (2004).
DOI: 10.1002/polb.10710

[12] Wang W., Wang X., Li R., Liu B., Wang E., Zhang Y.: Environment-friendly synthesis of long chain semiaromatic polyamides with high heat resistance. Journal of Applied Polymer Science, **6**, 2036–2042 (2009).
DOI: 10.1002/app.30774

[13] Wang W., Zhang Y.: Environment-friendly synthesis of long chain semiaromatic polyamides. Express Polymer Letters, **3**, 470–476 (2009).
DOI: 10.3144/expresspolymlett.2009.58

[14] Pei X., Zhao Q., Liu M., Wang Y., Wang W., Cao S.: Synthesis and characterization of two new semiaromatic polyamides. China Plastics Industrial, **33**, 7–9 (2005).

[15] Liu M., Zhao Q., Wang Y., Zhang C., Li X.: Synthesis, property and application of petroleum fermentation nylon 1212. Engineering Plastics Application, **30**, 37–39 (2002).

[16] Jiang T., Liu M., Fu P., Wang Y., Fang Y., Zhao Q.: Melting behavior, isothermal and nonisothermal crystallization kinetics of nylon 1111. Polymer Engineering and Science, **49**, 1366–1374 (2009).
DOI: 10.1002/pen.21269

[17] Ng H. C.: Blends of poly(1,3-propylene 2,6-naphthalate). US Patent 6531548, USA (2003).

[18] Kuoo Y-H., Wang C-L.: Polynaphthimidazoles prepared from naphthalene dicarboxylic acid and their properties. Polymer International, **40**, 93–98 (1996).
DOI: 10.1002/(SICI)1097-0126(199606)40:2<93::AID-PI520>3.0.CO;2-B

[19] Jian L., Sherrington D. C.: Recent developments in the synthesis, thermostability and liquid crystal properties of aromatic polyamides. Advances in Polymer Science, **111**, 177–216 (1994). DOI: 10.1007/BFb0024129

[20] Ballistreri A., Garozzo D., Giuffrida M., Maravigna P.: Thermal decomposition processes in aliphatic-aromatic polyamides investigated by mass spectrometry. Macromolecules, **19**, 2693–2699 (1986). DOI: 10.1021/ma00165a005

[21] Gao L., Liu M., Zhao Q., Wang Y., Yang X., Cao S.: Thermal degradation process and mechanism of poly(dodecamethyleneterephthalamide) (in Chinese). Polymer Materials Science and Engineering, **18**, 129–132 (2002).

[22] Liebman S. A., Levy E. J.: Pyrolysis and GC in polymer analysis. Marcel Dekker, New York (1985).

[23] van Lieshout M. H. P., Janssen H-G., Cramers C. A., Hetem M. J. J., Schalk H. J. P.: Characterization of polymers by multi-step thermal desorption/programmed pyrolysis gas chromatography using a high temperature PTV injector. Journal of High Resolution Chromatography, **19**, 193–199 (1996). DOI: 10.1002/jhrc.1240190404

[24] Wang F. C.: Composition and structure analysis of styrene-maleic anhydride copolymer by pyrolysis-gas chromatography. Journal of Chromatography A, **765**, 279–285 (1997). DOI: 10.1016/S0021-9673(96)00968-5

[25] Cui X. W., Li W. H., Yan D. Y.: Investigation on odd-odd nylons based on undecanedioic acid: 1. Synthesis and characterization. Polymer International, **53**, 1729–1734 (2004). DOI: 10.1002/pi.1546

[26] Zou S.: Heat resistant polyamide PA9T. Modern Plastics, **12**, 62–64 (2000).

[27] Li Y., Zhu X., Tian G., Yan D., Zhou E.: Multiple melting endotherms in melt-crystallized nylon 10,12. Polymer International, **50**, 677–678 (2001). DOI: 10.1002/pi.682

[28] Ramesh C., Keller A., Eltink S. J.: Studies on the crystallization and melting of nylon 66: 3. Melting behaviour of negative spherulites by calorimetry. Polymer, **35**, 5300–5302 (1994). DOI: 10.1016/0032-3861(94)90483-9

[29] Hybart F. J., Platt J. D.: The melting of 66 nylon: Observations by differential thermal analysis. Journal of Applied Polymer Science, **11**, 1449–1453 (1967). DOI: 10.1002/app.1967.070110808

[30] Wang Y., Liu M., Zhao Q.: Studies on the process and kinetics of thermal degradation in nylon 109 (in Chinese). Polymeric Materials Science and Engineering, **15**, 78–80 (1999).

[31] Zhao Q., Wang Y., Liu M., Du B., Li H., Li X..: Study on process and kinetics of thermal degradation in nylon 69 (in Chinese). Polymeric Materials Science and Engineering, **11**, 52–56 (1995).

[32] Ma J. M., Song S. W., Guo J.: New heat resistance polyamide. Modern Plastics, **15**, 41–44 (2003).

[33] Schulten H-R., Plage B.: Thermal degradation of aliphatic polyamides studied by field ionization and field desorption mass spectrometry. Journal of Polymer Science Part A: Polymer Chemistry, **26**, 2381–2394 (1988). DOI: 10.1002/pola.1988.080260911

[34] Ballistreri A., Garozzo D., Giuffrida M., Impallomeni G., Montaudo G.: Primary thermal decomposition processes in aliphatic polyamides. Polymer Degradation and Stability, **23**, 25–41 (1988). DOI: 10.1016/0141-3910(89)90066-9

[35] Czégény Z., Blazsó M.: Thermal decomposition of polyamides in the presence of poly(vinyl chloride). Journal of Analytical and Applied Pyrolysis, **58**, 95–104 (2001). DOI: 10.1016/S0165-2370(00)00152-2

[36] Herrera M., Matuschek G., Kettrup A.: Main products and kinetics of the thermal degradation of polyamides. Chemosphere, **42**, 601–607 (2001). DOI: 10.1016/S0045-6535(00)00233-2

[37] Linda J. B., Michael T. K., Barry D. D., Stephen M. A.: Thermal degradation of aliphatic-aromatic polyamides: Kinetics of *N*,*N*′-dihexylisophthalamide neat and in presence of copper lodide. Journal of Applied Polymer Science, **56**, 803–815 (1995). DOI: 10.1002/app.1995.070560705

[38] Cottrell T. L.: The strengths of chemical bonds. Butterworths, London (1958).

[39] Levchik S. V., Weil E. D., Lewin M.: Thermal decomposition of aliphatic nylons. Polymer International, **48**, 532–557 (1999). DOI: 10.1002/(SICI)1097-0126(199907)48:7<532::AID-PI214>3.0.CO;2-R

[40] Ballistreri A., Garozzo D., Maravigna P., Montaudo G., Giuffrida M.: Thermal decomposition processes in aromatic-aliphatic polyamides investigated by mass spectrometry. Journal of Polymer Science Part A: Polymer Chemistry, **25**, 1049–1063 (1987). DOI: 10.1002/pola.1987.080250411

[41] Khanna Y. P., Pearce E. M., Smith J. S., Burkitt D. T., Njuguna H., Hindenlang D. M., Forman B. D.: Aromatic polyamides. II. Thermal degradation of some aromatic polyamides and their model diamides. Journal of Polymer Science Part A: Polymer Chemistry, **19**, 2817–2834 (1981). DOI: 10.1002/pol.1981.170191115

eXPRESS Polymer Letters Vol.4, No.6 (2010) 355–363
Available online at www.expresspolymlett.com
DOI: 10.3144/expresspolymlett.2010.45

Reinforcement of poly(dimethylsiloxane) by sol-gel *in situ* generated silica and titania particles

*L. Bokobza**, *A. L. Diop*

Laboratoire PPMD, E.S.P.C.I., 10 rue Vauquelin, 75231 Paris Cedex, France

Received 1 March 2010; accepted in revised form 10 April 2010

Abstract. The usual sol-gel process was applied to precipitate silica or titania particles in a preformed poly(dimethylsiloxane) (PDMS) network under the presence of dibutyltin diacetate used as a catalyst. The resulting structures of the reinforcing fillers were studied by transmission electron microscopy and small-angle neutron scattering. Stress-strain measurements in elongation and equilibrium swelling experiments revealed distinct behaviors mainly attributed to the nature and the size of the generated particles and to the formation, in the case of titania, of a filler network even at low filler loadings.

Keywords: *nanocomposites, reinforcement, poly(dimethylsiloxane), silica, titania*

1. Introduction

In the unfilled state, poly(dimethylsiloxane) (PDMS) elastomers have generally poor mechanical properties which can be greatly improved by incorporation of mineral particles. Uniformity of the dispersion and good interfacial adhesion between the matrix and the filler have a strong influence on the performance of the elastomeric material. PDMS is traditionally reinforced with silica and the interaction between the two phases is ensured via hydrogen bonds between the silanols on the silica surface and the oxygen atoms of the polymer chains. Although fillers can be incorporated by the usual technique of blending them into the polymer before cross-linking, a number of alternative novel techniques for incorporation of fillers have been developed. They include a sol-gel process to precipitate particles into the elastomeric matrix. This process produces a finely divided morphology of filler resulting in optically transparent materials. The formation of the inorganic component is carried out under mild synthetic conditions and involves various alkoxides ($[M(OR)_x]$, where M = Si, Ti, Zr, Al… and R is an aliphatic group) that are hydrolyzed and condensed under either acidic or basic catalysis, in order to form M–O–M bridging units.

A series of previous investigations [1–7] has shown the feasibility of precipitating silica, titania or mixed silica-titania phases into PDMS networks. All these studies report significant property improvements in the hybrid composites with regard to the unfilled networks.

Although there are a number of ways to carry out the sol-gel technique to prepare hybrid organic composites, the method chosen in this paper is to synthesize the mineral phase in already crosslinked networks by using a synthetic protocol different from those previously reported in the literature. Additionally, the sol-gel approach developed for the *in situ* generation of silica into an elastomer is extended to the generation of titania by hydrolyzing a titanate instead of a silicate. PDMS networks filled with *in situ* generated reinforced particles are

*Corresponding author, e-mail: Liliane.Bokobza@espci.fr

prepared and characterized through their morphological, mechanical and swelling properties in order to compare titania-filled materials with those filled with silica.

2. Experimental

2.1. Materials

PDMS having hydroxyl chain ends and a number-average molecular weight of 18 000 g·mol^{-1} was obtained from Gelest (Morrisville, PA, USA). The catalysts: stannous-2-ethyl-hexanoate for the cross-linking reaction and dibutyltin diacetate for the sol-gel process were respectively supplied by Sigma and Aldrich. The alkoxides, tetraethoxysilane (TEOS) and titanium n-butoxide (TBO) were provided by Gelest (Morrisville, PA, USA) and Acros Organics (Geel, Belgium), respectively. All of these materials were used as received.

2.2. Synthetic aspects

In this study, unfilled PDMS networks are first prepared and are then swollen in the adequate alkoxide.

2.2.1. Preparation of the unfilled PDMS networks

The unfilled networks are prepared from hydroxy-terminated PDMS by end-linking reactions using tetraethoxysilane (TEOS) as the cross-linking agent. In this method of network synthesis, a stoichiometric balance between ethoxy groups of the tetrafunctional alkoxysilane cross-linker and the hydroxyl chain ends of the hydroxyl-terminated PDMS precursor chains, should be required to get model networks characterized by constant junction functionality and known molecular weight between cross-links (close to the number-average molecular weight of precursor chains) [1, 2, 8–12]. Actually, networks prepared at stoichiometric conditions have an elastic modulus lower than that deduced from the molecular weight between cross-links and great soluble fraction (around 10%). This may be due to the volatility of TEOS thus reducing the amount of cross-linker required for the alkoxy-functional condensation reaction. Much greater ratios of cross-linker functions to chain ends than that required by stoichiometry have already been used in the literature [13, 14] but a systematic study of the effect of excess of TEOS on the mechanical properties of networks synthesized from OH-terminated chains shows that a 50% excess (and not higher values as already reported) are enough to ensure correct modulus and reasonable soluble fraction. So, hydroxyl-terminated PDMS (M_w = 18 000) is mixed for half an hour with TEOS, in excess of 50%. A small amount of stannous-2-ethyl-hexanoate used as catalyst, is then added to the mixture under mechanical stirring just for 5 minutes to avoid cross-linking reaction during mixing. The reacting mixture is slowly cast into a Teflon mold and left for a few minutes at room temperature then at 80°C for one day for complete curing. The films are extracted with toluene for 72 hours to remove any unreacted materials. The sol fractions are between 4 and 5%.

2.2.2. Preparation of the *in situ* filled PDMS networks

The next step for composite preparation involves swelling the unfilled extracted polymer network in a silicon alkoxide for silica or in a titanium alkoxide for titania generation. The inorganic precursor is TEOS for silica and titanium n-butoxide (TBO) for titania. In fact, titanium alkoxides have much higher reactivity than silicon analogues and the resistance to hydrolysis can be obtained by increasing the length of the alkyl chain [15]. Therefore, as in other studies [16, 17] titanium n-butoxide (TBO) has been chosen as the precursor of TiO_2 in the sol-gel process.

The two overall reactions can be summarized as shown in Equations (1) and (2):

$$Si(OC_2H_5)_4 + 2H_2O \rightarrow SiO_2 + 4C_2H_5OH \quad (1)$$

$$Ti(OC_4H_9)_4 + 2H_2O \rightarrow TiO_2 + 4C_4H_9OH \quad (2)$$

For *in situ* precipitation of filler particles, the PDMS films are swollen in the alkoxide (TEOS or TBO) in the presence of a pH-neutral catalyst: dibutyltin diacetate (DBTDA) used at 3 weight percent. The swelling time determines the degree of alkoxide absorption and thus the filler loading. Both the swollen film and a beaker containing water are placed for 48 hours into a desiccator maintained at a constant temperature (30°C) thus exposing the swollen film to saturated water vapor.

The film is then vacuum-dried at 80°C for several days to constant weight in order to remove any alcohol generated from the reaction and also the remaining alkoxide which has not been hydrolyzed. The amount of filler incorporated into the network was calculated from the weights of the films before and after the generation of the filler. As a result of lower viscosity, the rate of diffusion of TEOS is much faster than that of TBO in PDMS films, leading, at a given swelling time, to a much higher swelling ratio. As a typical example, a degree of swelling of 100% of the initial PDMS film requires a swelling time of about 10 min in TEOS and 1000 min in TBO.

Infrared spectroscopy has been used to follow the sol-gel process. In particular, we note a progressive reduction in intensity of absorption bands associated with the alkoxides during the hydrolysis process and a total disappearance of these bands after total reaction. On the other hand, silica formation within the preformed PDMS network can be followed in the infrared spectra of the silica-filled PDMS networks where it is seen that the bands associated with silica increase with the silica content in the composite

2.3. Characterization techniques

For the transmission electron microscopy (TEM), ultrathin sections were cryomicrotomed using a diamond knife at –140°C. The nominal section thickness was 100 nm. The samples were observed on a JEOL JEM 1230 Transmission Electron Microscope, operating at 80 kV.

Small-angle neutron scattering (SANS) were collected using the equipment PACE provided by the Laboratoire Léon Brillouin at Saclay (France). A wavelength between 4 and 20 Å can be used with a wavelength spread of $\Delta\lambda/\lambda = 0.10$ and a sample-to-detector distance between 1 to 5 m. The scattering vector q, ranges between $3\cdot10^{-3}$ and 0.3 $Å^{-1}$.

Strips of unfilled and filled elastomers were used in the uniaxial elongation experiments carried out to obtain the stress-strain curves at equilibrium [18]. The nominal stress σ, was calculated from Equation (3):

$$\sigma = \frac{f}{A} \tag{3}$$

where f is the elastic force and A is the undeformed cross-sectional area and the reduced stress, σ^* was calculated from Equation (4):

$$\sigma^* = \frac{\sigma}{\alpha - \alpha^{-2}} \tag{4}$$

where α is the extension ratio (ratio of the final length of the sample in the direction of stretch to the initial length before deformation).

To determine the equilibrium swelling of the vulcanizate, a sample of 20 mm×10 mm×1 mm was put into toluene. After 72 h at room temperature, the sample was taken out of the liquid, the toluene removed from the surface and the weight determined. The swelling ratio, Q, was also determined from the lengths of the sample in the unswollen and swollen states.

3. Results and discussion

3.1. Filler characterization

Microscopy and scattering techniques are very useful for the characterization of generated filler structures. For filled materials formed by swelling an elastomeric network in alkoxides and subsequently polymerizing by the sol-gel technique, the generated particles are usually more finely dispersed than those prepared by a physical blending of preformed filler particles into polymers.

Figure 1 show TEM images of composites filled with SiO_2 (Figure 1a and 1b) or TiO_2 (Figure 1c –1e) particles *in situ* generated in already-formed PDMS networks. But although *in situ* precipitated filler particles seem to be uniformly dispersed in both cases, different morphologies are revealed. The diameter of the generated silica particles is seen to be much smaller than that of titanium dioxide particles. The composite containing 10 phr of SiO_2 (Figure 1a) shows an excellent dispersion of the mineral phase in the polymer with small silica domains around ~5 nm in diameter and rather diffuse interfaces. For the higher content, a fine morphology of the silicate structure is still obtained suggesting an interpenetrated polymer-silica structure and the sample may be regarded as microscopically phase separated but macroscopically uniform. TEM images of titania-filled PDMS composites indicate an obvious two-phase structure with particles approximately spherical in shape and

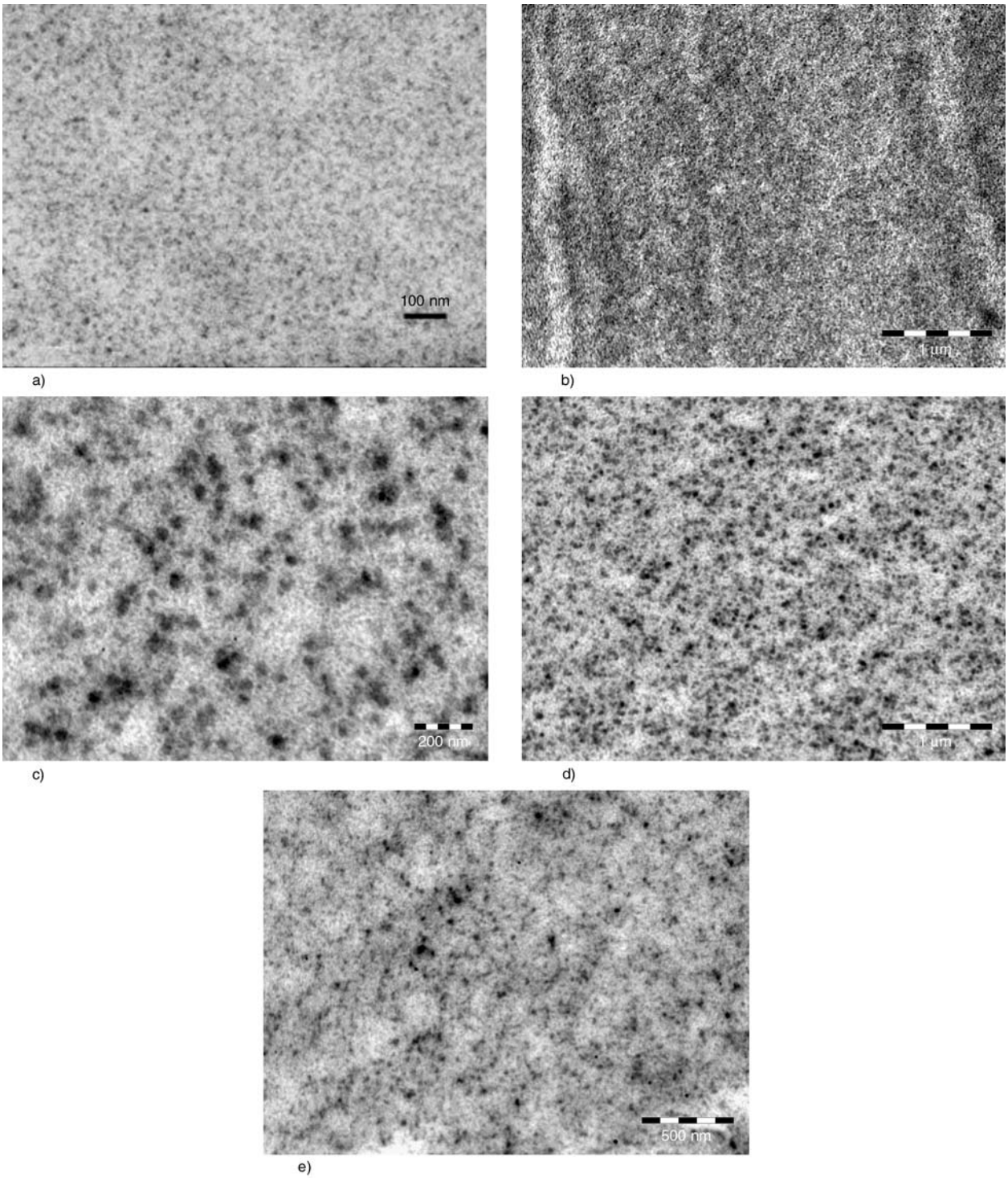

Figure 1. TEM images of PDMS composites filled with *in situ* generated particles: a) 10 phr of SiO_2, b) 28 phr of SiO_2, c) 12 phr of TiO_2, d) 12 phr of TiO_2, e) 25 phr of TiO_2

diameters between 20 and 40 nm in size. The interface between the polymer and the particles is better defined than in the case of silica-filled systems and even at the lowest filler content (Figure 1c and 1d), the titania particles are almost connected in a branched network structure.

With the aid of concepts in fractal geometry, some aspects of the filler structure can be derived from small-angle scattering techniques. The scattering profiles of fractal objects are a power law of the type described by Equation (5):

$$I(q) = q^{-P} \tag{5}$$

where I is the scattered intensity at wave vector q and the exponent P allows to distinguish between mass and surface fractals [9, 10, 19]. A slope of –4 in log-log axes, indicates that the system follows the Porod's law ($P = D_s - 6$), D_s being the surface fractal dimension. The scatterers are, in this case, dense objects characterized by smooth surface fractal dimension ($D_s = 2$). A value of P between –3 and –4, is indicative of compact objects with fractally rough surfaces. If $P < 3$, scatterers are mass fractal objects with a fractal dimension $D_f = P$. A slope of –2 suggests the presence of a polymeric structure.

As seen in Figure 2, the two types of composites yield distinctive small-angle scattering profiles. The slope of 3.3 obtained for the PDMS/TiO_2 composite indicated that the system is close to the Porod's law with uniformly dense objects characterized by almost rough surface fractal dimension. A correlation peak, observed at about 0.035 Å, associated with a characteristic length, L_{cor} of about 18 nm is observed for the silica-filled compound. In a previous study [7], the maximum of the correlation peak has been shown to shift to smaller q with the amount of filler. In our synthetic protocol, silica formation takes place in a swollen network, the network swelling ratio in TEOS, Q, determining the amount of filler. So the mean-squared end-to-end distance of a network chain in the swollen state, $\langle r^2 \rangle^{1/2}_{sw}$ can been correlated to the swelling ratio Q through the Equation (6):

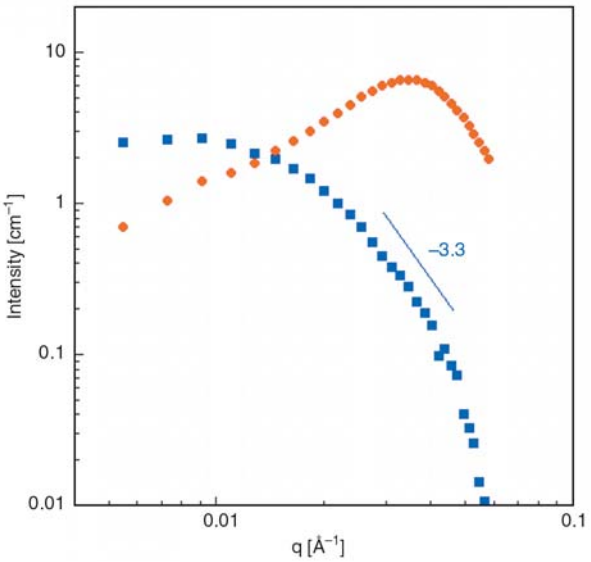

Figure 2. Small-angle neutron scattering of composites filled with 22 phr of generated particles: SiO_2 (●); TiO_2 (■)

$$\langle r^2 \rangle_{sw} = Q^{2/3} \langle r^2 \rangle_0 = Q^{2/3} C_\infty n l^2 \quad (6)$$

where C_∞ is the characteristic ratio of a chain of n bonds of length l and $\langle r^2 \rangle_0$ is the mean-squared end-to-end distance of a network chain in the unperturbed state.

A linear dependence of L_{cor} with $\langle r^2 \rangle^{1/2}_{sw}$ has been found [7] which has led to the belief that the network itself imposes a length scale on the growth of the generated particles.

3.2. Stress-strain behavior

According to the different morphologies deduced from TEM and SANS, one would predict different mechanical properties for the two types of composites. As revealed in Figure 3a, a quite different tensile behavior is observed. At small strains, a higher level of reinforcement is obtained for the titania-filled sample while at higher strains, the silica-filled sample displays a sharp increase in stress. Plots of the reduced stress, σ^* against reciprocal elongation, are presented in Figure 3b. They show a marked decrease in stress attributed to the breakdown of the filler network upon application of the deformation and an upturn in modulus at high elongations for the PDMS/SiO_2 composite. The existence of a titania network even at low filler contents has been already revealed by TEM images. The upturn in the modulus observed in the silica-filled compound is attributed to non-Gaussian effects arising from the limited extensibilities of the network chains. It is somewhat the signature of a strong polymer-filler interface resulting from the interaction between the silanols present on the silica surface and the PDMS chains. On the other hand, the excellent dispersion as well as the small size of the particles offer a large interfacial area available for polymer-filler interactions. The PDMS/TiO_2 composite does not exhibit the upturn in the modulus which reflects less interfacial adhesion between the filler particles and the polymer chains. At large deformations, the mechanical behavior of the titania-filled composite is close to that of a thermoplastic polymer with a smaller strain dependence of the stress. This plastics-like stress-strain curve is probably related to the deformation of polymer chains confined between filler particles. These network chains, which are immobilized, behave as hard filler.

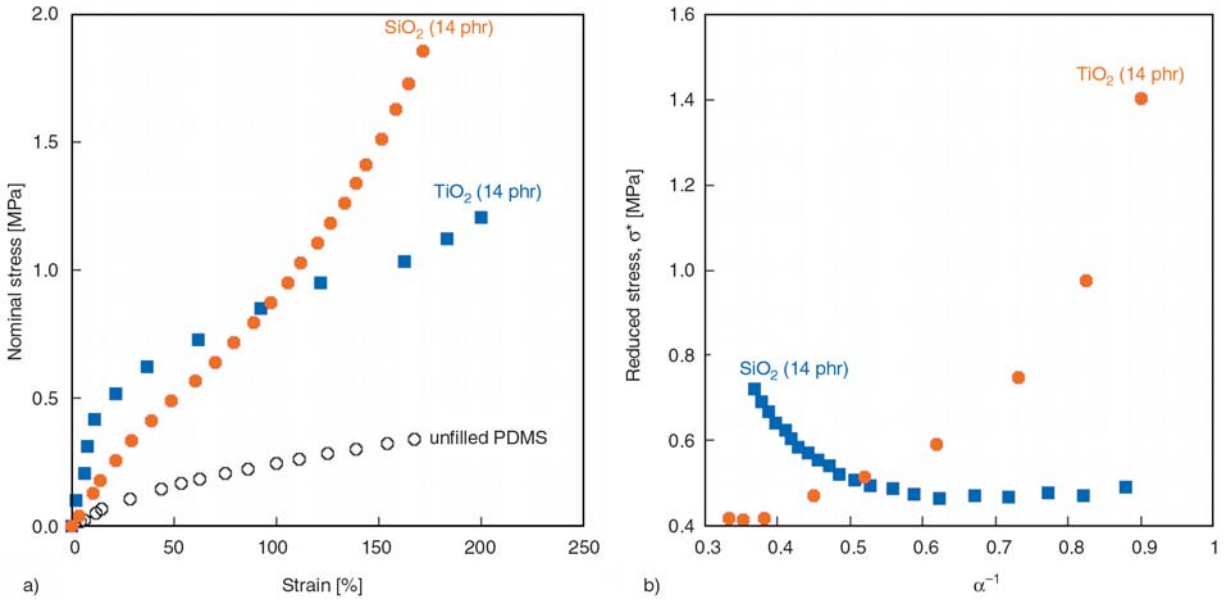

Figure 3. Comparison of the tensile behavior of PDMS composites containing a same amount of filler

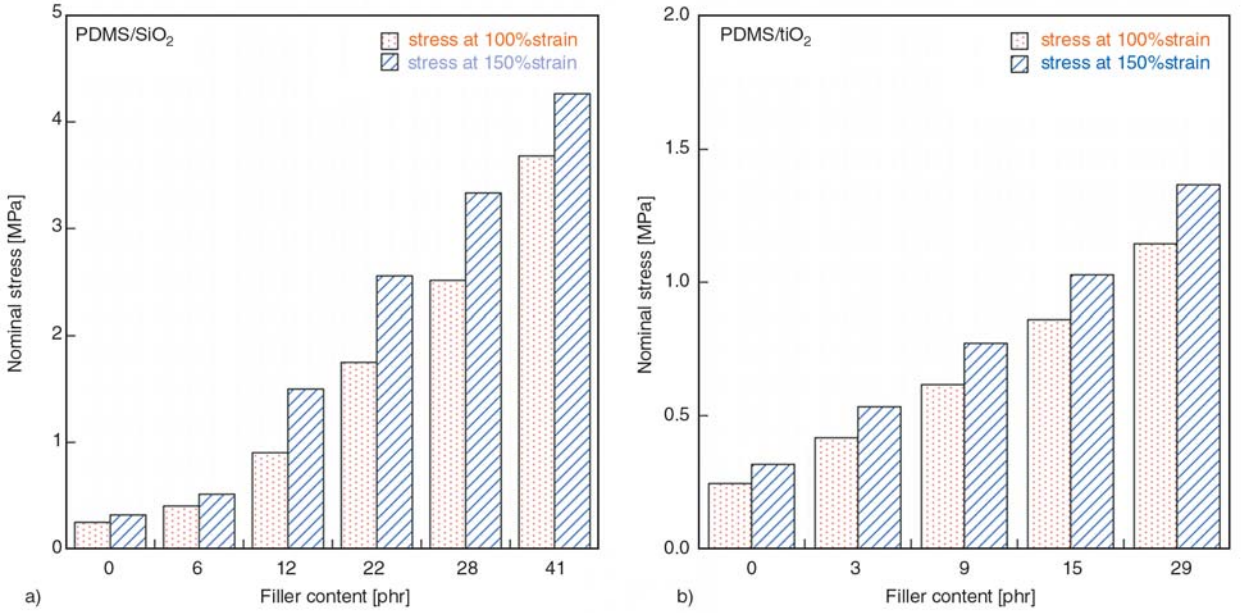

Figure 4. Tensile tests of the PDMS composites as a function of the amount of filler

Figure 4 shows the dependence of the stress at 100 and 150% strain on the amount of filler. The moduli of the composites are found to increase significantly with increase in amount of either type of filler with larger reinforcing effects at high elongations in the case of silica.

3.3. Swelling measurements

Besides the increase in the elastic modulus, another characteristic feature of filler reinforcement is a reduction in the ability of filled vulcanizates to swell in solvents. This restriction of swelling has been associated with the degree of interaction between rubber and filler. More generally, the swelling procedure has been applied in filled vulcanizates to evaluate the number the total network chain density ν ($\nu = \nu_r + \nu_f$, where ν_r is the number of effective network chains in the unfilled rubber, and ν_f is the number of additional chains produced by the bonding to the filler). This number, ν_f, of filler-rubber attachments is expected to be strongly dependent of the surface chemistry of the reinforcing filler. The advantage of the swelling measurements over the use of stress-strain measurements for estimating additional cross-linking provided by

the presence of filler is that they are free from hydrodynamic reinforcement.

Under the assumption that the filler particles do not swell, one can calculate the equilibrium swelling ratio of the rubber phase, Q_r (see Equation (7)), from the equilibrium swelling ratio, Q of the composite ($Q = V/V_d$, V being the volume of the sample plus solvent and V_d that of the dry sample) and the volume fraction of filler, ϕ:

$$Q_r = \frac{Q - \phi}{1 - \phi} \tag{7}$$

According to Kraus [20, 21], the swelling for a large number of vulcanizates containing highly reinforcing fillers has been found to obey Equation (8):

$$\frac{Q_r}{Q_{r0}} = \frac{v_{r0}}{v_r} = 1 - \frac{m\phi}{1 - \phi} \tag{8}$$

where Q_r and Q_{r0} are the rubber equilibrium swelling ratios for the filled and unfilled samples, respectively, v_{r0} is the volume fraction of the unfilled rubber after swelling, v_r is the volume fraction of rubber in the gel of the filled vulcanizate after swelling and m is defined by Equation (9):

$$m = 3c(1 - v_{r0}^{1/3}) + v_{r0} - 1 \tag{9}$$

c is a constant characteristic of the filler, but independent of the polymer, the solvent or the degree of vulcanization. This parameter arises from the manner in which the local restriction of swelling varies with the distance from the surface.

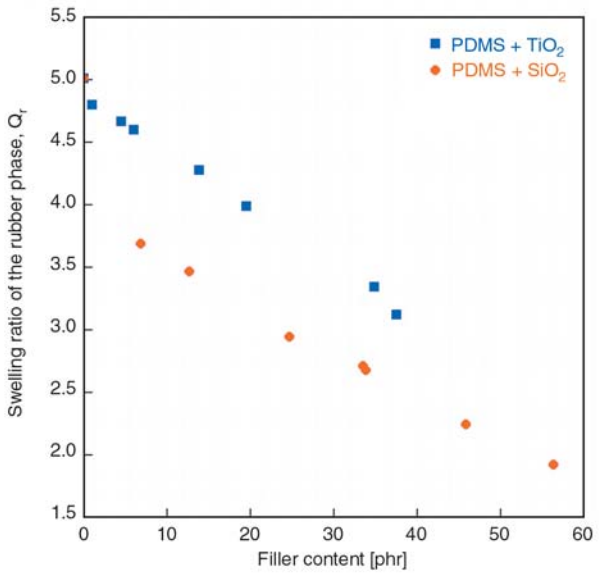

Figure 5. Dependence of rubber phase swelling on the amount of filler

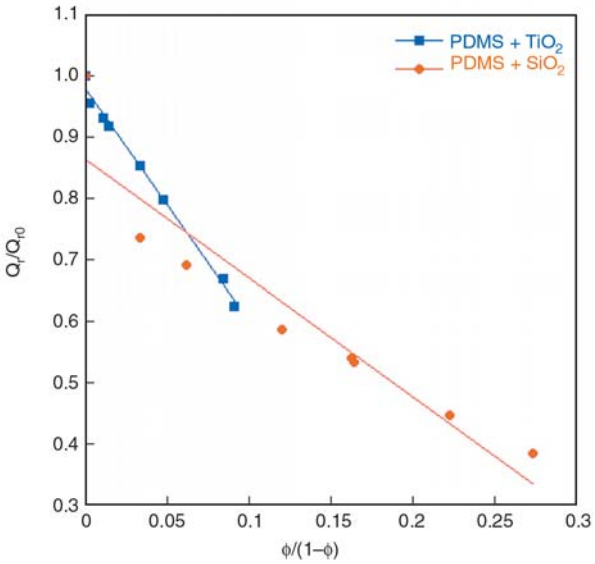

Figure 6. Plot of Q_r/Q_{r0} against filler loading expressed as volume ratio of filler to rubber

Figure 5 displays the equilibrium swelling ratio of the rubber phase in toluene, Q_r. For each type of composite, Q_r decreases with the amount of filler, indicating a pronounced restriction in swelling in the filled samples. Nevertheless, at a given filler loading, Q_r is higher for the titania-filled samples reflecting less polymer-filler linkages. Representation of Equation (8) is reported in Figure 6 and leads to slopes equal to 1.9 and 3.8 for SiO_2 and TiO_2, respectively. Values of the parameter c equal to 2.2 and 3.7 respectively can be extracted from the slopes according to Equation (9). The larger value obtained in samples filled with titania shows that restriction of swelling is extended to a larger distance from the particle surface with regard to silica analogs. This interpretation is consistent with the existence of confined polymer chains between titania particles as discussed in the previous section.

4. Conclusions

The usual sol-gel technique for the *in situ* precipitation of reinforcing particles within an elastomer is applied for the generation of silica and titania as an extension of preliminary studies reported earlier. The two types of particles exhibit two distinct morphologies, two different polymer-filler interfaces

that influence the mechanical properties of the resulting materials.

Although all composites have mechanical properties that are very much improved compared to the unfilled network, the two types of particles impart to the resulting materials a quite different tensile behavior. The high level of stress obtained at small deformations for the titania-filled PDMS reflects the formation of a filler network at a relatively low filler content. On the other hand, the low strain dependence of the stress and the absence of upturn in modulus at large deformations lead to the belief that TiO_2 is less interacting with the elastomeric phase and the polymer chains are confined between filler particles.

References

[1] Wang S., Xu P., Mark J. E.: Shear and biaxial extension measurements of reinforcement form *in-situ* precipitated silica. Rubber Chemistry and Technology, **64**, 746–759 (1991).

[2] Wen J., Mark J. E.: Precipitation of silica-titania mixed-oxide fillers into poly(dimethylsiloxane) networks. Rubber Chemistry and Technology, **67**, 806–819 (1994).

[3] Wang S-B., Mark J. E.: In-situ precipitation of reinforcing titania fillers. Polymer Bulletin, **17**, 271–277 (1987).
DOI: 10.1007/BF00285360

[4] Whang C. M., Yeo C. S., Kim Y. H.: Preparation and characterization of sol-gel derived SiO_2-TiO_2-PDMS composite films. Bulletin of the Korean Chemical Society, **22**, 1366–1370 (2001).

[5] Rajan G. S., Sur G. S., Mark J. E., Schaefer D. W., Beaucage G.: Preparation and characterization of some unusually transparent poly(dimethylsiloxane) nanocomposites. Journal of Polymer Science Part B: Polymer Physics, **41**, 1897–1901 (2003).
DOI: 10.1002/polb.10565

[6] Murugesan S., Sur G. S., Mark J. E., Beaucage G.: *In-situ* catalyst generation and controlled hydrolysis in the sol-gel precipitation of zirconia and titania particles in poly(dimethylsiloxane). Journal of Inorganic and Organometallic Polymers, **14**, 239–252 (2004).
DOI: 10.1023/B:JOIP.0000048029.08289.fe

[7] Dewimille L., Bresson B., Bokobza L.: Synthesis, structure and morphology of poly(dimethylsiloxane) networks filled with in situ generated silica particles. Polymer, **46**, 4135–4143 (2005).
DOI: 10.1016/j.polymer.2005.02.049

[8] Mark J. E.: Novel reinforcement techniques for elastomers. Journal of Applied Polymer Science: Applied Polymer Symposium, **50**, 273–282 (1992).

[9] McCarthy D. W., Mark J. E., Schaeffer D. W.: Synthesis, structure, and properties of hybrid organic-inorganic composites based on polysiloxanes. I. Poly(dimethylsiloxane) elastomers containing silica. Journal of Polymer Science Part B: Polymer Physics, **36**, 1167–1189 (1998).
DOI: 10.1002/(SICI)1099-0488(199805)36:7<1167::AID-POLB7>3.0.CO;2-R

[10] McCarthy D. W., Mark J. E., Clarson S. J., Schaeffer D. W.: Synthesis, structure, and properties of hybrid organic-inorganic composites based on polysiloxanes. II. Comparisons between poly(methylphenylsiloxane) and poly(dimethylsiloxane), and between titania and silica. Journal of Polymer Science Part B: Polymer Physics, **36**, 1191–1200 (1998).
DOI: 10.1002/(SICI)1099-0488(199805)36:7<1191::AID-POLB8>3.0.CO;2-X

[11] Breiner J. M., Mark J. E., Beaucage G.: Dependence of silica particle sizes on network chain lengths, silica contents, and catalyst concentrations in *in situ*-reinforced polysiloxane elastomers. Journal of Polymer Science Part B: Polymer Physics, **37**, 1421–1427 (1999).
DOI: 10.1002/(SICI)1099-0488(19990701)37:13<1421::AID-POLB8>3.0.CO;2-M

[12] Yuan Q. W., Mark J. E.: Reinforcement of poly(dimethylsiloxane) networks by blended and *in-situ* generated silica fillers having various sizes, size distributions, and modified surfaces. Macromolecular Chemistry and Physics, **200**, 206–220 (1999).
DOI: 10.1002/(SICI)1521-3935(19990101)200:1<206::AID-MACP206>3.0.CO;2-S

[13] Takeuchi H., Cohen C.: Reinforcement of poly(dimethylsiloxane) elastomers by chain-end anchoring to clay particles. Macromolecules, **32**, 6792–6799 (1999).
DOI: 10.1021/ma990218+

[14] Schmidt D. F., Clément F., Giannelis E. P.: On the origins of silicate dispersion in polysiloxane/layered silicate nanocomposites. Advanced Functional Materials, **16**, 417–425 (2006).
DOI: 10.1002/adfm.200500008

[15] Bradley D. C., Mehrotra R. C., Gaur D. P.: Metal alkoxides. Academic Press, London (1986).

[16] He Y-q., Ping Y-h.: Nano-composite TiO_2-PI via sol-gel process. Materials Chemistry and Physics, **78**, 614–619 (2003).
DOI: 10.1016/S0254-0584(02)00118-9

[17] Xiong M., Zhou S., You B., Gu G., Wu L.: Effect of preparation of titania sol on the structure and properties of acrylic resin/titania hybrid materials. Journal of Polymer Science Part B: Polymer Physics, **42**, 3682–3694 (2004).
DOI: 10.1002/polb.20218

[18] Bokobza L., Rahmani M., Belin C., Bruneel J-L., El Bounia N-E.: Blends of carbon blacks and multiwall carbon nanotubes as reinforcing fillers for hydrocarbon rubbers. Journal of Polymer Science Part B: Polymer Physics, **46**, 1939–1951 (2008).
DOI: 10.1002/polb.21529

[19] Breiner J. M., Mark J. E.: Preparation, structure, growth mechanisms and properties of siloxane composites containing silica, titania or mixed silica-titania phases. Polymer, **39**, 5483–5493 (1998).
DOI: 10.1016/S0032-3861(97)10276-2

[20] Kraus G.: Interactions between elastomers and reinforcing fillers. in 'Reinforcement of elastomers' (ed.: Kraus G.) New York, Wiley, 125–152 (1965).

[21] Kraus G.: Reinforcement of elastomers by carbon black. Advances in Polymer Science, **8**, 155–237 (1971).
DOI: 10.1007/3-540-05483-9_12

eXPRESS Polymer Letters Vol.4, No.6 (2010) 364–372
Available online at www.expresspolymlett.com
DOI: 10.3144/expresspolymlett.2010.46

Influence of static and cyclic climate condition on bending properties of wood plastic composites (WPC)

*A. K. Bledzki, M. Letman-Sakiewicz, M. Murr**

Institut für Werkstofftechnik, Kunststoff- und Recyclingtechnik, Universität Kassel, Germany

Received 16 November 2009; accepted in revised form 16 April 2010

Abstract. Wood and natural fiber reinforced plastic composites are established for several fields like decking, transportation and automotive applications. In the last decade, extensive researches were conducted to improve the mechanical properties, such as incorporating additives like maleic anhydride grafted polypropylene (MAH-PP). The major challenge is to keep the properties in face of the environmental influence the parts are exposed to. Therefore it's necessary to find the hardest impact factor concerning the mechanical properties. Water absorption (static and cyclic) of the composites was examined at two different temperatures (23, 50°C). A correlation between duration, kind of conditioning, temperature and modification was established. The results indicate that the coupling agent MAH-PP improved significantly the water resistance of the wood plastic composites under climatic conditions and higher temperature accelerated the rate of water absorption of the composites. The decrease of mechanical properties related to cyclic conditions is partially reversible and therefore the cyclic exposition shows less effects compared to static conditions.

Keywords: *biocomposites, WPC, coupling agent, water absorption, weathering*

1. Introduction

Wood plastic composites (WPC) containing wood plastics and additives were used to substitute wood products as well as standard plastics [1–3].

Currently, more than 1.5 million tons of WPC per year are produced worldwide. With about 1 million tons, the USA represents the largest market by far, followed by China (200 000 tons), Europe (170 000 tons), and Japan (100 000 tons). In Europe, Germany is the leading producer of wood polymer materials and, furthermore, the most significant constructor of machines.

The most important application areas of WPC are the automobile industry (automobile interior) as well as decking's and floorings, especially those for outdoor use, which are increasingly establishing themselves as an alternative to tropical- or other kinds of high quality-wood and which are subject to a two-digit growth in sales volume annually. Chinese WPC industry shows particular dynamics, where, a growth of 30 per cent can be recorded annually; until 2015, the WPC production in China is estimated to increase up to 5 million tons [4].

Due to their increased water absorption and thus, lower dimension stability, these composites are not suitable for all areas of application (e.g. wet areas). However, the desired stability can be achieved by chemical modification, for example by acetylation or by adding coupling agents [5].

To achieve the desired composite properties, the wood fibres (particles) were modified with a coupling agent. By using maleic anhydride grafted PP as a coupling agent, an increase in water resistance as well as a rise in mechanical data in comparison to untreated composites could be demonstrated [6–12].

The aim of this study was to clarify the influence of water exposition as well as static and cyclic cli-

*Corresponding author, e-mail: m.murr@uni-kassel.de

matic conditions to the composites. Static and cyclic conditions were applied at two different temperatures (23, 50°C) and a correlation between duration, kind of conditioning, temperature and modification was evaluated.

2. Composition of natural fibres

The hydrophilic characteristics of natural fibres result from their composition (Figure 1 and 2).

Natural fibers are composed of fibre bundles that consist of several elementary fibres. These elementary fibres are made up of individual layers in which cellulose fibrils are differently oriented. The middle lamella is no integral constituent of the fibre cell wall, but an exterior layer that protects the fibre from moisture expansion. In the primary wall, the cellulose fibrils form a network. The secondary wall consists of three layers. At S_1 and S_3, there is a thinner layer and in the S_2, a thicker one accounts for approx. 80% of the fibre weight. A cavity is situated in the middle of the elementary fibres (lumen). These walls (S_1, S_2, S_3, P) consist of micro fibrils [13, 14]. Figure 2 shows the composition of micro fibrils.

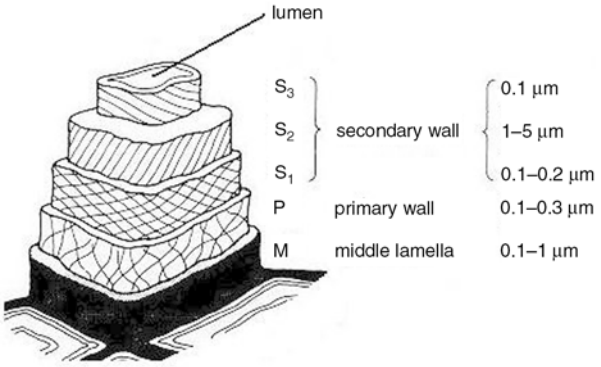

Figure 1. Composition of the elementary fibres of wood [13]

The micro fibril itself consists of approx. 60 cellulose chains. The interconnected cellulose chains belong to the crystalline areas (micelle) and single cellulose chains to the amorphous areas.

Water absorption primarily takes place in the amorphous areas of cellulose and in hemicelluloses. During this process, mainly the thicker layer of the secondary wall expands. The mechanical properties of the fibres do not only depend on the orientation of the cellulose fibrils, which exhibit a varying gradient towards the major axis of the fibre depending on the fibre type, but also on other parameters like, degree of polymerization, degree of crystallinity, pore structure, and chemical composition of the fibres [7, 13, 16, 17].

Cellulose and hemicelluloses contain several hydroxyl groups in their structure that can form hydrogen bonds with water molecules. The result is a reversible moisture expansion of the fibre that can change the mechanical characteristics. The water-cellulose interdependencies are subject to the water content of the fibres and the temperature [16].

In general, three kinds of water retention can be distinguished: free water, bound water, and capillary water. Free water is located in the lumen and described as stored water above fibre saturation. Bound water is absorbed in the cellular walls until fibre saturation. The third type of water retention takes place in the pores of the fibre wall above fibre saturation by means of capillary action [18].

Especially wood has a very large inner surface because of its microscopic capillary porosity. Consequently, it can absorb moisture from the air or other surrounding media (adsorption) or emit it (desorption). The depiction of the interdependence between relative wood moisture and relative air moisture at a constant temperature (and air pressure) level characterizes a sorption (Figure 3). Dur-

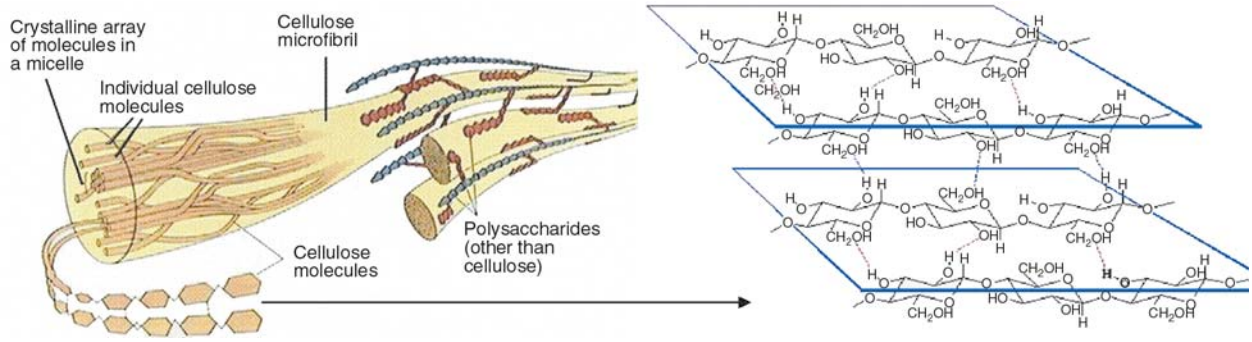

Figure 2. Composition of a cellulose fibril (left) and structure of the cellulose level (right) [15]

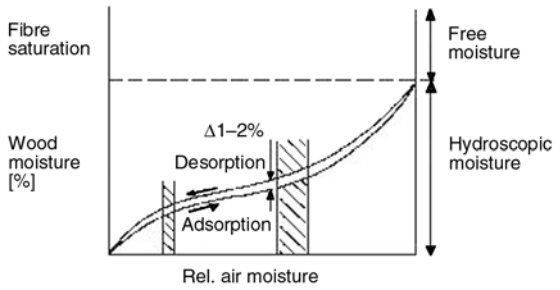

Figure 3. Typical sorption isotherm for wood [19]

ing desorption, the equilibrium moisture content is 1–2% higher than during absorption. In the case of a directional sorption, this behaviour is shown by a hysteresis curve.

Sorption takes place in the hygroscopic area and is only valid until fibre saturation. According to (DIN EN 844-4), fibre saturation is the state of a wood sample when the cellular walls are saturated with water, and there should be no water in the cellular cavities. Wood moisture depending on the kind of wood is individually assigned to a specific temperature and air moisture [19].

Thus, moisture absorption is equally divided into three phases: chemical absorption, physical absorption, and capillary condensation (Table 1).

During chemical absorption, which takes place at 0–20% of rel. humidity (*RH*), the monomolecular water layer is bound to the cellulose. In this process, the water dipoles orientate themselves towards the negative poles of the exposed OH-groups of cellulose. As long as no crystalline areas are displaced, hardly any external volume extension follows the molecular sorption. The phase of adsorption extends from approx. 20–60% of *RH*. The attachment of water molecules happens by means of electrostatic and Van der Waals' forces. Yet, the polymolecular water layer developed this way is distributed unevenly. The water molecules depend less on the boundary layer with increasing layer thickness. They begin to show fluid characteristics (surface tension, flowability). Above approx. 60% of *RH*, less vapour saturation pressure leads to capillary condensation. This condensation still takes place in the cellular wall structure. The water is adsorbed in the intermicellular and interfibrillar cavities. Only when the fibrils cannot extend anymore because of the relatively strong bonds in the crystalline areas, fibre saturation is completed and the end of the hygroscopic area is reached [10, 11, 19, 20]. The sorption phases overlap each other and occur locally distributed. The sorption behaviour is influenced by temperature.

3. Experimental part

3.1. Materials

3.1.1. Wood fibres (particle)

The soft wood fibres BK 40-90 (spruce), provided by J. Rettenmaier & Söhne GmbH + Co.KG Rosenberg, Germany, were used as filling material (see Tables 2 and 3).

3.1.2. Matrix

The polypropylene Homopolymer SABIC® PP 575P, provided by the company Sabic Euro Petrochemicals B.V., Sittard, Netherlands, was used as matrix polymer.

Table 2. Characteristics of used wood fibres

Name	Lignocel® (BK 40-90)
Type	soft wood (spruce)
Structure	cubic
Particle area	300–500 μm
Colour	yellow
pH-value	5.5±1
Density	1.5 g/cm^3

Table 3. Chemical composition of employed wood fibres in weight [%] [21]

Main components of the fibres	Soft wood fibres	
	Literature [10, 19][1]	Experimental
Cellulose	40–45	43
Hemicellulose	25–30	24
Lignin	26–34	30
Extracts	0–5	3

[1]the references do not refer to the product Lignocel Chemical

Table 1. Kinds of water bonds in wood [10, 11]

Relative air moisture	Wood moisture	Moisturization-drying phase	Water bonds
0–20%	0–6%	chemical absorption	bound water
20–60%	6–15%	physical absorption	bound water
above 60%	below 30%	capillary condensation	bound water
100%	above 30%	capillary condensation	free water

Table 4. Characteristic data of the employed matrix materials

Characteristics	Polypropylene	Coupling agent
Trade name	SABIC® PP 575P	Licomont AR 504
Chemical nomination	Isotactic PP	Maleic anhydride grafted PP
Density	0.905 g/cm^3	0.89–0.93 g/cm^3
Vicat-temperature	152°C	154–158°C
Viscosity	–	~800 mPa·s
MFR	10.5 g/10 min (230°C/2.16 kg)	>1000 g/10 min (190°C/2.16 kg)
Acid value	–	37–45 mg KOH/g

3.1.3. Coupling agent

Maleic anhydride grafted polypropylene (MAH-PP), provided by Clariant Produkte GmbH Gersthofen, Germany, was used as coupling agent. The information given by the manufacturers about their matrix polymers and coupling agents is listed in Table 4.

3.2. Manufacturing of the specimens

Wood fibre was mixed with PP using a high speed mixer (Henschel Mixer, type HM40 KM120) with and without coupling agent (MAH). The soft woof fibre (SW) was dried at 80°C in an air circulating oven for 24 h (until the moisture content became <1%) before mixing. The fiber content is 50%. The specimens of wood fibre composites were prepared by injection moulding using a Klöckner Ferromatik FM 85. At 160 to 180°C and with the mould temperature kept at 80 to 100°C.

3.3. Conditioning of the fibres

With percental moisture content, the relation between the mass of moisture in the wood and the mass of dry wood is denoted. For this reason, the dried wood fibres (3 g) were stored at a relative humidity of 65 and 95% as well as an ambient temperature of 20±3°C. The moisture absorption in equilibrium was determined with a precision of 0.0001 g. The wood fibre samples were weighed after certain periods of time (24, 48, 96 h etc.) until they reached a constant weight (saturation point). In doing so, a double determination was carried out and the resulting value was represented as average value.

3.4. Conditioning of the samples

The composites were conditioned under different circumstances. The immediate influence of water (by static water conditioning) as well as the results of cyclic moisturization-dehydration on physical and especially mechanical data were determined. The data of all conditioned samples were compared with the values of the samples conditioned in standard climate. In this context, it is important to know in how far the manipulations are irreversible or can be reversible by subsequent dehydration.

3.4.1. Conditioning in standard climate

The term ‘samples conditioned in standard climate’ refers to those samples which were exclusively stored at standard climate (DIN 50014) in the testing room for 48 hours and tested without further conditioning.

3.4.2. Static and cyclic water absorption

Static water absorption was determined according to DIN EN ISO 62. Cyclic water absorption took place in accordance with the same standard.
During cyclic storage in water, the materials were soaked in water for 24 h and were dried at the same temperatures for 24 h; this represents a cycle.

3.4.3. Static and cyclic climate conditioning

The ageing of the samples took place in appropriate conditioning cabinets. Static climate conditioning was carried out according to DIN EN 60068-2-78. The WPC samples were conditioned over 6 weeks at 40°C and with a relative humidity of 95%.
Figure 4 shows the implemented climatic cycle which took 24 h.

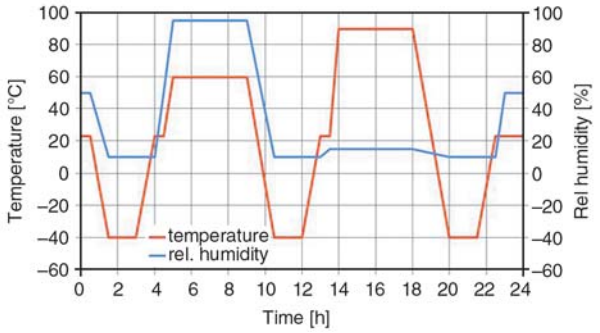

Figure 4. Adjustment parameters of the cyclic climate test

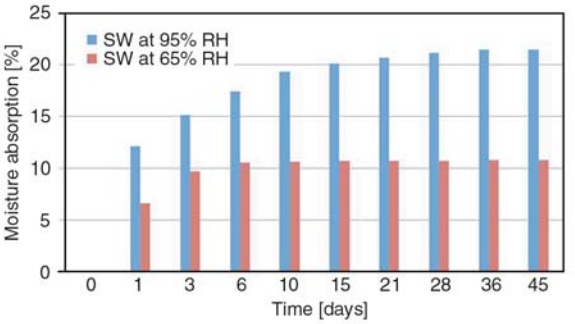

Figure 5. Influence of relative air moisture on moisture absorption of soft wood fibres (SW)

The following conditions were integrated: dry/cold, warm/humid, hot/dry, and a standard condition (23°C/50% *RH*).

3.4. Bending test

The determination of bending properties was carried out according to DIN EN ISO 178 using injection-moulded standard specimens in a universal testing machine type Zwick1446. Depending on the ambient climate, 5 to 10 specimens were used.

4. Results and discussion

4.1. Moisture absorption of the wood fibres

The moisture absorption was investigated at a relative moisture level of 65 and 95% and at an ambient temperature of 20±3°C. Figure 5 shows the differing moisture absorptions of soft wood fibres.

The investigations carried out show that the speed of moisture absorption depends on the degree of moisture. Accelerated moisture absorption occurred during the first three days at a moisture level of 65% and up to ten days at a level of 95%. The equilibrium moisture of the soft wood fibres was reached after two weeks at 65% of *RH* and after about three weeks at 95% of *RH*.

4.2. Static water absorption of the composites

The influence of coupling agent application and conditioning temperature on static water absorption of wood composites is depicted in Figure 6.

It was determined that water absorption takes place in a higher amount and faster at 50°C-conditioning. Within three months during static water storage at ambient temperature, approximately the same percentage amount of water was absorbed as within one month at 50°C. In both cases, the modified samples show lower water absorption in comparison to the untreated ones. The difference between untreated and modified WPCs after 112 days of water conditioning is about 26% at 23°C and about 11% at 50°C.

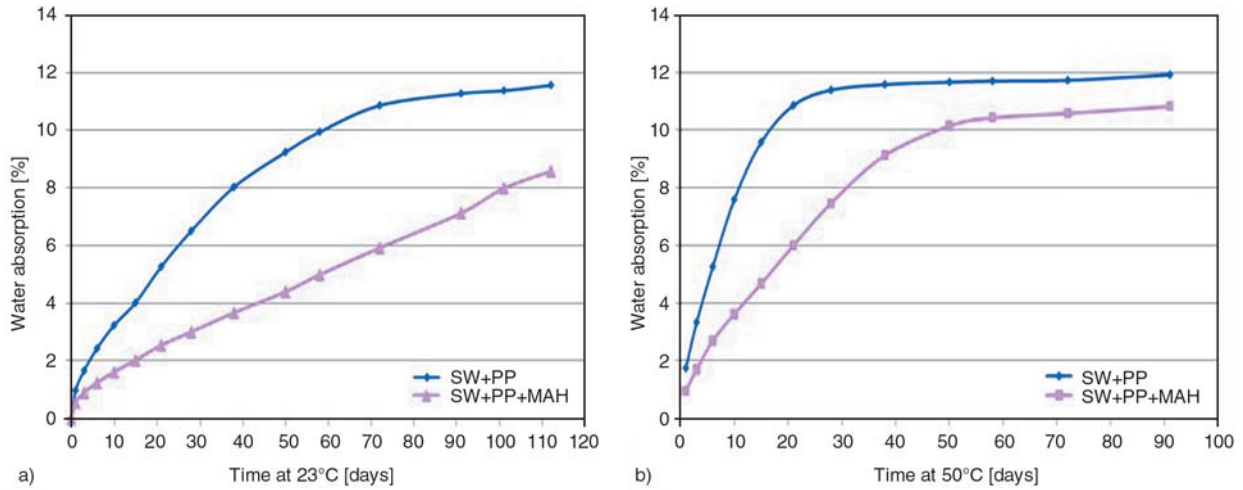

Figure 6. Influence of fibre modification and conditioning temperature on static water absorption of WPC

4.3. Cyclic water absorption of the composites

In order to compare the experimental results of static water conditioning, cyclic water absorption was carried out at 23 and 50°C. The influence of the temperature on cyclic water absorption behaviour is depicted in Figure 7.

Despite the augmentation in conditioning temperature which leads to an increase in water absorption, the water absorption and -desorption of the samples have mainly proven to be reversible.

At both conditioning temperatures, the modified samples exhibit lower water absorption in comparison to the untreated composites.

As for static water absorption, the conditioning temperature is an important factor here. With increasing temperature, the water absorption of the composites increases by approximately 50% after 50 days in comparison to the WPC's conditioned at 23°C.

Besides, periodic water conditioning shows that after 50 days, the composites conditioned in cycles exhibit a water absorption which is 40% (50°C), and 52% (23°C) respectively, lower in comparison to the samples stored in water under static conditions. With regard to the materials treated with MAH-PP, the difference is approximately 42% (23°C), and 56% (50°C) respectively.

As the storing period includes moisturization and drying, the results of water absorption behaviour after 50 days of cyclic storage were compared with that of static water conditioning after 25 days. The difference in water content between the material stored under static and that stored under cyclic conditions is up to 25% at 23°C and approximately 35% at 50°C.

4.4. Bending experiments after static water absorption

The influence of static water storage on the bending properties of WPC is shown in Figure 8.

Static water conditioning clearly influences the bending stability. At both conditioning temperatures, a considerable decrease of the characteristic values was observed. The composites treated with MAH-PP possess a bending stability which is up to 35% higher in comparison to the unmodified materials; but a clear reduction (approx. 30%) of the characteristic values of the treated wood-PP was observed due to this conditioning.

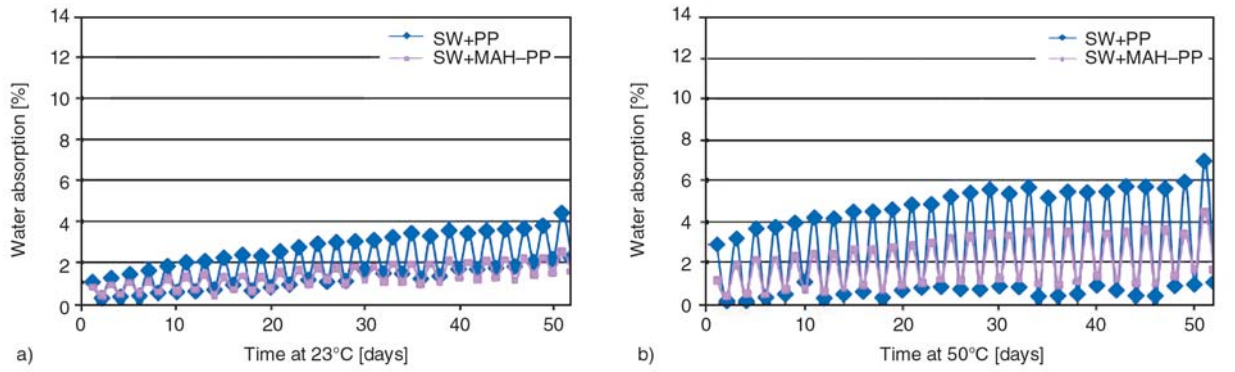

Figure 7. Influence of fibre modification and conditioning temperature on cyclic water absorption of WPC

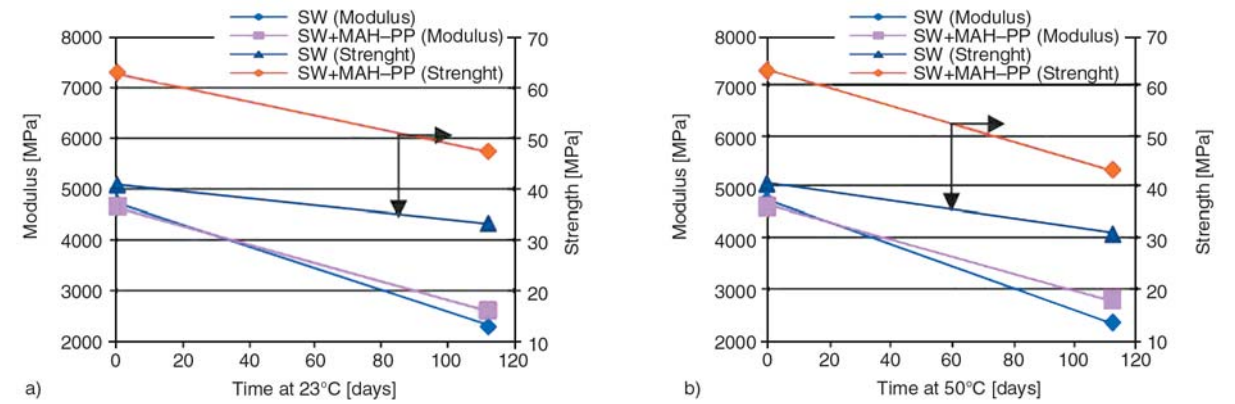

Figure 8. Influence of static water storage on the bending properties of WPC (arrows refer to the axes)

By absorbing moisture, wood plastic composites normally undergo a kind of softening, that is, with increasing moisture content, the stiffness of the materials decreases. Apart from this, a higher temperature can be detected which undoubtedly plays a role as well.

4.5. Bending experiments after cyclic water absorption

After 10, 20 and 30 cycles of cyclic water storage, bending experiments were carried out (Figure 9). These figures show that cyclic water storage at 23°C does not cause a remarkable change of the bending stabilities of the set treated with a coupling agent and the untreated one. At 50°C, a small decrease in stiffness (approx. 10%) can be observed. The specimens treated with MAH-PP altogether show a bending stability that is approx. 40% higher than that of the untreated materials. Due to this, the first irreversible effects of cyclic conditioning can be observed with regard to the bending stabilities. At both conditioning temperatures, a reduction of the *E*-modulus could be detected. The highest decrease in stiffness (approx. 32%) can be observed in the untreated materials.

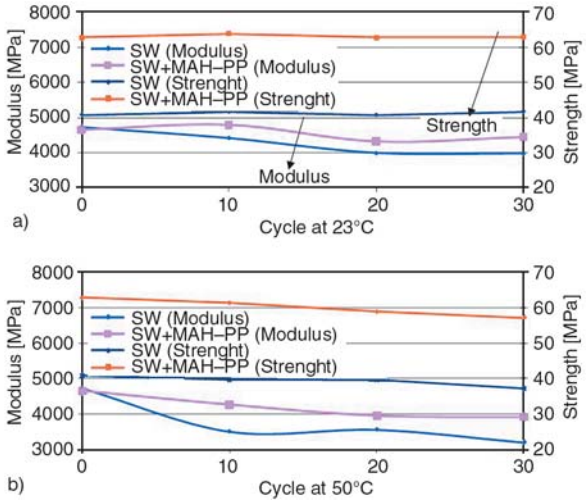

Figure 9. Influence of cyclic water storage on the bending properties of WPC

4.6. Bending experiments after static climate conditioning

The influence of static climate conditioning on the bending properties of WPC was investigated as well (see Figure 10).

It was determined that the stability values of all materials show no significant differences. In this context, the materials which were treated with a coupling agent exhibit a bending stability up to 36% higher than the untreated composites.

In comparison to the unconditioned samples, the characteristic values of the moduli of modified and unmodified WPC's decreased, and especially those of the non-modified composites by approx. 24% after six weeks of storing. Additionally, the WPCs treated with a coupling agent show slightly higher stiffness values in comparison to the untreated materials here.

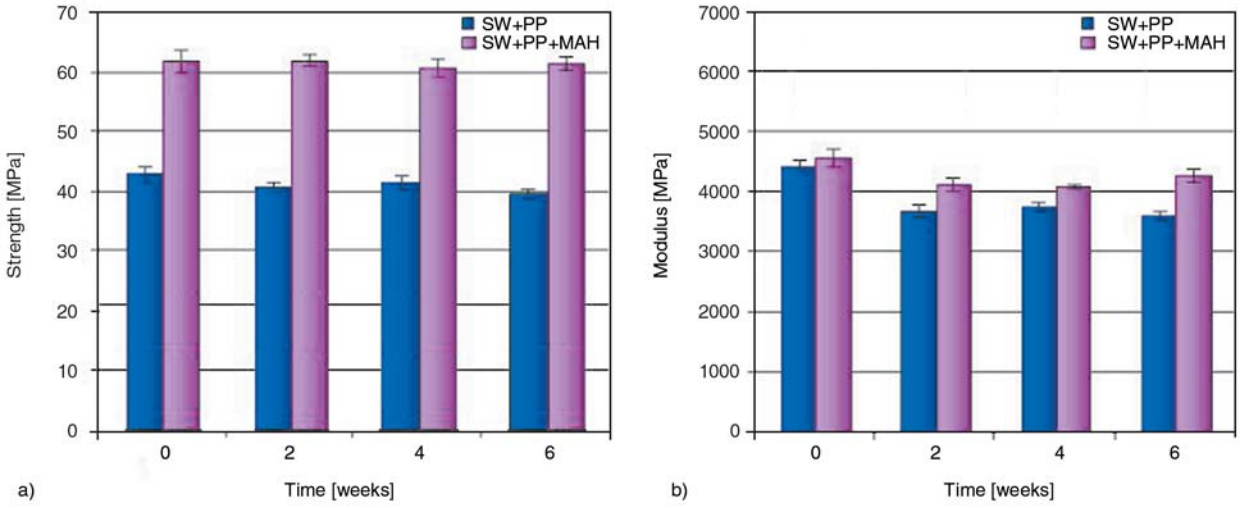

Figure 10. Influence of static climate conditioning (40°C, 95% of *RH*) on the bending properties of WPC

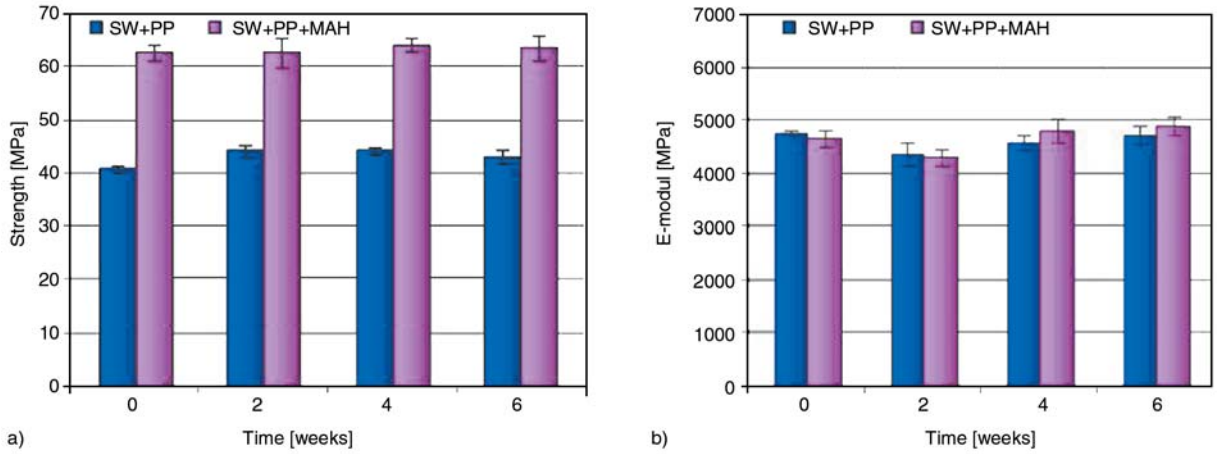

Figure 11. Influence of cyclic climate conditioning

4.7. Bending experiments after cyclic climate conditioning

The following Figure 11 shows the bending behaviour of the WPC-materials after storage in Cyclic Climate.

While there are only slight changes within the test series, the samples treated with a coupling agent show no change in bending stability after six weeks of storing in comparison to the unconditioned sample. The modified WPC-samples show stiffness values that are up to 32% higher than those of the unmodified sets.

The stiffness values are only marginally influenced by cyclic conditioning.

The investigations carried out prove that the stability- and stiffness values of WPC remain unchanged after six weeks of climatic exposition in comparison to the untreated.

5. Conclusions

Static and cyclic water absorption:

– The higher temperature (50°C) causes water absorption to become higher and three times faster.
– At both temperatures, a significant decrease (20–30%) of the mechanical data was determined, while the materials treated with a coupling agent have characteristic values that are approx. 35% higher.
– The cyclic sorption graph increases asymptotically and causes significantly lower water absorption in comparison to the statically stored samples.
– The mechanical characteristics show no decrease in stability values after two months of cyclic water storage at 23°C and only a slow decrease at 50°C. However, at both conditioning temperatures, a reduction of the modulus was detected.

Static and cyclic climate conditioning:

– While the stability values were hardly influenced, slight changes in the characteristic values can be observed with regard to the modulus.
– After six weeks of cyclic climate conditioning, approx. the same mechanical values of all materials were measured as in the original sample.

It was shown that the a higher temperature can accelerate the absorption rate and volume of WPCs. Coupling agents causes an improvement of moisture resistance and mechanical properties in WPC. Besides, it could be proved that after cyclic influences on moisture and temperature and subsequent drying, the mechanical values of the composites are at the level of the original data.

References

[1] Bledzki A. K., Sperber V. E., Faruk O.: Natural and wood fibre reinforcement in polymers. Rapra, Shrewsbury (2002).

[2] Dale Ellis W., O'Dell J. L.: Wood-polymer composites made with acrylic monomers, isocyanate, and maleic anhydride. Journal of Applied Polymer Science, **73**, 2493–2505 (1999).
DOI: 10.1002/(SICI)1097-4628(19990919)73:12<2493::AID-APP18>3.0.CO;2-C

[3] Bledzki A. K., Gassan J.: Composites reinforced with cellulose based fibres. Progress in polymer Science, **24**, 221–274 (1999).
DOI: 10.1016/S0079-6700(98)00018-5

[4] Jäger A.: Market growth WPC. Biowerkstoff-Report, **7**, 18–19 (2010).

[5] Rowell R. M.: Handbook of wood chemistry and wood composites. Taylor and Francis, New York, (2005).

[6] Nechwatal A., Reußmann T., Böhm S., Richter E.: The dependence between the process technologies and the effect of MAH-PP-adhesives in natural fibre reinforced thermoplastic composites. Engineering Materials, **7**, 68–73 (2005).
DOI: 10.1002/adem.200400138

[7] Rowell R. M., Lange S. E., Jacobson R. E.: Weathering performance of plant fiber/thermoplastic composites. Molecular Crystals and Liquid Crystals, **353**, 85–94 (2000).
DOI: 10.1080/10587250008025650

[8] Ichazo M. N., Albano C., González J., Perera R., Candal M. V.: Polypropylene/wood flour composites: Treatments and properties. Composites Structures, **54**, 207–214 (2001).
DOI: 10.1016/S0263-8223(01)00089-7

[9] Cantero G., Arbelaiz A., Mugika F., Valea A., Mondragon I.: Mechanical behavior of wood/polypropylene composites: Effects of fibre treatments and ageing processes. Journal of Reinforced Plastics and Composites, **22**, 37–50 (2003).
DOI: 10.1177/0731684403022001495

[10] Ruch J., Fritz H. G.: Compounding and characterisation of long fibre reinforced composites based on flax and polypropylene. in 'ANTEC 2002, 60th Annual Technical Conference, San Francisco, USA' Vol 2, 2180–2184 (2002).

[11] Gassan J.: Naturfaserverstärkte Kunststoffe- Korrelation zwischen Struktur und Eigenschaften der Fasern und deren Compositen. PhD thesis, Universität Kassel (1997).

[12] Bledzki A. K., Sperber V. E., Specht K., Letman M., Viksne A.: Effect of defined waxes and coupling agents on moisture behavior of injection molded wood fiber reinforced PP composites. in '8th International Conference on Woodfiber-Plastic Composites (and other Natural Fibers), Madison, USA' 229–238 (2005).

[13] Fengel D., Wegener G.: Wood-chemistry, ultrastructure, reactions. European Journal of Wood and Wood Products, **42**, 314 (1984).
DOI: 10.1007/BF02608943

[14] Wagenführ R.: Anatomie des Holzes. DRW-Verlag, Leinfelden-Echterdingen (1999).

[15] Letman M.: Holzgefüllte Kunststoffe- eine kreative Werkstoffinnovation für technische Anwendungen. PhD thesis, Universität Kassel (2007)

[16] Klemm D., Philip B., Heinze T.: Comprehensive cellulose chemistry. Volume 1: Fundamentals and analytical methods. Wiley, Weinheim (1998).

[17] Schneider Ch.: Chemische und morphologische Veränderungen von Zellstoffen während der Bleiche und deren Auswirkung auf die technologischen Eigenschaften. PhD thesis, TU-Darmstadt (2000).

[18] Thienel K. Ch.: Bauchemie und Werkstoffe des Bauwesens: Holz, Skript zur Vorlesung. Universität München, München (2006).

[19] Niemz P.: Physik des Holzes und der Holzwerkstoffe. DRW Verlag, Leinfelden-Echterdingen (1993).

[20] Kollmann F.: Technologie des Holzes und der Holzwerkstoffe, Band 1. Springer, Berlin (1951).

[21] Bledzki A. K., Letman M., Viksne A., Rence L.: A comparison of compounding processes and wood type for wood fibre-PP composites. Composites Part A: Applied Science and Manufacturing, **36**, 789–797 (2005).
DOI: 10.1016/j.compositesa.2004.10.029

eXPRESS Polymer Letters Vol.4, No.6 (2010) 373–381
Available online at www.expresspolymlett.com
DOI: 10.3144/expresspolymlett.2010.47

Photocatalytic polymerization induced by a transparent anatase titania aqueous sol and fabrication of polymer composites

X. X. Wang[1], *H. T. Wang*[1*], *X. M. Song*[1], *G. Q. Wang*[2], *Q. G. Du*[1], *Q. T. Chen*[3]

[1]Key Laboratory of Molecular Engineering of Polymers of Ministry of Education, Department of Macromolecular Science, Fudan University, Shanghai 200433, People's Republic of China
[2]Innovative Systems and Materials Laboratory, Shanghai Research Institute, Hitachi (China) Research & Development Corporation, Shanghai 200020, People's Republic of China
[3]Shanghai Koito Automotive Lamp Co., Ltd, Shanghai 201821, People's Republic of China

Received 20 November 2009; accepted in revised form 23 April 2010

Abstract. The surface modification of the anatase titania nanoparticles prepared via a controlled nonhydrolytic sol-gel process is achieved by the formation of the bidentate coordination between titania and methacrylic acid (MAA) molecules. The *in situ* photocatalytic polymerization of methyl methacrylate (MMA) monomer is initiated by surface modified anatase titania nanoparticles under Xe lamp irradiation. A variety of techniques including differential scanning calorimetry (DSC), thermo-gravimetric analysis (TGA) and scanning electron microscopy (SEM) are employed to characterize the resulting materials. The glass transition temperatures and the thermal stabilities of polymethyl methacrylate (PMMA) composite materials prepared via photocatalytic polymerization are enhanced compared with pure polymer. The partial aggregation of titania nanoparticles in PMMA composite films is derived from the surface polymerization of MMA, which makes the inorganic particles hydrophobic and drives them to the water/oil interfaces.

Keywords: *polymer composites, thermal properties, titania, morphologies*

1. Introduction

At present, titania has been considered as one of the most studied semiconductors and widely used in gas sensors [1], as a pigment [2], in solar-energy conversion [3, 4] and as a promising photocatalyst for water and air purification [5] because of its high oxidative power, chemical stability, low cost and nontoxicity [6]. Titania is also used as a photocatalyst to initiate polymerization of vinyl monomers without adding any photosensitizers, which has acquired important progresses in this aspect [7–9]. Ni *et al*. [7] studied the kinetics of the photopolymerization of methyl methacrylate initiated by titania nanopowders in aqueous suspensions. Damm and coworkers [8, 9] reported the influence of the properties of titania on the photocatalytic acrylate polymerization and also investigated the photopolymerization of an ethoxylated trisacrylate initiated by iron-doped titania particles. Most of the research articles concerned the photocatalytic polymerization induced by crystalline titania powders. A transparent anatase titania aqueous sol, however, as the photocatalyst to initiate polymerization of vinyl monomers has hardly ever been studied. The titania nanoparticles in the sol normally have smaller particle size (less than several tens nanometers) and less aggregation because of hydrophilic surfaces and electrostatic repulsion of nanoparticles. The *in situ* photocatalytic polymerization induced by titania aqueous sol may decrease the

*Corresponding author, e-mail: wanght@fudan.edu.cn

aggregation of inorganic nanoparticles in polymer matrices. With the increasing interests in the preparation of polymer/inorganic nanocomposites, including polymer/titania composite materials [10, 11], the homogeneous dispersion of the inorganic nanoparticles in the polymer matrices avoiding macroscopic phase separation is very important at any time. Therefore, the surface functionalization of titania nanoparticles has attracted increasing attention. There have been several methods for the modification of titania particles. One is using a silane coupling agent to functionalize nanosized titania [12–14]. Second is encapsulating titania particles within organic polymers by various polymerization methods [15–17]. The third method is surface modification of the titania nanoparticles with bifunctional molecules [18, 19].

In this work, we report a practical and convenient method to prepare a stable and transparent anatase titania aqueous sol. This preparation method was based on a nonhydrolytic sol-gel process using titanium tetrachloride as precursor in ethanol solution. The solution was then dried at 80°C to produce anatase titania nanoparticles and they were dispersed in water to obtain the titania sols. After functionalization of the anatase titania surface with methacrylic acid coupling agent, the PMMA/titania composite materials were synthesized through an *in situ* photocatalytic polymerization of methyl methacrylate under Xe lamp irradiation. This preparation method is environmentally friendly approach because no organic solvent is used in the polymerization process. The influence of surface modification of anatase titania nanoparticles on the morphology and thermal properties of PMMA composite materials was investigated. A tentative mechanism for the partial aggregation of titania nanoparticles during photocatalytic polymerization process was also presented.

2. Experimental

2.1. Materials

Titanium (IV) chloride ($TiCl_4$, chemical reagent grade), ethanol (EtOH, analytical reagent grade), methanol (MeOH, analytical reagent grade), methyl methacrylate (MMA, analytical reagent grade), azobisisobutyronitrile (AIBN, chemical reagent grade), methacrylic acid (MAA, analytical reagent grade) and tetrahydrofuran (THF, analytical reagent grade) were purchased from Shanghai Chemical Reagent Company, Shanghai, China. MMA was purified by distillation and AIBN was recrystallized before use. $TiCl_4$, ethanol, MAA, methanol and THF were used without further purification. Deionized water was used in the experiments.

2.2. Synthesis of anatase titania sol

The anatase titania sol was prepared by a convenient nonhydrolytic sol-gel method. Briefly, $TiCl_4$ was slowly added to anhydrous ethanol under vigorous stirring. The mixture was stirred magnetically at room temperature for 12 h and then dried at 80°C for 20 h to produce off-white powders. They were grinded by a ball mill (QM-3SP04, Nanjing University Instrument Plant, Nanjing, China) at room temperature for 24 h and the nanosized titania particles were obtained. The 5 wt% anatase titania sol was produced after dispersion of 1 g titania nanoparticles in 19 g deionized water.

2.3. Surface modification of anatase titania nanoparticles

The surface modification of anatase titania nanoparticles was performed by mixing 20 g 5 wt% anatase titania sol with different contents (0.11 or 0.25 g) of MAA coupling agent. The solution was then stirred magnetically at room temperature for 12 h in dark. The content of MAA in titania/MAA system was 10 and 20 wt%, respectively.

2.4. Preparation of PMMA/titania composite materials

The PMMA/titania composite materials were prepared by *in situ* photocatalytic polymerization of MMA in the presence of the surface modified anatase titania sol. The mixtures of 9 g MMA monomer and 20 g above mentioned surface modified anatase titania sol were deoxygenated by bubbling with nitrogen for 20 min. Then the glass flasks were sealed and the polymerization was carried out by exposing the flask to a XQ 500W Xe lamp (the distance of the glass flasks to the Xe lamp was 20 cm) with continuous stirring for 48 h at room temperature. The products were filtered and dissolved in a good solvent of PMMA (THF) fol-

lowed by being precipitated in water. And then they were filtered and dried at 50°C for 48 h to obtain the PMMA/titania composite materials. For comparison, the polymerization of MMA using unmodified titania sol was also performed under the same experimental conditions.

2.5. Preparation of PMMA homopolymer

For comparison, PMMA homopolymer was also prepared via a conventional free radical polymerization described as follows. The monomer MMA and the initiator AIBN (0.2 wt% in the monomers) were added to a reaction flask and then polymerized at 70°C under nitrogen atmosphere for 12 h. The resulting polymer was purified by precipitating in methanol and then dried at room temperature under vacuum. The molecular weight (M_w) of PMMA was ~120 000 g/mol and its polydispersity (D) was 1.8.

2.6. Preparation of PMMA/titania composite films

To prepare PMMA/titania composite films, 2 g composite materials were dissolved in 15 g THF by vigorous stirring and the mixture was cast on a polyethylene terephthalate (PET) substrate and dried at 50°C in the oven for 10 h. For comparison, the PMMA/titania material via subsequent addition of titania was also prepared. 1.8 g PMMA homopolymer was dissolved in 15 g THF by vigorous stirring followed by the addition of 0.2 g the as-synthesized titania nanoparticles with continuous stirring for 2 h. Then the mixture was also cast on a PET substrate and dried at 50°C in the oven for 10 h. The thickness of these composite films was in the range of 50–60 μm.

2.7. Measurements

FT-IR spectra were measured on a Nicolet NEXUS-470 spectrometer. The pure and modified titania nanoparticles were dried and washed with ethanol carefully. Then the powders were dried in a vacuum oven and pressed into KBr pellets for FTIR measurements. The absorption spectra of anatase titania sol was recorded using a Perkin-Elmer Lambda 35 UV/Vis spectrometer. The thermal stability of pure PMMA and the PMMA/titania composite materials was investigated by thermo-gravimetric analysis (TGA) using a Perkin-Elmer Pyris 1 thermogravimetric analyzer. The measurements were conducted at a heating rate of 20°C/min in air atmosphere. Differential scanning calorimetry (DSC) tests of pure PMMA and the composite materials were performed at a heating rate of 10°C/min in the nitrogen atmosphere using a Perkin-Elmer DSC-7 apparatus. Transmission electron microscopy (TEM) investigations were performed on a Hitachi H-600 microscope. The samples for TEM observation were prepared by adding 1–2 drops of the anatase titania sol on lacey carbon copper grids. The X-ray powder diffraction (XRD) patterns were measured on an X'Pert PRO (PANalytical) diffractometer at room temperature with CuK_α radiation. XRD diagrams were obtained for the range of $2\theta = 20–80°$. The morphologies of the fractured surfaces of the PMMA/titania composite films were observed with a JSM-5600LV and SUPERSCAN SS-550 scanning electron microscope (SEM). The particle size and particle size distribution were determined by measurement of about 300 particles. Gel permeation chromatographic (GPC, Agilent 1100, USA) analysis was carried out at 30°C at a flow rate of 1ml/min using THF as the solvent. The instrument was calibrated using polystyrene as standard.

3. Results and discussion

3.1. Properties of the anatase titania sol

Figure 1 shows the UV/Vis spectrum of the transparent anatase titania sol. It can be found that the sol has a strong absorption in UV region, while it is

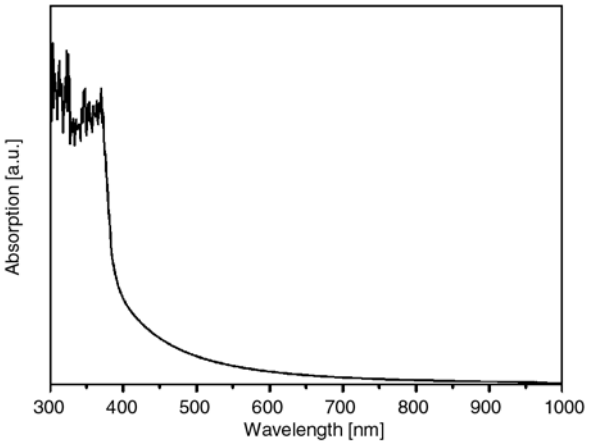

Figure 1. UV/Vis spectrum of the prepared anatase titania sol

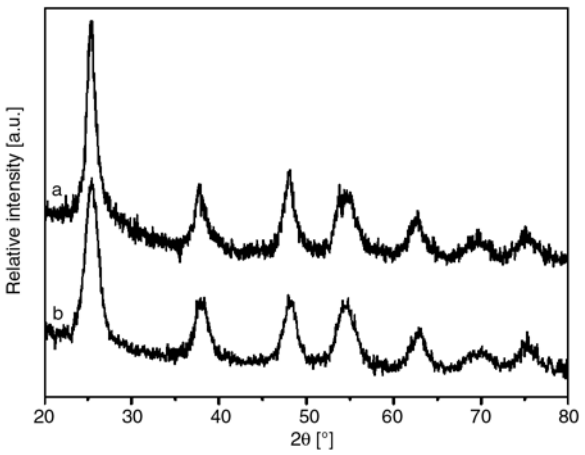

Figure 2. XRD patterns of (a) original titania nanoparticles and (b) the dried titania sol

almost transparent in visible region. This is in accordance with its appearance detected by eye. No precipitation is found after 3 months, which indicates that the anatase titania sol is very stable at room temperature.

Figure 2 presents the XRD patterns of the original titania nanoparticles obtained by the controlled nonhydrolytic sol-gel process and the dried titania sol. It is seen that there is almost no difference in the XRD patterns between these two kinds of nanoparticles. They both show well-defined diffraction peaks characteristic of anatase phase [20] and the crystal size determined by the Scherrer equation is about 9 nm. These facts suggest that crystallinity of the anatase titania nanoparticles is not affected after dispersion in water.

Transmission electron microscopy (TEM) was used to examine the size of anatase titania sol as shown in Figure 3. The average size of the titania nanoparticles in sol is around 20 nm, which is bigger than the crystal size determined by XRD. This is due to the incomplete crystallinity of these titania nanoparticles. The anatase titania nanoparticles may have applications in the photocatalytic polymerization and the preparation of polymer/titania nanocomposites.

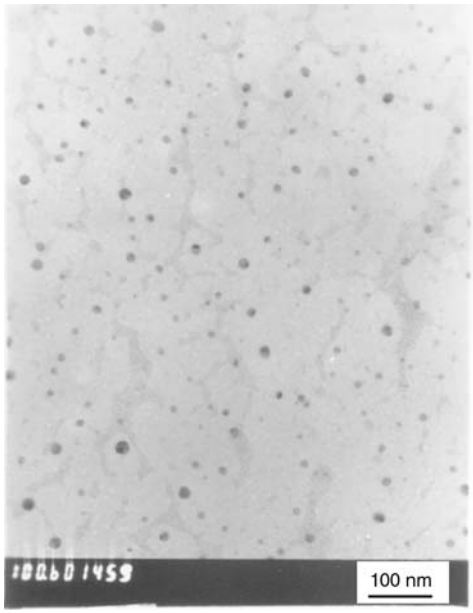

Figure 3. TEM image of the prepared anatase sol

3.2. FT-IR spectra of the modified anatase titania nanoparticles

The FT-IR spectra of anatase titania sol modified with different content of MAA after careful rinse are shown in Figure 4. The original titania particles (Figure 4a) have no absorption peaks from 1400 to 1800 cm^{-1} except a strong bands at 1630 cm^{-1} which is the characteristic of bending vibration of water molecules [21]. For the samples after functionalized by MAA coupling agent (Figure 4b and 4c), the peak at 1721 cm^{-1} is attributed to typical C=O vibration [22] and the bands at 1540, 1440, and 1410 cm^{-1} are due to the bidentate coordination between titanium centers and the carboxylic groups of MAA [19]. The FT-IR spectra confirm that the coupling agent is successfully bonded with the titania nanoparticles, which is used to improve the compatibility of PMMA and inorganic moiety.

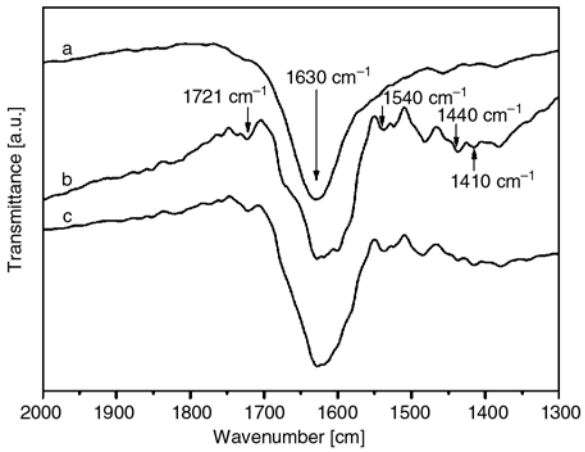

Figure 4. FTIR spectra of anatase titania sol modified with different content of MAA: (a) 0, (b) 10 and (c) 20 wt%

3.3. Glass transition temperatures of PMMA/titania composites

Figure 5 shows the DSC curves of the pure PMMA and the PMMA/titania composite materials at a heating rate of 10°C/min under nitrogen flow. All PMMA/titania composites obtained by photocatalytic polymerization exhibit an increased glass transition temperature (T_g) compared with pure PMMA (Figure 5a, T_g ~111°C), which indicates the restrained mobility of the polymer chains in the composites. This is attributed to the intercalated polymer chains within titania particles that prevents their segmental motion. Moreover, the higher T_g value of PMMA may also depend on the predominant syndiotacticity of the polymer prepared by photocatalytic polymerization [7]. The PMMA/titania composite obtained via photocatalytic polymerization by original anatase titania sol exhibits a glass transition temperature of 123°C (Figure 5b), while the PMMA-functionalized titania composites show elevated T_g values ranging from 127 to 129°C (Figure 5c and 5d). Therefore, the interfacial strength becomes stronger by the addition of MAA coupling agent. These DSC results indicate that the PMMA produced by photocatalytic polymerization has surely enhanced glass transition temperature. And moreover, the T_g values of PMMA composite materials is further increased by using MAA as coupling agent due to the formation of much stronger interactions between PMMA molecules and titania nanoparticles.

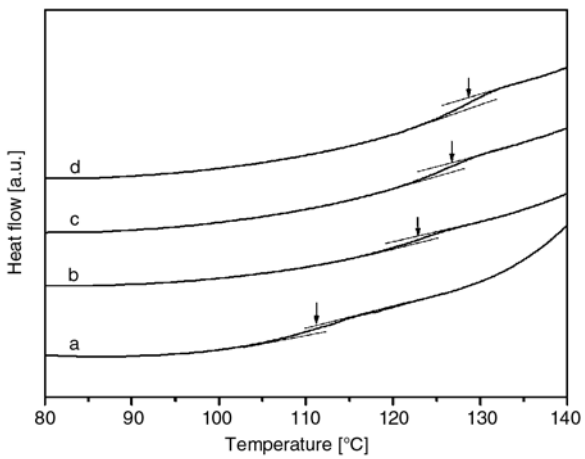

Figure 5. DSC curves of (a) pure PMMA and the composite materials with different MAA contents: (b) 0, (c) 10 and (d) 20 wt%

3.4. Thermal stabilities of PMMA/titania composites

The TGA curves of a pure PMMA and PMMA/titania composite materials with 10 wt% inorganic nanoparticles modified using different content of MAA as coupling agent are shown in Figure 6. In general, for the thermal decomposition of pure PMMA (Figure 6a), at least two degradation steps are clearly found and it starts decomposition at about 150°C. Previous works has proved that there are two steps in the thermo-oxidative degradation of PMMA. The first is due to the degradation of partially oxidized groups. The second is an attack of oxygen on the free radicals generated by random scission within the polymer chain [23, 24]. While there appears to be one step of weight loss for the composite materials starting at about 250°C and ending at about 400°C, which corresponds to the structural decomposition of the polymers. According to our previous work, the thermo-oxidative degradation mechanism of the PMMA/titania composite materials is such that titania may trap the free radical in the process of thermo-oxidative degradation of PMMA [25]. So evidently, the thermal decomposition of these composite materials shifts toward much higher temperature range than that of pure PMMA, which confirms the enhancement of thermal stability of PMMA by the introduction of titania nanoparticles. Furthermore, we clearly found that the $T_{0.5}$ ($T_{0.5}$ stands for the temperature at which 50% weight loss took place) of the

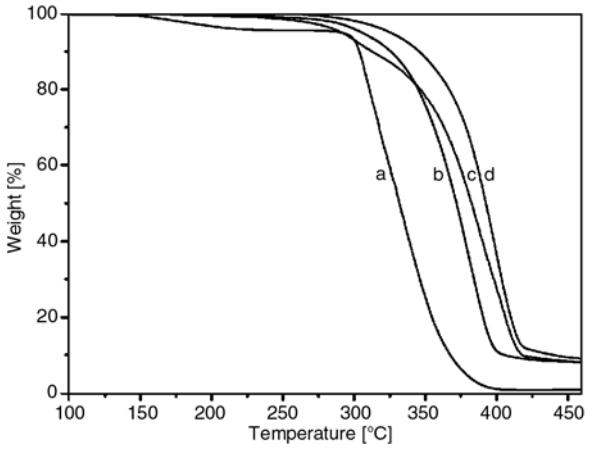

Figure 6. TGA curves of (a) pure PMMA and PMMA/titania composite materials with different content of MAA as coupling agent: (b) 0, (c) 10 and (d) 20 wt%

PMMA/titania composite materials with 0 (Figure 6b), 10 (Figure 6c) and 20wt % (Figure 6d) MAA as coupling agent are 372, 382 and 392°C respectively. So, when compared with PMMA/non-functional titania composites, the thermal properties of the as-synthesized PMMA/titania composite materials with MAA as coupling agent are enhanced. This implies that the use of MAA as coupling agent to modify the surface of anatase titania nanoparticles is feasible, and MAA can successfully improve the interfacial interactions between titania and PMMA matrix. Therefore, PMMA composite materials with enhanced thermal properties can be conveniently prepared by photocatalytic polymerization using the anatase titania sol.

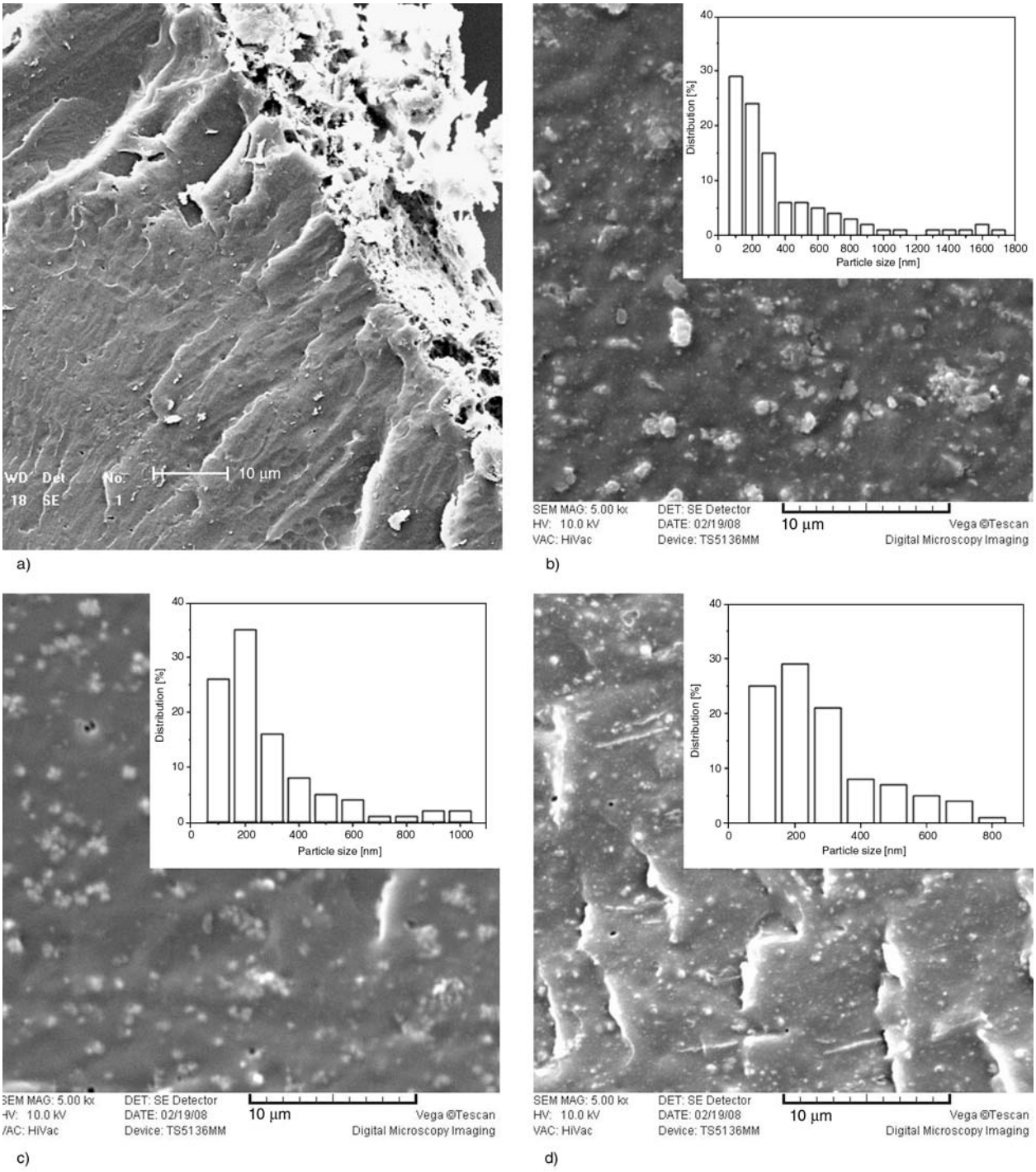

Figure 7. SEM images of the PMMA/titania composite films (a) prepared via subsequent addition of titania and *in situ* polymerization with different MAA contents: (b) 0, (c) 10 and (d) 20 wt%

3.5. Morphology of PMMA/titania composite films

SEM observations (Figure 7) were performed to examine the dispersion of the functionalized titania nanoparticles in the PMMA matrix. The fractured surface of the PMMA/titania composite film prepared via subsequent addition of the as-synthesized titania nanoparticles to PMMA solution was also characterized for comparison (Figure 7a). It is clearly found that the titania particles aggregate seriously and even deposit to the bottom of the PMMA composite film. The PMMA/titania composite films prepared via *in situ* polymerization have a much better distribution of inorganic particles as shown in Figure 7b–7d. For the better observation of dispersion of titania nanoparticles in PMMA matrix, the particle size and particle distribution of the PMMA/titania composites are also shown in Figure 7b–7d. The PMMA composite with non-functionalized titania indicates the obvious aggregation of inorganic particles and their distribution in the PMMA matrix is relatively poor (Figure 7b). The size of about 67% titania particles is less than 300 nm, while a portion of inorganic component is larger than 1 μm. To some extent, the aggregation of titania nanoparticles is restricted by the preparation method of *in situ* photocatalytic polymerization. The dispersion of the titania particles modified with 10 and 20 wt% MAA coupling agent (Figure 7c and 7d) is improved significantly in PMMA matrix. Above 75% titania particles are less than 300 nm in size and no inorganic particles larger than 1 μm is found. The PMMA/titania composite with 20 wt% MAA shows a better distribution of titania particles in the PMMA matrix than the one with 10 wt% MAA. This may result from the existence of stronger interfacial interactions between polymer matrices and functionalized inorganic particles. However, these SEM observations of PMMA/titania composite films obviously deviate from our expectation because of the disagreement between the size of original titania nanoparticles (~20 nm) and the inorganic nanoparticles in PMMA matrices (hundreds of nanometers) even after the surface modification. This may be clarified by the reaction process of the photocatalytic polymerization of the monomer. Our tentative proposed mechanism for the aggregation of anatase titania nanoparticles is as follows. The coupling agent MAA is initially absorbed onto the titania nanoparticles via the bidentate coordination. This leads to surface polymerization of MMA, which produces hydrophobic patches on the titania nanoparticles. In our reaction system, oil component (MMA) is excessive compared with its soluble amount in water and there must be the interfaces of oil/water during stirring. It has been proved that the energy of attachment of a spherical nanoparticle to the oil/water interface is related to the wettability of the nanoparticles and the nanoparticles with intermediate hydrophobicity benefit to stabilize oil drops in water [26]. Therefore, this leads to the movement of hydrophobic titania nanoparticles and their aggregation on the interfaces of oil/water to form the structure similar with Pickering emulsion.

4. Conclusions

A transparent anatase titania aqueous sol is successfully prepared by a facile nonhydrolytic sol-gel reaction. The PMMA/titania composites are prepared by the photocatalytic polymerization using functionalized anatase titania sol. According to the DSC, TGA and SEM results, introduction of MAA is beneficial to improve the interfacial interaction between PMMA matrices and titania nanoparticles. The glass transition temperatures and thermal stabilities of the PMMA/titania composites are increased. Compared with direct blending, the PMMA/titania composite films prepared via *in situ* polymerization show a much better distribution of titania particles. The partial aggregation of titania nanoparticles in PMMA composite films is caused by the enhancement of hydrophobicity of inorganic nanoparticles and formation of the structure like Pickering emulsion.

Acknowledgements

The authors gratefully acknowledge the financial support by the National Natural Science Foundation of China (NSFC) (No. 20704007) and Shanghai Nano Technology Project of China (No. 0625NM028).

References

[1] Guidi V., Carotta M. C., Ferroni M., Martinelli G., Paglialonga L., Comini E., Sberveglieri G.: Preparation of nanosized titania thick and thin films as gas-sensors. Sensors and Actuators B: Chemical, **57**, 197–200 (1999).
DOI: 10.1016/S0925-4005(99)00080-5

[2] Feldmann C.: Preparation of nanoscale pigment particles. Advanced Materials, **13**, 1301–1303 (2001).
DOI: 10.1002/1521-4095(200109)13:17<1301::AID-ADMA1301>3.0.CO;2-6

[3] Kamat P. V., Dimitrijević N. M.: Colloidal semiconductors as photocatalysts for solar energy conversion. Solar Energy, **44**, 83–98 (1990).
DOI: 10.1016/0038-092X(90)90070-S

[4] Grätzel M.: Photoelectrochemical cells. Nature, **414**, 338–344 (2001).
DOI: 10.1038/35104607

[5] Legrini O., Oliveros E., Braun A. M.: Photochemical processes for water treatment. Chemical Reviews, **93**, 671–698 (1993).
DOI: 10.1021/cr00018a003

[6] Linsebigler A. L., Lu G. Q., Yates J. T.: Photocatalysis on TiO_2 surfaces: Principles, mechanisms, and selected results. Chemical Reviews, **95**, 735–758 (1995).
DOI: 10.1021/cr00035a013

[7] Ni X. Y., Ye J., Dong C.: Kinetics studies of methyl methacrylate photopolymerization initiated by titanium dioxide semiconductor nanoparticles. Journal of Photochemistry and Photobiology A: Chemistry, **181**, 19–27 (2006).
DOI: 10.1016/j.jphotochem.2005.10.021

[8] Damm C., Völtzke D., Abicht H. P., Israel G.: Influence of the properties of TiO_2 particles on a photocatalytic acrylate polymerization. Journal of Photochemistry and Photobiology A: Chemistry, **174**, 171–179 (2005).
DOI: 10.1016/j.jphotochem.2005.03.006

[9] Damm C.: An acrylate polymerisation initiated by iron doped titanium dioxide. Journal of Photochemistry and Photobiology A: Chemistry, **181**, 297–305 (2006).
DOI: 10.1016/j.jphotochem.2005.12.011

[10] Yuwono A. H., Xue J. M., Wang J., Elim H. I., Ji W., Li Y., White T. J.: Transparent nanohybrids of nanocrystalline TiO_2 in PMMA with unique nonlinear optical behavior. Journal of Materials Chemistry, **13**, 1475–1479 (2003).
DOI: 10.1039/b211976e

[11] Yang Y. N., Wang P.: Preparation and characterizations of a new PS/TiO_2 hybrid membranes by sol-gel process. Polymer, **47**, 2683–2688 (2006).
DOI: 10.1016/j.polymer.2006.01.019

[12] Goto K., Tamura J., Shinzato S., Fujibayashi S., Hashimoto M., Kawashita M., Kokubo T., Nakamura T.: Bioactive bone cements containing nano-sized titania particles for use as bone substitutes. Biomaterials, **26**, 6496–6505 (2005).
DOI: 10.1016/j.biomaterials.2005.04.044

[13] Ma D. L., Hugener T. A., Siegel R. W., Christerson A., Mårtensson E., Önneby C., Schadler L. S.: Influence of nanoparticle surface modification on the electrical behaviour of polyethylene nanocomposites. Nanotechnology, **16**, 724–731 (2005).
DOI: 10.1088/0957-4484/16/6/016

[14] Yoshida K., Taira Y., Atsuta M.: Properties of opaque resin composite containing coated and silanized titanium dioxide. Journal of Dental Research, **80**, 864–868 (2001).
DOI: 10.1177/00220345010800030401

[15] Sidorenko A., Minko S., Gafijchuk G., Voronov S.: Radical polymerization initiated from a solid substrate. 3. grafting from the surface of an ultrafine powder. Macromolecules, **32**, 4539–4543 (1999).
DOI: 10.1021/ma981355u

[16] Erdem B., Sudol E. D., Dimonie V. L., El-Aasser M. S.: Encapsulation of inorganic particles via miniemulsion polymerization. I. Dispersion of titanium dioxide particles in organic media using OLOA 370 as stabilizer. Journal of Polymer Science Part A: Polymer Chemistry, **38**, 4419–4430 (2000).
DOI: 10.1002/1099-0518(20001215)38:24<4419::AID-POLA110>3.0.CO;2-X

[17] Erdem B., Sudol E. D., Dimonie V. L., El-Aasser M. S.: Encapsulation of inorganic particles via miniemulsion polymerization. II. Preparation and characterization of styrene miniemulsion droplets containing TiO_2 particles. Journal of Polymer Science Part A: Polymer Chemistry, **38**, 4431–4440 (2000).
DOI: 10.1002/1099-0518(20001215)38:24<4431::AID-POLA120>3.0.CO;2-Y

[18] Rong Y., Chen H-Z., Wu G., Wang M.: Preparation and characterization of titanium dioxide nanoparticle/polystyrene composites via radical polymerization. Materials Chemistry and Physics, **91**, 370–374 (2005).
DOI: 10.1016/j.matchemphys.2004.11.042

[19] Khaled S. M., Sui R. H., Charpentier P. A., Rizkalla A. S.: Synthesis of TiO_2-PMMA nanocomposite: Using methacrylic acid as a coupling agent. Langmuir, **23**, 3988–3995 (2007).
DOI: 10.1021/la062879n

[20] Yamazaki S., Nakamura N.: Photocatalytic reactivity of transparent titania sols prepared by peptization of titanium tetraisopropoxide. Journal of Photochemistry and Photobiology A: Chemistry, **193**, 65–71 (2008).
DOI: 10.1016/j.jphotochem.2007.06.008

[21] Hojjati B., Sui R. H., Charpentier P. A.: Synthesis of TiO_2/PAA nanocomposite by RAFT polymerization. Polymer, **48**, 5850–5858 (2007).
DOI: 10.1016/j.polymer.2007.07.054

[22] Rotzinger F. P., Kesselman-Truttmann J. M., Hug S. J., Shklover V., Gratzel M.: Structure and vibrational spectrum of formate and acetate adsorbed from aqueous solution onto the TiO_2 rutile (110) surface. Journal of Physical Chemistry B, **108**, 5004–5017 (2004).
DOI: 10.1021/jp0360974

[23] Manring L. E.: Thermal degradation of saturated poly(methyl methacrylate). Macromolecules, **21**, 528–530 (1988).
DOI: 10.1021/ma00180a046

[24] Chang T. C., Wang Y. T., Hong Y. S., Chiu Y. S.: Organic-inorganic hybrid materials. V. Dynamics and degradation of poly(methyl methacrylate) silica hybrids. Journal of Polymer Science Part A: Polymer Chemistry, **38**, 1972–1980 (2000).
DOI: 10.1002/(SICI)1099-0518(20000601)38:11<1972::AID-POLA60>3.0.CO;2-5

[25] Wang H. T., Meng S., Xu P., Zhong W., Du Q. G.: Effect of traces of inorganic content on thermal stability of poly(methyl methacrylate) nanocomposites. Polymer Engineering and Science, **47**, 302–307 (2007).
DOI: 10.1002/pen.20708

[26] Binks B. P., Lumsdon S. O.: Influence of particle wettability on the type and stability of surfactant-free emulsions. Langmuir, **16**, 8622–8631 (2000).
DOI: 10.1021/la000189s

eXPRESS Polymer Letters Vol.4, No.6 (2010) 382–395
Available online at www.expresspolymlett.com
DOI: 10.3144/expresspolymlett.2010.48

Controversial effects of fumed silica on the curing and thermomechanical properties of epoxy composites

J. Tarrío-Saavedra[1], J. López-Beceiro[2], S. Naya[2], C. Gracia[3], R. Artiaga[2]

[1]Department of Mathematics, EPS. University of A Coruna. Avda. Mendizábal s/n. 15403. Ferrol, Spain
[2]Department of Industrial Engineering II, EPS. University of A Coruna. Avda. Mendizábal s/n. 15403. Ferrol, Spain
[3]Thermal Analysis, Rheology and Microcalorimetry Applications. TA Instruments – Waters Cromatografía, S.A. Avda. Europa, 21 Parque Empresarial La Moraleja 28108. Alcobendas Madrid, Spain

Received 10 February 2010; accepted in revised form 24 April 2010

Abstract. The effect of fumed silica on the curing of a trimethylolpropane epoxy resin was investigated by thermal analysis methods like Differential Scanning Calorimetry (DSC), and Dynamic Mechanical Analysis (DMA). The fumed silica used here is a by-product of the silicon and ferrosilicon industry, consisting of micro and nanosized particles. Both the curing reaction and the properties of the obtained composites were affected by the filler content. Different trends were observed for filler contents above and below the 30 wt%. Up to 30 wt%, the behaviour can be explained as a predominantly agglomeration effect. For 30 wt% and higher filler contents, single particles seem to play a more important role.

Keywords: *polymer composites, thermal properties, thermosetting resins, fumed silica, viscoelastic properties*

1. Introduction

Although epoxy resins are widely used, their application is somewhat limited due to their brittleness derived from a highly cross-linked structure. The mechanical properties of epoxy resins can, however, be improved by incorporating inorganic particles [1]. It is well known that particle volume, shape, size, surface characteristics and particle dispersion within the matrix have an influence on the mechanical properties of the composites [2–5]. Specific surface area can promote stress transfer from matrix to nanoparticles and improve the Young's modulus of polymers to a higher extent than micro-fillers. Consequently, the required nanoparticle contents in polymer matrices are usually much lower as compared to micro-fillers [6]. The formation of organic-inorganic nanocomposites has shown the ability to provide simultaneous improvements in several properties including thermal stability, glass transition temperature levelling, dimensional stability, flame retardance, dielectric constant lowering and gas barrier and corrosion protection [6–15]. The degree of interaction between filler and polymer and thus the composite properties have been related to the filler-matrix interface. As defined in traditional composites, by Drzal *et al.* [16], and Schadler [17], the interfacial region is the region beginning at the point in the fiber at which the properties differ from those of the bulk filler and ending at the point in the matrix at which the properties become equal to those of the bulk matrix. The chemistry, polymer chain mobility, degree of cure, and crystallinity are likely to be altered in that region. Its thickness has been reported to be in the 2 to 50 nm range [17]. The interphase can have a significant effect, both positive and negative, on the mechanical properties of the composite: when the glass transition tempera-

*Corresponding author, e-mail: jtarrio@udc.es

ture, T_g, of the interphase is less than that of the matrix, the T_g of the composite decreases with filler addition. But, if the T_g of the interface is higher than that of the matrix, the T_g of composite will increase by increasing filler content [18]. Synergistic effects were found in the form of a further increase in wear resistance, stiffness, fracture toughness and tensile and impact strengths by mixing nano and microparticles [19–21]. Processing methods producing controlled particle size distribution, dispersion, and interfacial interactions would be advisable to obtain customized properties in new composites. Thus, the dispersion of nanoparticles in a polymer matrix has a significant impact on the properties of nanocomposites. Methods to improve the dispersion of nanoparticles into the matrix include, but are not limited to, mechanical mixing and ultrasonic dispersion [8, 10], surface modification of nanoparticles [10, 22, 23] and sol-gel process [24, 25].

On other hand, thermal analysis techniques are usually employed in the study of thermal stability, curing reactions, glass transition and thermomechanical properties. Thermal stability of polymers and composites is usually evaluated by thermo-gravimetric analysis (TG) [10, 26]. Differential scanning calorimetry (DSC) has been used to study the degree of curing of thermosets by calculating the heat of cure from the area enclosed in the exothermal peak [10, 18, 27]. In non-homogeneous materials, like composites, the reaction heat should be divided by the mass of resin. Sealed crucibles are recommended in order to prevent volatilization, which would appreciably affect the measured heat [18]. The experiments should start at temperatures low enough in order to prevent any curing reaction from taking place before the data acquisition starts. In standard DSC, a heating rate of 10°C min^{-1} is usually recommended to promote an adequate balance between resolution and sensitivity [18]. Thermal glass transition refers to the immobilization or freezing-in at the transition from the liquid to the glassy state in cooling experiments [28]. The glass transition temperature is usually defined on cooling from the equilibrium liquid to the glassy state, and is a function of cooling rate [29]. Therefore the T_g is usually measured by standard DSC at 10°C min^{-1} cooling rate. Modulated temperature DSC (MTDSC) is a refinement of the standard DSC allowing for separation of overlapping reversing and non reversing events, such as glass transition and enthalpy recovery [18, 30, 31] or post-cure processes. Dynamic glass transition is used to describe the increasing relaxation time in the stable or metastable equilibrium state [28]. It is usually determined in heating ramp by DSC or dynamic mechanical analysis (DMA). For frequencies in the Hertz range and higher, the temperature range is located above the glass transition temperature in thermodynamic (metastable) equilibrium [32]. DMA allows for evaluation of viscoelastic properties in polymers along a broad temperature range. Through the analysis of the damping factor, this technique provides one of the most reliable methods for measuring the dynamic glass transition temperature [33, 34].

There is some controversy about the T_g determination by DSC on heating because, in most cases, an endothermic hysteresis peak is superimposed on the glass transition. Measurement of T_g on cooling is recommended when using standard [29, 35]. Differences between T_g measured by DSC on cooling and dynamic T_g measured by DMA are due to the frequency effect on T_g values. T_g values obtained from 1 Hz DMA data for E'' or tanδ peak are always a few degrees higher than DSC T_g values obtained at 10–20°C min^{-1} heating rates [35].

In this work, fumed silica-epoxy mixtures were prepared and characterized by thermal analysis methods. The properties of the non conventional epoxy resin, based on trimethylolpropane, make it particularly suitable for the manufacture of composites. Synthetic silicon dioxide (silica) can be produced either by precipitation or by apyrogenic (thermal) process. According to the method of production, synthetic silicon dioxides can be classified into two groups: precipitated and pyrogenic silica [36]. The fumed silica used here was obtained as a by-product of the silicon production in the top of large electrical melting furnaces, which is a non conventional production. Hence, the particle size and the purity of the fumed silica are variable, reflecting the furnace operation at the time it was collected. In any case, the silica weight proportion is greater than 95%. According to Schadler, three dimensional nanofillers are relatively equally-axed particles, with a length lower than 100 nm in their largest dimension [17]. Hence, the fumed silica used in this work has its specific particle size distribution, including micro and nanoparticles. This makes it different from other micro or nanosized

silica powders, and therefore, combined effects of both are expected.

The aim of this work is to evaluate the effects of fumed silica on both the curing and the viscoelastic properties of the resulting composites. Possible relations between the effect on the curing and the composite properties were considered and a statistical study was performed to this aim. Therefore, each experiment was replicated and several design of experiments (DOE) tests were applied: ANOVA table, F and Tukey.

2. Experimental

2.1. Materials

A two component epoxy system was used. It consisted of a diglicidyl ether of trimethylolpropane based resin, Triepox GA, from Gairesa (Valdoviño, Spain) and 1,3-benzenedimethanamine 99% pure, from Aldrich (St. Louis, MO, USA), as curing agent. The 1,3-benzenedimethanamine is an aromatic amine hardener. Triepox GA is a highly thyxotropic resin with low density and curing capability at room temperature on its own, without either plasticizers or additives [37–39]. The epoxy resin was prepared by reaction of epichlorydrin with trimethylolpropane. The curing reaction scheme is presented in Figure 1 [37–39].

The fumed silica was provided by Ferroatlántica I+D (Arteixo, Spain). It was obtained as a by-product of the silicon production in electrical melting furnaces. This process involves the reduction of high purity quartz, at temperatures above 1800°C. The silica fume is formed when the SiO gas, resulting from the reduction of quartz, is mixed with oxygen at the top of the furnace producing spherical silica particles. It is a fine powder with colour ranging from almost black to slightly-off white, depending on its carbon content. Its mean particle size is 0.15 μm and 41.9% of the particles have a diameter below 0.2 μm, as shown in Table 1. The SediGraph method was used for determining the mass distribution of particles as a function of particle size. This method has proved to be useful in many applications since 1967. Particle sizes were calculated from measurements of settling velocity and mass fraction, which was determined by relative absorption of low-energy X-ray [40]. The values obtained through surface area analysis typically fall about 20 $m^2 \cdot g^{-1}$. Chemically, the fumed silica consists of amorphous SiO_2 of variable purity. Some physical properties and chemical composition are shown in Table 2.

Table 1. Particle size distribution of the fumed silica

Diameter [μm]	Mass [%]
100–50	1.2
50–20	2.0
20–10	0.2
10–5	0.5
5–2	1.4
2–1	1.5
1–0.5	8.3
0.5–0.2	43.0
<0.2	41.9

Table 2. Some physical properties and chemical composition of the fumed silica

Moisture 110°C	0.50%
Loss on calcination at 1000°C	2.78%
Real density	2.26 $g \cdot cm^{-3}$
Apparent density	0.66 $g \cdot cm^{-3}$
SiO_2	+95%
CaO	0.68%
MgO	0.22%
Na_2O	0.10%
K_2O	0.22%
Cl	0.006%
SO_4	0.076%

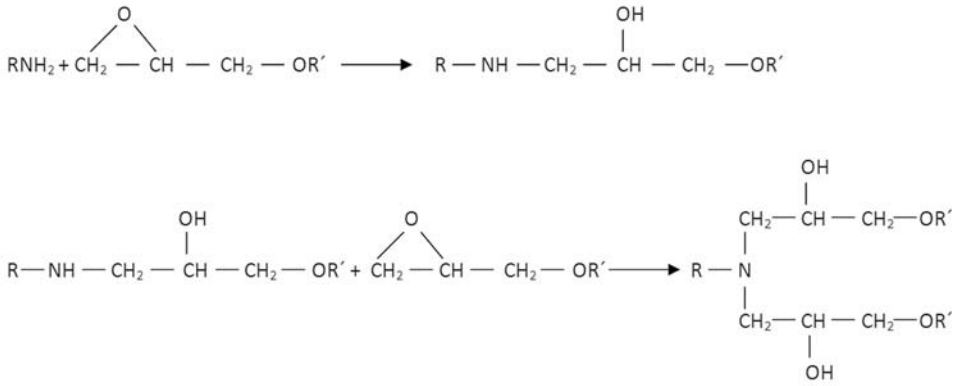

Figure 1. Chemical reaction scheme of the curing of Triepox GA with amine hardeners

2.2. Sample preparation

Filler-resin mixtures for curing studies:

For the curing study, samples of the resin containing 0, 10, 20, 30, 40 and 50 wt% of fumed silica were prepared, with the aim of measuring the heat of reaction by DSC. The resin and the curing agent were poured at stoichiometric proportions and manually stirred for 2 minutes. Then, the adequate amount of silica was added and mixed again for 5 minutes. In order to prevent any volatilization process, the samples were encapsulated in hermetic aluminium DSC crucibles. The mass of the samples was adjusted so that the resin content was close to 3.18 mg, independently of the filler content.

Cured samples:

Composite samples for DMA tests were prepared with filler contents of 5, 10, 20, 30, 40, 50 and 60 wt% of fumed silica. Both the epoxy resin and the hardener were mixed in stoichiometric proportions. Resin and silica mixtures were stirred for 15 minutes in order to obtain a uniform distribution. Then, a sonication treatment was applied for 5 minutes at room temperature to disperse the filler agglomerates. The composite paste was poured into a silicone mould whose cavity dimensions were 0.8×4×30 mm. This resin was reported to cure at room temperature having a T_g about 90°C. In this work, the samples were cured at room temperature for 24 hours and post-cured in an oven at 90°C for 2 hours. Further MDSC analysis showed the adequacy of this procedure. The specimens were finally cut, by scissors, to a length of 10 mm, so that their lengths do not protrude in excess the DMA fixtures. For the DSC and MTDSC-glass transition tests and for the TG stability study, cured samples were cut from DMA samples. The sample mass was adjusted so that each sample contained about 3 mg of resin, independently of the filler content.

2.3. Characterization methods

The DSC experiments were performed on a TA Instruments (headquartered in New Castle, DE, USA) MDSC Q-1000 attached to a refrigerating cooling system. This instrument can be operated in both modulated and standard modes. The following calibrations were performed, according to manufacturer recommended procedures: T_{zero}, enthalpy constant, temperature and modulated heat capacity. A range of temperature from –20 to 300°C was chosen, as per recommendations from the literature [18]. Sapphire standard and crimped aluminum crucibles were used for heat capacity calibration in modulated conditions.

The curing experiments were performed by standard DSC using hermetic aluminium crucibles to prevent hardener volatilization. A 10°C·min^{-1} heating ramp was applied from –20 to 220°C.

The T_g of the cured samples was also determined by DSC in standard mode, although in this case a 10°C·min^{-1} cooling ramp from 110 to 0°C was used. A previous thermal stability study of these composites [26] was considered in order to determine a range of temperature where the material does not decompose.

DSC was operated in modulated mode in order to separate the reversing Cp from non reversing phenomena such as enthalpic recovery, residual cure and possible degradation processes taking place in cured samples. The thermal program consisted of a 5°C·min^{-1} average heating ramp from –20 to 200°C. The modulation amplitude was 1.6°C and the period 60 s.

The viscoelastic properties of the cured composites were evaluated by DMA on a DMTA IV instrument manufactured by the company Rheometric Scientific (Piscataway, NJ, USA). Calibration was performed as per manufacturer recommendations included in the Rheometric Orchestrator™ software. The tests were conducted in tensile mode. The samples were about 0.8 mm thick and 4 mm width. A fixture gap of 10 mm was used. A strain sweep test was performed at room temperature in order to find experimental conditions in the viscoelastic linear region for subsequent experiments. This was done by varying the strain amplitude while keeping the frequency at 1 Hz. A strain amplitude of 0.005% and 1 Hz frequency were chosen. A constant heating ramp of 2°C·min^{-1} was applied in all the experiments.

An additional TGA experiment was performed with a cured composite sample in order to verify some possible degradation process observed in the MTDSC experiments. The test was performed on a STA 1500 Rheometric Scientific thermo balance (Piscataway, NJ, USA). A heating ramp of 10°C·min^{-1} was applied in the range from 20 to

600°C, at a rate of 50 ml·min^{-1} of N_2. Upon reaching 600°C, the purge was changed to air and isothermal condition was kept for 4 minutes.

Particle distribution and dispersion in the matrix were studied by scanning electron microscopy. DMA specimens were previously broken manually. The fracture surface was coated with a thin layer of gold in a sputtering equipment BALTEC SCD 004 and then analyzed in a scanning electron microscope JSM-6400 (JEOL, Tokyo, Japan) equipped with a system of chemical microanalysis by energy dispersive X-ray Oxford INCA ENERGY 200 (Oxford Instruments, Abingdon, Oxfordshire, UK). It has been performed a TEM analysis for studying the distribution of particle sizes and dispersion with a greater magnification. TEM analysis has been realized in a transmission electron microscope JEM-1010 (JEOL, Tokyo, Japan). The sections observed under the microscope (with a thickness of about 80nm) were obtained in a Reichert ultramicrotome Ultracut E (Reichert, Depew, NY, USA).

2.4. Experimental design

An experimental design was applied to evaluate the filler content effects on the heat of curing of the fresh mixtures and the T_g of the cured samples. A one-way design was chosen to test for differences in the response among the independent groups. The silica content was the chosen factor or independent variable. A fixed-effects model of analysis of variance (ANOVA) was applied. The value of the explanatory variable was varied in order to see how the response variable changes, and to test if there are testing significant differences in the response. It also allows for estimation of the variation ranges of the responses produced by the filler content. The responses considered were the heat of reaction, the T_g, measured by DSC in cooling, and the dynamic T_g, determined by DSC in heating. The following levels of filler content were considered for the heat of curing study: 0, 10, 20, 30, 40 and 50 wt%. The 5 wt% level was also included for the T_g study in order to increase the resolution of the analysis in the low filler content range. All the experiments were replicated in order to estimate the variability.

3. Results and discussion

3.1. Evaluation of the curing by DSC

Figure 2 plots an overlay of the DSC curves obtained from the curing experiments. A broad exotherm corresponding to the curing reaction can be observed in each curve. The curing enthalpy, ΔH_{RXN}, was calculated by dividing the area of the exotherm peak by the resin content of the sample. An ANOVA test was performed to discern if the silica content factor produces significant differences in the response, ΔH_{RXN}. The Tukey test was applied to determine what particular proportions of silica produce significant differences in the response respect to the other levels of silica [41–43]. This test can only be applied when observations are independent, variances on the response are equal across groups and the response or dependent variable is normally distributed in each group. Normality was tested by the Shapiro Wilk test (P-value = 0.16 > 0.05) [44], homoscedasticity by the Bartlett one (P-values = 0.769 > 0.05) [45] and independence by the Durbin-Watson test (P-value = 0.966 > 0.05) [46, 47]. The ANOVA and F test have shown that there are significant differences in ΔH_{RXN} when varying the amount of silica (P-value = $6.873 \cdot 10^{-11} < 0.05$) assuming a significance level of 0.05. Therefore the ΔH_{RXN} response actually depends on the silica content.

Moreover, the Tukey test was applied to find out which specific means of ΔH_{RXN}, at each silica level, are different from the others. The results (P-values < 0.05), indicate that the six groups are significantly

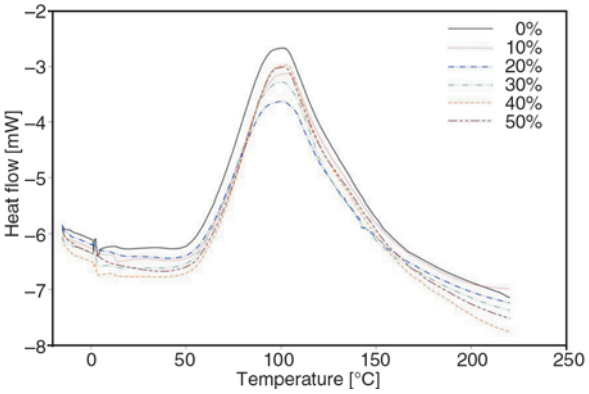

Figure 2. DSC curves obtained from the curing experiments with different wt% of fumed silica

Table 3. Results obtained from the DSC curing experiments

Silica content [wt%]	Sample mass [mg]	ΔH_{RXN} [J·g^{-1}]
0	3.18	440.1±0.1
10	3.90	429.5±1.3
20	3.95	379.6±1.3
30	4.50	436.1±0.1
40	5.52	491.8±0.7
50	6.28	496.7±0.7

different. Then, the ΔH_{RXN} averaged values presented in Table 3 are significantly different.

It can be observed in Table 3 that ΔH_{RXN} increases with the silica content for contents above the 30 wt%, which indicates that the resin may react with the filler. The opposite effect can be observed for silica contents below the 30 wt%, indicating an incomplete cross linking due to the presence of particles. It suggests that agglomerates of particles are formed and these agglomerates could absorb part of the hardener. Thus, the stoichometric balance would be distorted resulting in an incomplete cure.

3.2. Morphological study of cured composites

A morphological study of composite samples with 5, 30 and 40 wt% of filler was performed by SEM and TEM. Few areas containing agglomerates and single particles could be found in the 5 wt% sample. The first two micrographs in Figure 3 show two of these areas. The first SEM micrograph shows an uncovered agglomerate surrounded by smaller agglomerates, which are covered by the polymer matrix. It can be observed that the agglomerate seems to be mostly composed of nanosized particles, although a particle of about one μm is located at its center. The shape and size of the agglomerates is variable. The second SEM micrograph shows some single microparticles, which are spherical in shape, although of very different sizes. It was considered convenient to complete the mor-

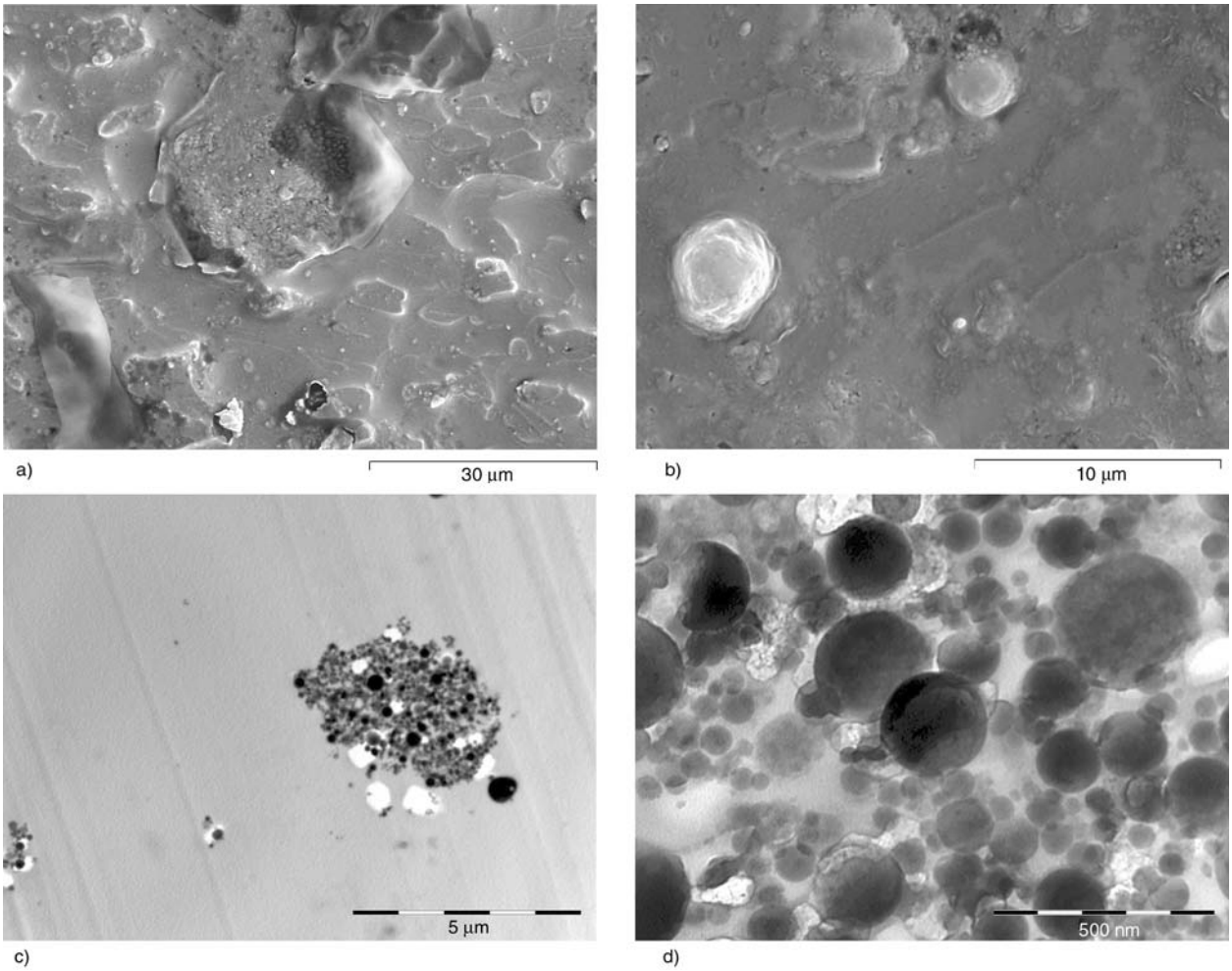

Figure 3. SEM micrographs obtained from the fracture surface (a, b) and TEM micrographs (c, d) of a 5 wt% filler sample

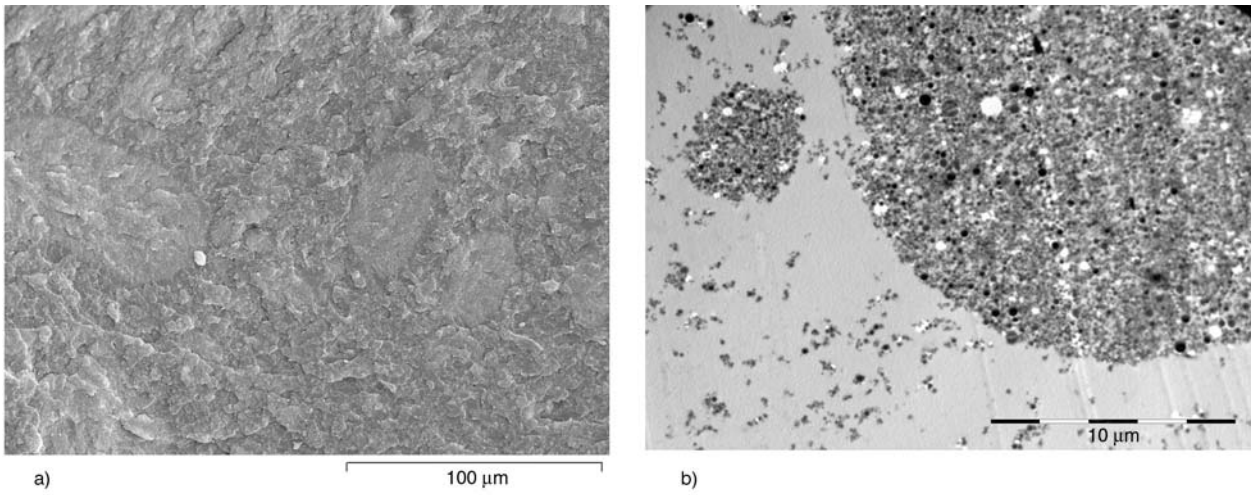

Figure 4. SEM micrographs obtained from the fracture surface of a 30 wt% sample (a) and TEM micrograph (b)

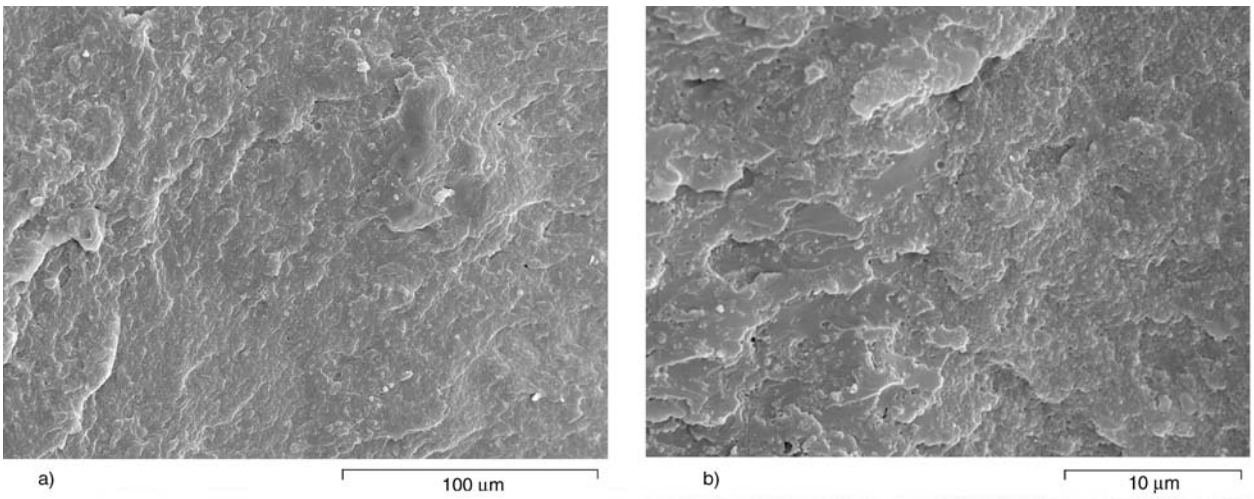

Figure 5. SEM micrographs obtained from a 40 wt% sample (a, b)

phological study by TEM to confirm the SEM observations. So, the third and fourth micrographs in Figure 3 show that the agglomerates are mostly composed of nanosized particles. The first micrograph in Figure 4, obtained by SEM, shows one region on the fracture surface, belonging to the 30 wt% sample. Some elliptical regions can be observed. The energy dispersive X-ray (EDX) analysis of these regions indicates high silica content. In contrast, the surrounding regions present very low silica content. It indicated that the fumed silica particles are not uniformly dispersed but agglomerated in the elliptical regions. TEM analysis supports and complements SEM analysis in the second micrograph in Figure 4. Moreover, it shows that the agglomerates grow when compared with those in the 5 wt% sample (Figure 3, third micrograph). The micrographs in Figure 5, obtained by SEM, show the fracture surface of a 40 wt% sample, at two different magnifications. The elliptical formations disappeared and no agglomerates were found, indicating that the filler is well distributed over the entire sample. Single particles can be observed in the second picture. Figure 6 shows a SEM micrograph corresponding to a 40 wt% sample and its corresponding silica particle dispersion map, obtained by X-ray. Silica particles are well dispersed although non-uniformly distributed over the region. That non-uniformity was only observed at the low scale. Morphologically, two regions can be distinguished. The one corresponding to the higher silica content is rough, with no apparent plastic deformation, indicating a brittle fracture. On the contrary, the lower filler content region presents some plastic deformation, indicating a somewhat ductile fracture.

These morphological results match the hypothesis drew from the curing study, so that the agglomer-

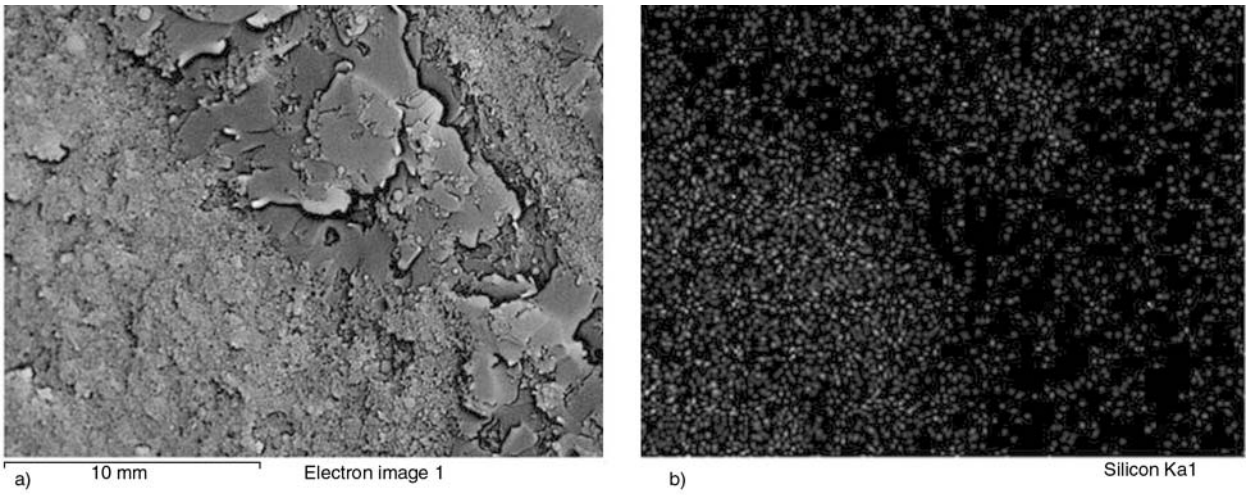

Figure 6. SEM micrograph corresponding to a region in a sample with an amount of 40 wt% of silica (a) and its silica particles dispersion map, obtained by X-ray (b)

ates would act as hardener captors and the well dispersed particles would react with the resin.

3.3. Effects on the properties of cured composites

Figure 7 shows the non-reversing heat flow plots obtained by MTDSC from the cured samples. An exotherm, starting at about 115°C, indicates the beginning of sample degradation, what was confirmed by TGA, as it can be observed in Figure 8. But there is no trace of residual cure. It means that the curing and post curing treatments were enough to fulfil the cure completion. Figure 8 plots the TGA curves obtained in N_2 atmosphere, with change to air at 600°C. A small increase of the sample mass is observed at the beginning of the experiment. It was reported that this phenomenon can be attributed to a buoyancy effect due to a decrease of the atmosphere density as the temperature raises

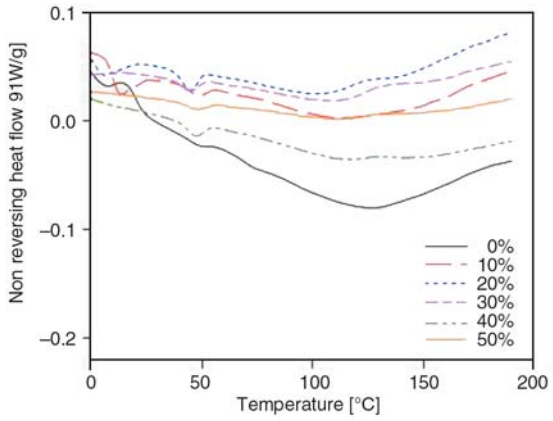

Figure 7. Specific non reversing heat flow curves obtained with the different samples

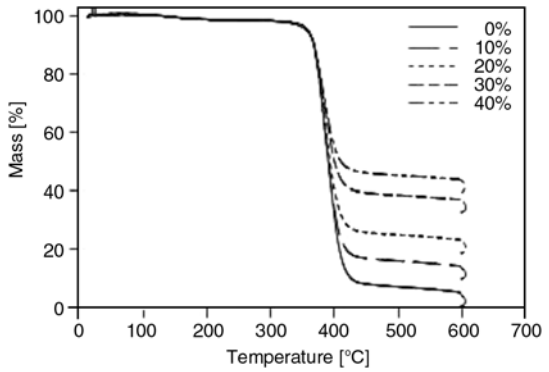

Figure 8. TGA curves obtained from the neat epoxy thermoset and composites with different fumed silica contents in N_2 atmosphere. Upon reaching 600°C, isothermal condition was established and the purge was changed to air.

[35]. Nevertheless, considering that this phenomenon was not observed in other experiments, performed under the same experimental conditions but with different materials, the buoyancy effect does not seem to be responsible of that mass gain. Thus, it indicates that the sample absorbs nitrogen from the purge flow. There is also a mass loss in the range from 100 to 200°C. It is higher than the increase due to N_2 absorption, and indicates a decomposition process of the weakest structure of the sample, which extends up to about 300°C, overlapping with the main degradation process. The residue obtained after the isothermal stage in air at 600°C corresponds to the filler content, indicating a complete combustion of the char.

Figure 9 shows the storage modulus, E', loss modulus, E'', and damping factor, tanδ, obtained in a DMA temperature ramp from a cured sample. The

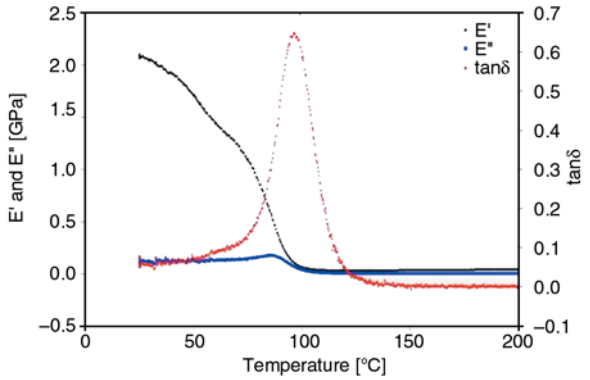

Figure 9. E', E'' and tanδ curves obtained by DMA from the neat resin sample

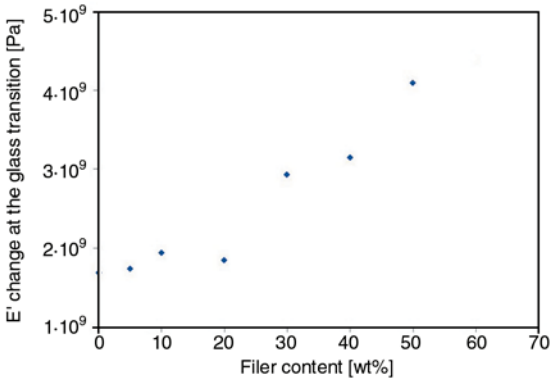

Figure 11. Change of E' observed for different filler contents in the temperature range of 50 to 150°C

E' decrease observed in a range from 50 to 100°C correspond to the glass transition relaxation of the polymer. The T_g is also evidenced by a small peak of E'' and by a well defined peak of tanδ. Thus, the maximum peak value of tanδ was the chosen criterion to compare the T_g values obtained by DMA. It can be observed in Figure 10 that, in all cases, E' decreases monotonically with any temperature increment, at temperatures below the T_g. This can be attributed in part to the softening of the polymer matrix, which is more apparent in the proximity of T_g, as it can be observed on the unfilled curve, and in part, to the difference between the coefficients of thermal expansion of the matrix and the fumed silica, inducing relaxations in the polymer phase, as was reported in other studies [6, 8, 10]. Above the T_g, E' increases with the temperature, indicating a stiffening process of the matrix. It is probably due to an incipient degradative process, which is consistent with the TGA behavior observed at temperatures below 300°C. The slope of the E' curve does not change appreciably, which is in line with existing studies [8].

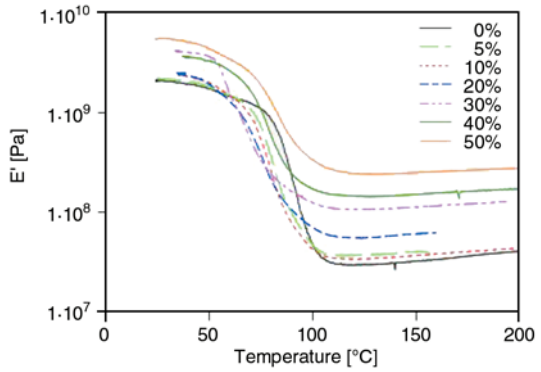

Figure 10. E' plots obtained from the neat resin and composites with different fumed silica contents

Figure 10 also shows a stiffening effect of the fumed silica addition, which seems to be more noticeable above the glass transition temperature. Nevertheless, it is only apparent, due to the use of a semi-logarithmic scale. In Figure 11, the E' change in the temperature range of 50 to 150°C is plotted vs. the filler content. It can be observed that the E' drop at the glass transition increases very slightly up to the 20 wt%. Above the 30 wt%, an important increasing trend with the filler content is observed. Since the glass transition is associated to the polymer phase, the opposite behavior could be, in principle, expected. Nevertheless, it can be understood as an indication that the silica induces some changes in the polymer matrix so that the higher the filler content the higher the fraction of the matrix undergoing some kind of relaxation at the glass transition. Particularly, the change of trend observed at the 30 wt% can be easily related to the dispersion of nanoparticle elliptical agglomerates, which was described in the morphological study part. Any increase of the filler amount, below the 20 wt%, would mainly produce an increase of the agglomerate size, providing little contribution to an effective filler-polymer surface increment. Nevertheless, in the range from 30 to 40 wt%, the agglomerates are destroyed, due to the higher viscosity and thus to the higher shear stresses generated in the stirring sample preparation stage. Any increment in the filler content, above the 30 wt%, will produce a neat increment of the amount of filler-polymer interphase.

A plasticizing effect of the filler can be observed in Figure 12, where all the filled samples present a shifting of the tanδ peaks to lower temperatures with respect to the neat resin sample, according to

Table 4. T_g values obtained by DSC on cooling and DMA on heating. The area and normalized area of the tanδ peaks obtained by DMA are also shown.

Silica content [wt%]	T_g DSC (cooling) [°C]	T_g DMA (heating) [°C]	tanδ peak area [s]	Normalized tanδ peak area [s]
0	77.6±0.6	96.7	430.8	430.8
5	66.7±1.0	83.7	413.9	435.7
10	66.9±1.3	81.8	396.0	440.0
20	63.3±1.1	77.4	363.2	454.0
30	62.1±0.6	70.6	324.0	462.9
40	65.0±0.7	81.6	319.9	533.1
50	68.2±1.3	85.8	280.9	561.8

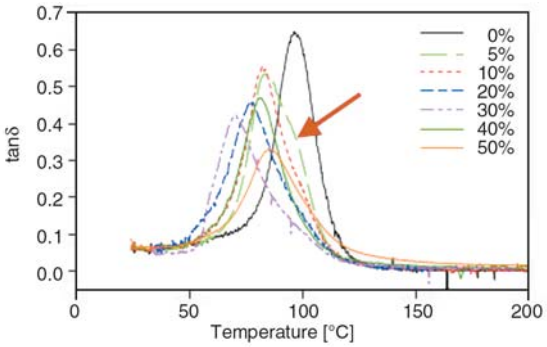

Figure 12. tanδ curves obtained from composites with different filler contents. A shoulder on the right side of tanδ peak is pointed out by an arrow.

Huang and Lee study [10]. Another effect of the filler is a broadening of the tanδ peaks. This indicates higher heterogeneity of the composites crosslinked structure [35]. In Table 4, it can be observed that the area of the peaks decreases when the silica content is increased. Since the glass transition is a relaxation process of the polymer, the lower the polymer content, the lower the magnitude of the glass transition change. A shoulder can be observed on the right side of the tanδ peaks of the composites. It is more evident on the 5 wt% curve. Reed [48] suggested that the existence of a shoulder can be attributed to the particle-resin interface, which is different from the polymer matrix [18]. In this case, the composites shoulder is located at the T_g of the unfilled material. It would indicate that the shoulder represents the glass transition of the polymer segments not affected by the filler, while the interface material has a lower T_g. At the filler contents considered in this work, it is clear that the magnitude of the interface glass transition is higher than that corresponding to the fraction of the matrix free from the filler effect. Nevertheless, a different relation should be expected for filler contents well below the 5 wt%. Table 4 also shows the normalized values of the tanδ peak areas, which were obtained by division of the areas by the polymer fraction. The normalized tanδ area increases with the filler content up to the 50 wt%. It can be explained as an effect of the effective polymer-filler interfacial area, which increases with the filler content. The maximum difference is observed in the 30 to 40 wt% range, which corresponds to the agglomerates destruction and thus, to a dramatic increase of the interface area.

Table 4 shows the T_g values obtained by DSC and DMA. The DSC T_g values were calculated from the heat flow curves shown in Figure 13, which were performed in standard DSC mode, in cooling, according to recommendations from the literature [35], while the DMA values were taken at the maximum of tanδ peak [35] from heating ramp experiments. Under hypothesis previously explained, the DMA T_g values of the composites are mainly contributed by the interface glass transition, while in the case of the neat thermoset such interface does not exist. The T_g values obtained by DSC are always lower than the corresponding ones obtained by DMA. This difference comes from the fact that these techniques measure different properties and the DMA results are affected by the frequency effect.

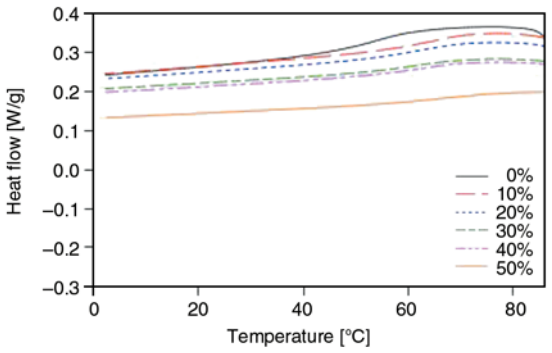

Figure 13. Specific heat flow curves obtained from the different composites by DSC operated in standard cooling ramp

A statistical study was done in order to determine the reliability of these results. Therefore, each experiment has been replicated. ANOVA was applied to discern whether the silica content produces significant differences in the response. In order to verify the model hypothesis, normality was tested by the Shapiro Wilk test (P-value = 0.03 <0.05) [44], homoscedasticity by Bartlett (P-values = 0.9995 > 0.05) [45] and independence by Durbin-Watson (P-value = 0.997 > 0.05) [46, 47]. Although, normality is in the limit of significance, ANOVA is robust even if the dependent variable data are approximately normally distributed [41]. So, the ANOVA and the F test revealed that there are significant differences in T_g when varying the amount of silica (P-value = $1.419 \cdot 10^{-5} < 0.05$). Moreover, the coefficient of determination (R^2 = 0.9797) indicates that mean differences of the amount of silica explain the T_g variability. The result from the Tukey test, Table 5, revealed that there are four groups with significantly different T_g. The neat epoxy material is statistically different from the rest of the samples. The 30 wt% composite is also significantly different from the rest of the samples. The increase of T_g observed in the 40 and 50 wt% samples and the difference between the 40 and 50 wt% are also significant.

Both DMA and DSC T_g values indicate that, in general, although the T_g values measured in the composites were always lower than that obtained from the unfilled sample, opposite effects exist below and above 30 wt% of filler. While additions of filler up to 30 wt% produce a continuous decrease of the T_g, increments from 30 to 50 wt% result in an increase of T_g. It can be again related to the dispersion of nanoparticle elliptical agglomerates, which was clearly observed in the 30–40 wt% filler content range. In this case, increments of the filler content, below the 20 wt%, would mainly produce an increase of the agglomerates amount and size, providing little contribution to an effective filler-polymer surface increment. These agglomerates would act as small bubbles, providing a plasticizing effect. Nevertheless, in the range from the 30 to the 40 wt%, the agglomerates are destroyed, and any increment of the filler content, above the 30 wt%, will produce a neat increment of the filler-polymer interfacial area resulting in an increase of T_g. Increments above the 50 wt% seem to produce a slight decrease of T_g, indicating some discontinuity of the polymer matrix, which would not be sufficient to surround all the particles and agglomerates. The fact that the T_g of the high filler content composites is still lower than the one of the neat resin indicates a plasticizing effect of the well dispersed particles, which is much lower than the plasticization produced by the agglomerates.

Table 5. Silica content groups resulting to be different according to the Tukey analysis of the T_g values

Silica content [wt%]	Significance level = 0.05			
	1	2	3	4
30	62.1			
20	63.3	63.3		
40	65.0	65.0	65.0	
5		66.7	66.7	
10		66.9	66.9	
50			68.2	
0				77.6
P-values	0.152	0.058	0.090	1.000

4. Conclusions

The curing study suggests that the agglomerates would act as hardener captors and the well dispersed particles would react with the resin. It matches perfectly with the morphological results.

The morphological study confirmed that the particles tend to agglomerate when its content is lower than the 30 wt%. Higher filler content produce well dispersed composites. It is related to the viscosity of the mixture and the shear stresses generated in the preparation of the mixtures. According to the micrographs, the agglomerates appear to be mostly composed of nanoparticles.

Two glass transition processes were identified, although not resolved, by DMA in the composites. One seems to correspond to the polymer fraction not interacting with the filler and occurs at the same temperature that the glass transition of the pristine thermoset. The other seems to correspond to the interface. The latter is predominant at the 5 wt% and higher filler contents and thus, it is the responsible of the plasticization effects identified by the glass transition temperature studies.

The glass transition temperature studies revealed two plasticization effects of the fumed silica. Both effects are reflected in the interface glass transition, which predominates over the neat polymer one at the 5 wt% and higher filler contents. One plasticizing effect is produced by the particle agglomerates and the other by the well dispersed particles. The

plasticizing effect of the agglomerates is much stronger than the produced by the dispersed particles. The agglomerates effect predominates at filler contents below the 30 wt% while the dispersed particles effect is predominant at higher filler contents. DSC results suggest that a slight degradation process starts at 115°C independently of the filler content. This is in line with a stiffening effect of the temperature observed by DMA. Finally, this degradation process was confirmed by TG.

Acknowledgements

This work was partially funded by the Spanish Ministerio de Educación y Ciencia MTM2008-00166. Thanks to Antonio Pérez from Ferroatlántica and Senén Paz from Gairesa for their comments about fumed silica and epoxy resin.

References

[1] Harsch M., Karger-Kocsis J., Holst M.: Influence of fillers and additives on the cure kinetics of an epoxy/anhydride resin. European Polymer Journal, **43**, 1168–1178 (2007).
DOI: 10.1016/j.eurpolymj.2007.01.025

[2] Lee A., Lichtenhan J. D.: Thermal and viscoelastic property of epoxy-clay and hybrid inorganic-organic epoxy nanocomposites. Journal of Applied Polymer Science, **73**, 1993–2001 (1999).
DOI: 10.1002/(SICI)1097-4628(19990906)73:10<1993::AID-APP18>3.0.CO;2-Q

[3] Hsiue G-H., Chen J-K., Liu Y-L.: Synthesis and characterization of nanocomposite of polyimide-silica hybrid from nonaqueous sol-gel process. Journal of Applied Polymer Science, **76**, 1609–1618 (2000).
DOI: 10.1002/(SICI)1097-4628(20000613)76:11<1609::AID-APP1>3.0.CO;2-W

[4] Mehta S., Mirabella F. M., Rufener K., Bafna A.: Thermoplastic olefin/clay nanocomposites: Morphology and mechanical properties. Journal of Applied Polymer Science, **92**, 928–936 (2004).
DOI: 10.1002/app.13693

[5] Fu S-Y., Feng X-Q., Lauke B., Mai Y-W.: Effects of particle size, particle/matrix interface adhesion and particle loading on mechanical properties of particulate-polymer composites. Composites Part B: Engineering, **39**, 933–961 (2008).
DOI: 10.1016/j.compositesb.2008.01.002

[6] Zhang H., Zhang Z., Friedrich K., Eger C.: Property improvements of in situ epoxy nanocomposites with reduced interparticle distance at high nanosilica content. Acta Materialia, **54**, 1833–1842 (2006).
DOI: 10.1016/j.actamat.2005.12.009

[7] Liu Y-L., Wei W-L., Hsu K-Y., Ho W-H.: Thermal stability of epoxy-silica hybrid materials by thermogravimetric analysis. Thermochimica Acta, **412**, 139–147 (2004).
DOI: 10.1016/j.tca.2003.09.004

[8] Preghenella M., Pegoretti A., Migliaresi C.: Thermomechanical characterization of fumed silica-epoxy nanocomposites. Polymer, **46**, 12065–12072 (2005).
DOI: 10.1016/j.polymer.2005.10.098

[9] Yousefi A., Lafleur P. G., Gauvin R.: Kinetic studies of thermoset cure reactions: A review. Polymer Composites, **18**, 157–168 (1997).
DOI: 10.1002/pc.10270

[10] Huang G. C., Lee J. K.: Isothermal cure characterization of fumed silica/epoxy nanocomposites: The glass transition temperature and conversion. Composites Part A: Applied Science and Manufacturing, **41**, 473–479 (2010).
DOI: 10.1016/j.compositesa.2009.12.003

[11] Bharadwaj R. K.: Modeling the barrier properties of polymer-layered silicate nanocomposites. Macromolecules, **34**, 9189–9192 (2001).
DOI: 10.1021/ma010780b

[12] Yano K., Usuki A., Okada A.: Synthesis and properties of polyimide-clay hybrid films. Journal of Polymer Science Part A: Polymer Chemistry, **35**, 2289–2294 (1997).
DOI: 10.1002/(SICI)1099-0518(199708)35:11<2289::AID-POLA20>3.0.CO;2-9

[13] Kim J-K., Hu C. G., Woo R. S. C., Sham M-L.: Moisture barrier characteristics of organoclay-epoxy nanocomposites. Composites Science and Technology, **14**, 805–813 (2005).
DOI: 10.1016/j.compscitech.2004.10.014

[14] Naya S., Martínez-Vilariño S., Artiaga R.: Efecto de ciclos térmicos en la permeabilidad y propiedades térmicas de compuestos nanoarcilla-epoxi. Dyna, **84**, 71–76 (2009).

[15] Huang K-Y., Weng C-J., Lin S-Y., Yu Y-H., Yeh J-M.: Preparation and anticorrosive properties of hybrid coatings based on epoxy-silica hybrid materials. Journal of Applied Polymer Science, **112**, 1933–1942 (2009).
DOI: 10.1002/app.29302

[16] Drzal L. T., Rich M. J., Koenig M. F., Lloyd P. F.: Adhesion of graphite fibers to epoxy matrices: II. The effect of fiber finish. Journal of Adhesion, **16**, 133–152 (1983).
DOI: 10.1080/00218468308074911

[17] Schadler L. S.: Polymer-based and polymer-filled nanocomposites. in 'Nanocomposite Science and Technology' (eds.: Ajayan P. M., Schadler L. S., Braun P. V.) Wiley, Weinheim, 77–135 (2003).

[18] Prime R. B.: Thermosets. in 'Thermal characterization of polymeric materials (second edition)' (ed.: Turi E.) Academic Press, San Diego, 1380–1766 (1997).

[19] Wetzel B., Haupert F., Zhang M. Q.: Epoxy nanocomposites with high mechanical and tribological performance. Composites Science and Technology, **63**, 2055–2067 (2003).
DOI: 10.1016/S0266-3538(03)00115-5

[20] Park J. H., Jana S. C.: The relationship between nano- and micro-structures and mechanical properties in PMMA-epoxy-nanoclay composites. Polymer, **44**, 2091–2100 (2003).
DOI: 10.1016/S0032-3861(03)00075-2

[21] Han J. T., Cho K.: Nanoparticle-induced enhancement in fracture toughness of highly loaded epoxy composites over a wide temperature range. Journal of Materials Science, **41**, 4239–4245 (2006).
DOI: 10.1007/s10853-006-6219-2

[22] Zhang X., Xu W., Xia X., Zhang Z., Yu R.: Toughening of cycloaliphatic epoxy resin by nanosize silicon dioxide. Materials Letters, **60**, 3319–3323 (2006).
DOI: 10.1016/j.matlet.2006.04.023

[23] Sipaut C. S., Ahmad N., Adnan R., Rahman I. Ab., Bakar M. A., Ismail J., Chee C. K.: Properties and morphology of bulk epoxy composites filled with modified fumed silica-epoxy nanocomposites. Journal of Applied Sciences, **7**, 27–34 (2007).
DOI: 10.3923/jas.2007.27.34

[24] Kang S., Hong S. I., Choe C. R., Park M., Rim S., Kim J.: Preparation and characterization of epoxy composites filled with functionalized nanosilica particles obtained via sol-gel process. Polymer, **42**, 879–887 (2001).
DOI: 10.1016/S0032-3861(00)00392-X

[25] Chang K-C., Lin C-Y., Lin H-F., Chiou S-C., Huang W-C., Yeh J-M., Yang J-C.: Thermally and mechanically enhanced epoxy resin-silica hybrid materials containing primary amine-modified silica nanoparticles. Journal of Applied Polymer Science, **108**, 1629–1635 (2008).
DOI: 10.1002/app.27559

[26] Tarrio-Saavedra J., López-Beceiro J., Naya S., Artiaga R.: Effect of silica content on thermal stability of fumed silica/epoxy composites. Polymer Degradation and Stability, **93**, 2133–2137 (2008).
DOI: 10.1016/j.polymdegradstab.2008.08.006

[27] Llorente M. A., Horta A.: Técnicas de caracterización de polímeros. UNED, Madrid (1991).

[28] Donth E.: The glass transition. Relaxation dynamics in liquids and disordered materials. Springer, Berlin (2001).

[29] Hutchinson J. M., Montserrat S.: The application of modulated differential scanning calorimetry to the glass transition of polymers. I. A single-parameter theoretical model and its predictions. Thermochimica Acta, **286**, 263–296 (1996).
DOI: 10.1016/0040-6031(96)02967-X

[30] Thomas L. C.: An introduction to the techniques of differential scanning calorimetry (DSC) and modulated DSC. in 'Thermal analysis. Fundamentals and applications to material characterization' (ed.: Artiaga R.) Publicationes de la Universidade da Coruna, Coruna, 9–25 (2005).

[31] Reading M., Hourston D. J.: Modulated temperature differential scanning calorimetry: Theoretical and practical applications in polymer characterisation. Springer, Dordrecht (2006).

[32] Schröter K., Wilde G., Willnecker R., Weiss M., Samwer K., Donth E.: Shear modulus and compliance in the range of the dynamic glass transition for metallic glasses. The European Physical Journal B: Condensed Matter and Complex Systems, **5**, 1–5 (1998).
DOI: 10.1007/s100510050411

[33] Artiaga R., García A.: Fundamentals of DMA. in: 'Thermal analysis. Fundamentals and applications to material characterization' (ed.: Artiaga R.) Publicationes de la Publicationes de la Universidade da Coruna, A Coruña, Spain, 183–206 (2005).

[34] Chartoff R. P., Menczel J. D., Dillman S. H.: Dynamic mechanical analysis (DMA). in: 'Thermal analysis of polymers. Fundamentals and applications' (eds.: Menczel J. D., Prime R. B.) Wiley, San Jose, 387–496 (2009).

[35] Menczel J. D., Judovits L., Prime R. B., Bair H. E., Reading M., Swier S.: Differential scanning calorimetry (DSC). in: 'Thermal analysis of polymers. Fundamentals and applications' (eds.: Menczel J. D., Prime R. B.) Wiley, San Jose, 7–239 (2009).

[36] Mohammad A., Simon G. P.: Rubber-clay nanocomposites. in 'Polymer nanocomposites' (eds.: Mai Y-W., Yu Z-Z.) Woodhead Publishing Limited, Abington 297–329 (2006).

[37] Pellín M. P., Regueira L. N., Quintela A. L., Losada P. P., Gándara J. S., Abuín S. P.: Epoxy resins based on trimethylolpropane. II. Kinetic and thermodynamic parameters of cure with *m*-XDA. Journal of Applied Polymer Science, **55**, 1507–1516 (1995).
DOI: 10.1002/app.1995.070551102

[38] Pellin M. P., Regueira L. N., Gandara J. S., Losada P. P., Lamela C. P., Abuin S. P.: Epoxy resins based on trimethylolpropane. I. Determination of chemical structres. Journal of Applied Polymer Science, **55**, 225–232 (1995).
DOI: 10.1002/app.1995.070550205

[39] Quintela A. L., Pellin M. P., Abuin S. P.: Epoxidation reaction of trimethylolpropane with epichlorohydrin: Kinetic study of chlorohydrin formation. Polymer Engineering and Science, **36**, 568–573 (1996).
DOI: 10.1002/pen.10443

[40] Webb P. A.: The perseverance of Sedigraph method in particle sizing. Micromeritics Instrument Corporation, January, 1–6 (2004).

[41] Pena D.: Regresión y diseño de experimentos. Alianza Editorial, Madrid (2002).
[42] Box G. E., Hunter J. S., Hunter W. G.: Estadística para investigadores: Diseno, innovación y descubrimiento. Editorial Reverté, Barcelona (2008).
[43] Maxwell S. E., Delaney H. D.: Designing experiments and analyzing data. A model comparison perspective. Lawrence Erlbaum Associates, New Jersey (2004).
[44] Shapiro S., Wilk M. B.: An analysis of variance test for normality (complete samples). Biometrika, **52**, 591–611 (1965).
DOI: 10.1093/biomet/52.3-4.591
[45] Bartlett M. S.: Properties of sufficiency and statistical tests. in 'Proceedings of the Royal Society of London. Series A: Mathematical and Physical Sciences' Vol 160, 268–282 (1937).
[46] Durbin J., Watson G. S.: Testing for serial correlation in least squares regression. I. Biometrika, **37**, 409–428 (1950).
DOI: 10.1093/biomet/37.3-4.409
[47] Durbin J., Watson G. S.: Testing for serial correlation in least squares regression. II. Biometrika, **38**, 159–178 (1951).
DOI: 10.1093/biomet/38.1-2.159
[48] Reed K. E.: Dynamic mechanical analysis of fiber reinforced composites. Polymer Composites, **1**, 44–49 (1980).
DOI: 10.1002/pc.750010109